

**Investigation on Macroscopic Mechanical Behavior of
Magnetorheological Elastomers under Shear deformation,
using Microscale Representative Volume Element Approach.**

Ilda Abdollahi

A Thesis

In

The Department

Of

Mechanical, Industrial and Aerospace Engineering

Presented in Partial Fulfillment of the Requirements for The Degree of
Master of Mechanical Engineering

Concordia University

Montreal, Quebec, Canada

December 2023

© Ilda Abdollahi, 2023

CONCORDIA UNIVERSITY

School of Graduate Studies

This is to certify that the thesis prepared

by: **Ilda Abdollahi**

Entitled: **Investigation on Macroscopic Mechanical Behavior of Magnetorheological Elastomers under Shear deformation, using Microscale Representative Volume Element Approach.**

and submitted in partial fulfillment of the requirements for the degree of

Master of Applied Science in Mechanical Engineering

complies with the regulations of the University and meets the accepted standards with respect to originality and quality.

Signed by the final examining committee:

_____ Chair

Dr. Hang Xu

_____ Examiner

Dr. Amir G Aghdam

_____ Examiner

Dr. Hang Xu

_____ Thesis Supervisor

Dr. Ramin Sedaghati

Approved by _____

Dr. Sivakumar Narayanswamy, Graduate Program Director

Dr. Mourad Debbabi, Dean

Gina Cody School of Engineering and Computer Science.

Date: Dec 20, 2023

ABSTRACT

Investigation on Macroscopic Mechanical Behavior of Magnetorheological Elastomers under Shear deformation, using Microscale Representative Volume Element Approach.

Ilda Abdollahi

Magnetorheological (MR) materials are intriguing smart materials that transform their physical characteristics in response to external magnetic fields. While MR fluids (MRFs) are often in the spotlight due to their rapid response and field-dependent yield strength and apparent viscosity, they grapple with issues like magnetic particle deposition and settling as well as leakage in MRF based devices. On the other hand, magnetorheological elastomers (MREs) are versatile, magnetically responsive composite materials with rubber-like qualities. By blending magnetic particles into nonmagnetic elastomeric matrices, MREs demonstrate field-dependent viscoelastic properties, such as a customizable field-dependent modulus which cannot be achieved using MRFs. MREs can instantly revert to their original state when the magnetic field is withdrawn, showcasing a fascinating interplay of magnetism and material science. MREs fall into two distinct categories depending on their curing process; those formed without the influence of a magnetic field, creating isotropic MREs, and those shaped under the application of a magnetic field, yielding anisotropic MREs.

During the recent decades, the advent of finite element (FE) modeling has provided considerable benefits, by reducing the financial and time expenses forced by experimental procedures. Alongside with providing substantial accuracy, its ability to conduct parametric studies with multiple systematic parameter adjustments, ensuring greater reproducibility while simultaneously reducing the environmental impact by minimizing resource consumption and waste production are among its significant benefits. As a finite element approach, the concept of Representative Volume Element (RVE) enables predicting the material's macroscopic behaviour from microscale modeling.

This research thesis aims at modeling the MREs' shear behaviour under the influence of magnetic field, using the RVE concept as the modeling scheme. For this purpose, MREs with different elastomeric host matrix including silicone rubber Ecoflex 30 and Ecoflex 50 have been considered. The stress-strain characteristic of these pure silicon rubbers was first evaluated experimentally using available tensile test machine. The experimental data was then used to identify the constant parameters of the Ogden strain energy function using the least-square minimization technique. The optimized Ogden strain energy function is subsequently used in the finite element model to characterize the matrix behavior of the MREs. These, along with the mechanical and magnetic properties of Carbonyl Iron Particle

(CIP), used as magnetic particles in MREs, were integrated into COMSOL Multiphysics to develop the RVE for the MREs, integrating properties of the matrix with magnetic particles. The RVE was generated in 2D and 3D configurations, for CIP volume fraction varying from 5% to 40%. Periodic Boundary Condition (PBC) was imposed on the RVE boundaries, while undergoing pure shear deformation. The results of 2D modeling suggest its ability to predict the shear deformation behaviour of isotropic MRE-RVE under varied external magnetic field. The maximum difference between theoretical and experimental shear modulus under varied magnetic field was found to be $\pm 20\%$, however, the 2D model was not able to predict the MR effect at saturation with acceptable accuracy. The results from 3D modeling of isotropic MRE-RVE show a reasonably good agreement with the experiment data, with the error generally in the range of 1%- 4% for magnetic flux densities up to 0.4T. The results also suggest that the MRE-RVE with the softer silicone rubber matrix (Ecoflex 30) provides substantially higher MR effect compared with the MRE-RVE based on Ecoflex 50. Moreover, 3D isotropic MRE-RVE predicts the influence of CIP volume fraction on the shear behaviour and MR effect of MREs, comparable to experiments. All in all, the developed 3D isotropic MRE-RVE has shown the potential to accurately predict the field-dependent macroscopic mechanical properties of different MREs and thus can be used effectively to design MREs with enhanced properties without expensive experimental tests.

To Myself,

for never giving up

and

to my loving husband,

Hossein,

for always being there for me.

Acknowledgements

I would like to express my genuine appreciation to all the professional guidance and support provided by my supervisor, Professor Ramin Sedaghati, during my studies. I deeply appreciate the opportunity of joining his research group and the invaluable knowledge and skills I gained through this time under his supervision. I would also like to express my appreciation to Seyed Alireza Moezi for his kind assistance and guidance in conducting the experiments.

My deepest gratitude goes to my mother, Mehrangiz, the miracle of my life. For all she gave me, all she taught me, and the way she believed in me. For teaching me how to be resilient and caring at the same time, and for her endless love and patience. My heartfelt appreciation goes to my beloved husband, Hossein, for his unconditional love and support during my studies which was just a tiny fraction of his warm and unwavering presence during these 10 years of wonderful companionship. As Julie Smith says in her book “If mine is the ink, then yours is the paper”, none of my success was possible, if he did not believe in me.

Last but not least, I am wholeheartedly thankful of my loved ones, Maryam and Parham, for being genuine supporters of my success, and being the ones who my joy brings them joy and my sorrow melts in their warm love.

Table of Contents

List of Figures	X
List of Tables	XVi
Nomenclature	XVii
Chapter 1: Introduction, Literature Review and Objectives	1
1.1 Introduction	1
1.2 The Composition of Magnetorheological Elastomers.....	2
1.2.1 Magnetic particles.....	2
1.2.2 Elastic matrices	3
1.2.3 Additives.....	5
1.3 Fabricating methods	5
1.4 Magnetorheological Effect in MREs.....	6
1.5 Microstructures and macroscopic properties of MREs	8
1.5.1 Microstructures of MREs.....	8
1.5.2 Macroscopic properties of MREs	9
1.6 Applications of MREs.....	10
1.6.1 Vibration absorbers.....	10
1.6.2 Vibration isolators.....	11
1.7 State-of-the-art on characterization of MREs	12
1.8 Current Study and Contributions	14
1.9 Thesis Organization.....	15
Chapter 2: Methodology and Mathematical Concepts	16
2.1 Representative Volume Element (RVE):.....	16
2.2 The RVE Size for Models Containing Hard Particles.....	18
2.3 Determining the RVE Size for MREs with Spherical Particles.....	21
2.4 RVE Boundary Conditions	23
2.4.1 Displacement Boundary Conditions (DBC)s.....	24
2.4.2 Traction Boundary Conditions (TBCs).....	24
2.4.3 Periodic Boundary Conditions (PBCs).....	25
2.4.3.1 Periodic Boundary Conditions in 2D	25

2.4.3.2	Computational Homogenization in 2D	26
2.4.3.3	Periodic Boundary Conditions in 3D	27
2.4.3.4	Computational Homogenization in 3D	30
2.5	Maxwell Equations.....	33
2.6	Maxwell’s Stress Tensor	35
2.7	Governing Equations.....	36
2.8	Summary and Conclusion	37
Chapter 3:	Characterization of Elastomeric Matrix and Magnetic Inclusion in MREs.....	38
3.1	Silicone Rubber Tensile Test	38
3.1.1	Sample Fabrication	38
3.1.2	Characterization of the MRE’s Elastomeric Matrix, using Uniaxial Tensile Test .	40
3.2	Hyper-Elastic Strain Energy Function	42
3.2.1	Ogden Hyper-Elastic Material Model.....	43
3.3	Identification of Ogden Model Parameters	44
3.4	Magnetic Properties of Carbonyl Iron Particles.....	46
3.5	Summary and Conclusion	49
Chapter 4:	Finite Element Modeling of MRE, using Representative Volume Element (RVE)	50
4.1	Modeling the 2D MRE-RVE in Comsol.....	50
4.1.1	Isotropic MRE-RVE	50
4.1.2	Meshing Pattern	50
4.1.3	Shear Deformation of Isotropic MRE-RVE	53
4.2	Modeling the 3D MRE-RVE in Comsol.....	61
4.2.1	Isotropic MRE-RVE	61
4.2.2	Meshing Pattern	63
4.2.3	Shear Deformation of Isotropic MRE-RVE	65
4.2.3.1	Silicone Rubber Ecoflex 50 MRE-RVE	65
4.2.3.2	Silicone Rubber Ecoflex 30 MRE-RVE	71
4.3	Summary and Conclusion	75
Chapter 5:	Contributions, Conclusion and Future Remarks.....	77
5.1	Major Contributions.....	77
5.2	Major Conclusions	77
5.3	Future Remarks	78

References	80
Appendix 1	86

List of Figures

Figure 1: SEM microscopic images of Carbonyl Iron Particles with different magnification [18, 19].	3
Figure 2: magnetic properties of CIP (Magnetization vs magnetic field intensity) [20].	3
Figure 3: Silicone rubber liquid state and molded Silicon [94].	4
Figure 4: MRE content and the classification of additives used in MREs [23].	5
Figure 5: Schematic representation of MRE fabrication [6].	6
Figure 6: Relative MR effect vs magnetic field for different Silicone oil (SO) content for (a) isotropic and (b) anisotropic MRE [28].	7
Figure 7: Shear behavior of MREs with 30% volume fraction of Iron particles with varying diameters 5 -150 μm . (a) initial shear Modulus vs particle diameter, and (b) saturated magnetic-induced shear modulus ΔG vs particle diameter [37].	8
Figure 8: SEM images of MREs prepared under different magnetic flux densities B (a) No field, (b) 200 mT, (c) 400 mT, (d) 600 mT, (e) 800 mT, and (f) 1000 mT with two different magnification of 200 times and 1600 times [41].	9
Figure 9 : Shear storage modulus of different natural rubber MRE samples consisting of 60, 70, 80, and 90% weight fraction of CIP (left) [22], and stress-strain loops of a silicone rubber MRE sample under different magnetic fields (right) [42].	10
Figure 10: Schematic of the MRE-based semi-active adaptive tuned vibration absorber (SATVA) [46].	11
Figure 11: MRE-based isolator: cross-sectional view of designed layout (left) and the fabricated prototype (right) [47].	12

Figure 12: The RVE size regarding different reinforcement particle shapes: (a) spherical particles, (b) oblate spheroids, (c) prolate spheroids and (d) gigantic fibers [65]..... 18

Figure 13: Morphological equivalence between RVEs of overlapping and non-overlapping spheres [70]..... 18

Figure 14: The MRE-RVE, containing finite element mesh used in calculation of shear modulus [40]..... 21

Figure 15: The gap region between two consequent particles, with radius R and the gap being $2w$. [40]..... 22

Figure 16: The schematic representation of a unit cell with one particle included. 22

Figure 17: The effect of the gap between two subsequent particles on shear modulus of MRE as the ratio of the gap to particle's radius (w/R) [40]..... 23

Figure 18: The change in modulus ($\Delta G = G-G_0$) at saturation, normalized to the initial modulus in the absence of the magnetic field (G_0), with respect to volume percentage of particles [40].. 23

Figure 19: Selected unit cells to analyze a heterogeneous material behaviour under tensile loading 1) Symmetric unit cell (solid line) and 2) asymmetric (dashed line) [81]..... 25

Figure 20: Periodically deformed 2D unit cell, with boundaries Γ_{ij} and vertices v_i [81]. 27

Figure 21: A typical 3D RVE, containing fibers, with the bounding domain of Ω_{RVE} [82]. 28

Figure 22: Tensile loading applied to 3D RVE in a) X , b) Y and c) Z direction, respectively [82]. 30

Figure 23: Shear loading applied to 3D RVE in a) XY , b) YZ and c) XZ plane, respectively [82]. 30

Figure 24: A schematic representation of macro- and micro-field relationship in 3D-RVE [82]. 32

Figure 25: Fabricating the molds using a 3D-printer (Original Prusa i3 MK3S+) (left), and the fabricated molds (right).....	39
Figure 26: (a) Parts A and B for fabricating silicone rubber Ecoflex 30, (b) the pressed mold containing the mixture to be cured , and (c) the cured final samples (30 indicates EcoFlex 30 and 50 refers to EcoFlex 50).....	40
Figure 27: (a) silicone rubber sample (Ecoflex 30) assembled on MTS machine prior to the tensile test, (b) sample through final steps of tensile test, and (c) the failed sample.	41
Figure 28: (a) silicone rubber sample (Ecoflex 50) assembled on MTS machine prior to the tensile test, (b) sample through final steps of tensile test, and (c) the failed sample.	41
Figure 29: The extracted raw data of the conducted pure tensile to failure test, for silicone rubber-Ecoflex30 and Ecoflex50.....	42
Figure 30: Curve-fitted plots for silicone rubber Ecoflex30 using least-square method, using GA and hybrid GA+SQP methods.	46
Figure 31: Curve-fitted plots for silicone rubber Ecoflex50 using least-square method, using GA and hybrid GA+SQP methods.	46
Figure 32: B-H curve for CIP provided by the manufacturer (Mekatronik Ilmenau, Germany). 47	
Figure 33: Extrapolated B-H curve of CIP. Vertical data represents Magnetic flux density (B) in Tesla and the Horizontal is the field intensity in A/m.	48
Figure 34: The 2D RVE generated in Comsol, Carbonyl Iron inclusion (Circle) inside the silicone rubber matrix (the gray square) surrounded by air domain (the purple square).....	51
Figure 35: Mesh sensitivity analysis graph for 2D MRE-RVE model, Ecoflex 50 ($\phi=15\%$, $B=0.2T$)......	52

Figure 36: (a) The mesh pattern of MRE-RVE surrounded by the air domain (purple square), (b) The boundary layers implemented to enhance precision around the inclusion 52

Figure 37: The magnetic field distortion around the CIP inclusion (the circle), while the small square indicates the RVE boundaries and the big square is the air domain boundary. The color definition bar depicts the magnetic flux density in Tesla. 53

Figure 38: The shear deformation of MRE-RVE under 30% shear strain, while the periodic boundary conditions are being applied on the RVE boundaries. The color definition bar depicts the displacement magnitude in μm 54

Figure 39: The magnetic boundary loads applied on the CIP inclusion boundaries. The color definition bar depicts the Maxwell upward stress tensor in Pa. 54

Figure 40: The whole shear stress (combination of magnetic and mechanical stress) in the RVE. The color definition bar depicts the stress magnitude in Pa. 55

Figure 41: Shear stress- shear strain plot for 2D MRE-RVE under different applied magnetic fields..... 56

Figure 42: Comparison of shear modulus versus magnetic flux density obtained from Comsol FE modeling of 2D isotropic MRE-RVE with the experimental results [55] for silicone rubber Ecoflex 50-MRE with 15% VF of CIP. 57

Figure 43: Shear stress- shear strain plot for 2D MRE-RVE under different applied magnetic fields for silicone rubber Ecoflex 50 with (a) 5%, (b) 10%, (c) 20%, (d) 27%, (e) 35%, and (f) 40% of CIP in volume fraction..... 58

Figure 44: MR effect behaviour in 2D modeling of silicone rubber (SR) Ecoflex50 MRE-RVE with respect to CIP volume fraction. 59

Figure 45: Comparison of shear modulus variation with respect to the applied magnetic flux density, for 2D MRE-RVEs with silicone rubber Ecoflex 30 and Ecoflex 50 as the matrix material. 60

Figure 46: Comparison of the MR effect behaviour in 2D isotropic MRE-RVEs with different matrix materials (Ecoflex 50 and Ecoflex 30), with respect to CIP volume fraction. 60

Figure 47: Different RVE arrangements (a) Simple Cubic (SC)-Davis (b) Simple Cubic (SC) (c) Body-Centered Cubic (BCC) (d) Face-Centered Cubic (FCC) (e) End-Centered Cubic (ECC) (f) Body- and End-Centered Cubic (BECC)..... 62

Figure 48: The 3D RVE generated in Comsol, Carbonyl Iron inclusion (the sphere) inside the silicone rubber matrix (the purple cube), surrounded by air domain (the gray cube). 63

Figure 49: Mesh sensitivity analysis graph for 3D MRE-RVE model, ($\phi=15\%$, $B= 0.1T$) using different meshing schemes..... 64

Figure 50: (a) The mesh pattern of MRE-RVE surrounded by the air domain, (b) The mesh quality in all regions with the color bar representing the quality of mesh in scale of 0 to 1. 65

Figure 51: The magnetic field distortion around the CIP inclusion inside the 3D RVE, red arrows represent the magnetic field intensity and direction (0.1 T, upward), the color definition bar describes the magnetic flux density (T) in the air and MRE-RVE domain referring to the hypothetical cut out surface in the middle of the model. 66

Figure 52: The magnetic boundary loads applied on the CIP inclusion boundaries under magnetic flux density of 0.1T. The color definition bar expresses the Maxwell upward stress tensor in Pa. 67

Figure 53: The shear deformation of MRE-RVE under 30% Shear strain, while the periodic boundary conditions are being applied on the RVE boundaries. The color definition bar depicts the Tresca stress in Pa. 67

Figure 54: Shear stress- shear strain plot for 3D MRE-RVE (Ecoflex 50), containing 15% of CIP in volume fraction under different applied magnetic fields..... 68

Figure 55: Shear modulus versus magnetic flux density for 3D isotropic MRE-RVE..... 69

Figure 56: Shear stress- shear strain plot for 3D Isotropic MRE-RVE under different applied magnetic fields for silicone rubber (SR) Ecoflex 50 with (a) 5%, (b) 10%, (c) 20%, (d)27%, (e)35%, and (f) 40% of CIP in volume fraction..... 70

Figure 57: Relative MR effect for silicone rubber Ecoflex50 MRE-RVE versus CIP volume fraction. 71

Figure 58: MRE-RVE (Ecoflex30) shear stress- strain behaviour under the application of different magnetic fields. 72

Figure 59: Shear stress- shear strain plot for 3D Isotropic MRE-RVE under different applied magnetic fields for silicone rubber Ecoflex 30 with (a) 5%, (b) 10%, (c) 20%, (d)27%, (e)35%, and (f) 40% of CIP in volume fraction. 73

Figure 60: Relative MR effect versus CIP volume fraction obtained from isotropic 3D MRE-RVE for silicone rubber Ecoflex30..... 74

Figure 61: Comparing MR effect versus CIP volume fraction obtained from 3D Isotropic MRE-RVE for silicone rubber Ecoflex 30 and silicone rubber Ecoflex 50. 75

List of Tables

Table 1: The optimized parameters gained through curve fitting the experimental data with the Ogden strain energy function.....	45
Table 2: Material properties of Silicone Rubber.....	45
Table 3: Material properties of air and CIP	48
Table 4: Comparing the results of 2D MRE-RVE and the Experiments.	56
Table 5: Comparison of the initial shear moduli of different MRE-RVE arrangements with experimental data (No field applied) Silicone rubber Ecoflex50- $\Phi = 15\%$	62

Nomenclature

V	Volume
ϕ	Volume fraction
A	Integral range
G	Shear Modulus
G_0	Zero-field Shear Modulus
D_z^2	Variance
S_z^2	Point Variance
ε_{abs}	Absolute Error
ε_r	Relative Error
n	Number of Realization
c	contrast
R	Inclusion's radius
$2w$	The gap between inclusions
ν	Poisson's ratio
H	Magnetic field intensity
B	Magnetic flux density
ε	strain
σ	stress
x_j	Location of points inside RVE
Γ	RVE surface boundary
Γ_p	Boundary pairs
u_i	displacement
t_i	traction
τ	Shear stress
γ	Shear strain
n_j	Normal unit vector
e_j	Coordinate system unit vector
u_{ij}	Displacement vector
v_i	RVE vertices
u_{v_i}	Displacement vector of vertices
R	Unit cell region
ψ	Arbitrary material quantity
$\sigma_{ij} (macro)$	Macroscopic total stress tensor
$\varepsilon_{ij} (macro)$	Macroscopic total strain tensor
$\langle \sigma_{ij} \rangle$	Average microscopic stress
$\langle \varepsilon_{ij} \rangle$	Average microscopic strain
E_{ii}^{eff}	effective Young's modulus
ν_{ij}^{eff}	effective Poisson ratio
G_{ij}^{eff}	effective shear modulus

Ω_{RVE}	the bounding domain of the 3D RVE
X_{pos}	RVE surface positioned at the positive end of X axis
$X_{posNodes}$	Nodes on X_{pos} surface
X_{neg}	RVE surface positioned at the negative end of X axis
S_{np}	RVE surfaces
N_1	RVE corner nodes
δ	prescribed positive displacement
L_{macro}	Macroscale length
V_{RVE}	RVE size
∇	Gradient operator
E	Electric field intensity
D	Electric displacement
ϵ_0	Electric permittivity of air
μ_0	Magnetic permeability of air
C_0	Light speed in vacuum
μ_r	Relative magnetic permeability
φ	Free charge density
J	Free current density
ϵ	Dielectric constant
Q	Electric conductivity
P	Polarization density
M	Magnetization density
q	Electric charge
v	velocity
t	time
F	Force
f	Force per unit volume
δ_{ij}	Kronecker delta
T_{ij}	Maxwell Stress tensor
ρ	density
\mathbf{T}	Total Stress tensor
f_m	Magnetic force per unit volume
W	strain energy function
λ_i	principal stretches
I_1, I_2, I_3	strain invariants
μ_p	Ogden parameter
α_p	Ogden parameter

Chapter 1: Introduction, Literature Review and Objectives

1.1 Introduction

Magnetorheological (MR) materials are a class of smart materials with the incredible ability to change their physical or mechanical characteristics rapidly in less than few milliseconds in response to an external magnetic field. These materials are fabricated by dispersing magnetic particles inside nonmagnetic host matrices. Depending on the matrix, MR materials can be classified as magnetorheological fluids (MRF), magnetorheological elastomers (MRE), magnetorheological grease (MRG), magnetorheological polymer gels (MRPGs), and other novel MR intelligent materials to be explored and developed. Most MR applications and discussions generally focus on the MR fluid, for the reaction time of MR fluid is often shorter than that of other types. The interaction among the induced dipoles in these fluidal materials leads to the formation of columnar structures aligned with the applied magnetic field. These chain-like formations impose restriction on fluid flow, elevating the viscosity of the suspension. The energy required to yield these interconnected structures rises with the intensity of the applied magnetic field, leading to a yield stress that is contingent on the magnetic field. MR fluid is often utilised as a working fluid in several types of vibration absorbers/isolators, clutches, dampers, and valves. However, despite its benefits, MR fluid has drawbacks that are still up for debate, such as magnetic particle sedimentation, which often occurs while the device is not operating, sealing problems, and environmental contamination [1–5].

While MR fluids are susceptible to settling, MR elastomers are not, because the employed magnetic particles are often bonded by a carrier matrix like rubber. Magneto-rheological elastomers (MREs) stand as multi-functional materials, exhibiting the capability of dynamically altering their mechanical properties, including stiffness, and damping capacity, in response to an external magnetic field. By the removal of the magnetic field, MREs will recover their original, inherent properties. Owing to the magnetic particles' sensitivity to an external magnetic field, MREs exhibit a magnetorheological (MR) effect in the presence of the field, defined as the ratio of the change in the field-dependent physical or mechanical property, to the value of the same property when no field is applied. Several factors may affect the obtained MR effect, such as the magnetic particles' content, shape, size and distribution and the matrix mechanical properties [6–8].

MREs are comprised of three fundamental components: magnetic particles, nonmagnetic elastic matrices, and additives. To obtain a stronger magnetic field-sensitive effect from magnetic particles, higher permeability and higher saturation magnetization are substantially desirable [9, 10]. Numerous polymeric rubbers, either high modulus or low modulus may be considered as the elastic matrix. Additives are generally considered based on the particle and matrix composition, typically Silicone oil is widely used additive. Speaking of the fabrication methods, there are several methods for fabricating MREs. Due to the application of a magnetic field during the curing process, it is possible to produce MREs with an anisotropic particle-formed microstructure, and

when no field is applied during the curing process, prepared MREs have isotropic particle-formed microstructure [11, 12]. It is important to note that the properties of isotropic MREs and anisotropic MREs can vary significantly. Research has shown that anisotropic MREs exhibit higher field-dependent increases in their properties. From these evaluations, MREs show great potential to be incorporated into design of intelligent devices in a variety of engineering disciplines, including but not limited to vibration absorbers, vibration isolators, sensors, controllable valves, automotive bushing, adaptive beam structures [13–15].

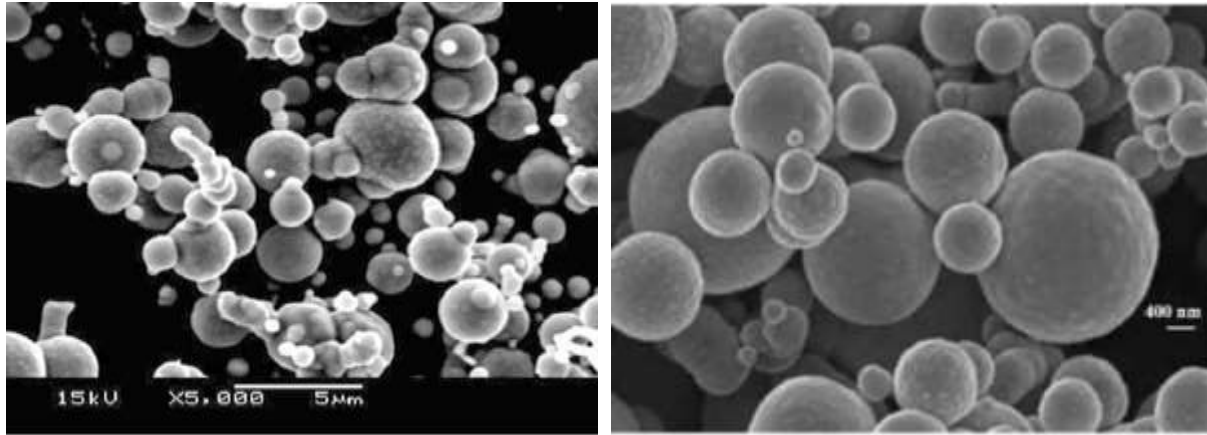
1.2 The Composition of Magnetorheological Elastomers

1.2.1 Magnetic particles

As previously pointed out, for magnetic particles, higher permeability and higher saturation magnetization are preferred in order to achieve a stronger magnetic field-sensitive effect. Micron-sized CI powder is currently extensively used as a magnetic particle for fabricating MREs, among an array of magnetic particle materials [16, 17]. Fig. 1 depicts CI particles (CIPs) in different magnifications. In general, the magnetic particles can range in size from nanometers to micrometers [18,19].

As illustrated in Fig. 2, CIP possesses a very high permeability, saturation magnetization, and a negligible remnant magnetization. Saturation magnetization can exceed 600 kA/m, and there is minimal remnant magnetization when the magnetic field is withdrawn. This mainly stems from the fact that the weight fraction content of Fe in CI powder is more than 97.5%. Due to its exceptional magnetic property, CI powder is extensively employed in production of magnetic materials, including MREs [20].

Compared with their analogous fluids (MR fluids), relatively larger diameters of polarizable particulates can be used in MREs as sedimentation is no longer an issue. Considering this capability of MREs, they generally exhibit a greater MR effect, due to possibility of using sufficiently large particles to sustain at least a few magnetic domains. Carbonyl Iron particles (CIPs) of various diameters, ranging from 1 μm to 200 μm , have been used extensively in the reported research [16].



(a)

(b)

Figure 1: SEM microscopic images of Carbonyl Iron Particles with different magnification [18, 19].

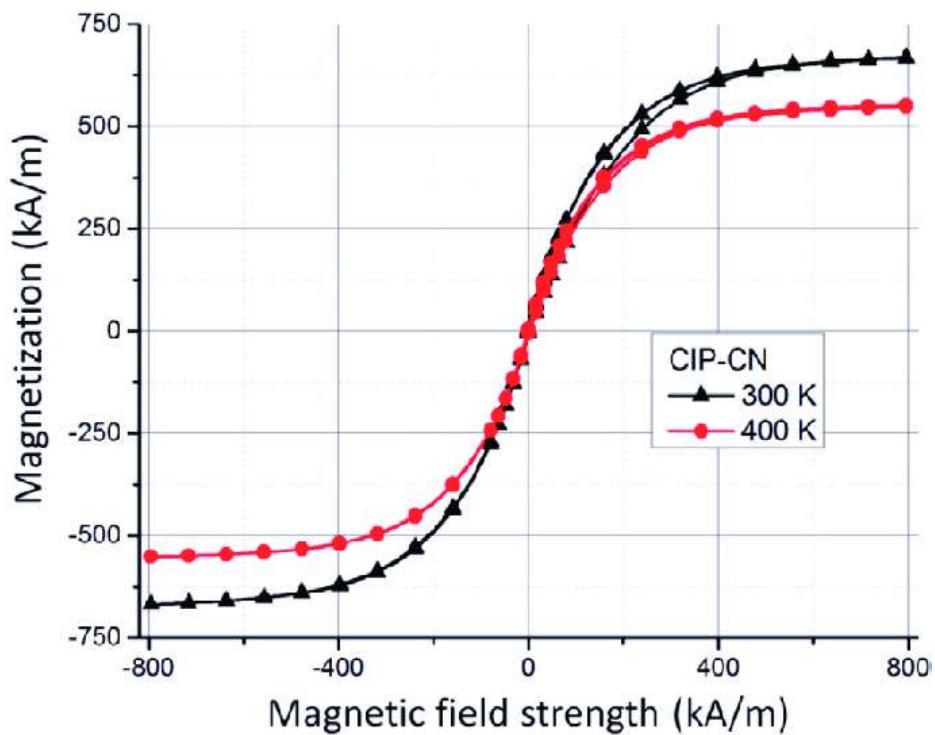


Figure 2: magnetic properties of CIP (Magnetization vs magnetic field intensity) [20].

1.2.2 Elastic matrices

An essential requirement of elastic matrices to fabricate MREs is possessing a soft elastic property, that can hold magnetic particles in a stable manner in the absence of a magnetic field, while allowing to undergo a finite deformation in the presence of a magnetic field. For the elastic matrices, there are an array of polymeric rubbers as potential candidates, for instance, natural and

synthetic rubber, silicone rubber, polyurethane, thermoplastic and polyvinyl alcohol, butadiene rubber, butyl rubber, polyurethane, epoxy and etc.

The modulus of these matrices varies significantly depending on their characteristics and preparation conditions. Normally, the modulus of silicone rubber is less than 1.0 MPa [21], or the tensile strength of natural rubber is typically in order of MPa [22]. With respect to magnetic properties, the magnetic permeability of the matrix material is the most important aspect beyond rheological parameters in determining the mechanical properties of MREs. Since matrix material magnetization could adversely affect polarisation of the particles and thus the MR effect, it is essential that the matrix's magnetic permeability be kept as low as possible [16].

Silicone rubber compounds are distinguished from other rubbers because of their combination of inorganic and organic properties, making them the most extensively used materials in MREs (Fig. 3). The Si-O bonding is largely responsible for the improved thermal stability, electrical insulation, and chemical stability. Silicone rubbers are the most often used matrices in MREs, since they are inexpensive and can be easily fabricated. They possess a mechanically low modulus, exceptional chemical stability and are non-toxic and non-polluting [21].



Figure 3: Silicone rubber liquid state and molded Silicon [94].

In general, the modulus of silicone rubber is significantly lower than that of other rubbers over a broad temperature range. In addition, the thermal conductivity of silicone rubber varies widely. Furthermore, when the anisotropic MREs are needed, the low viscosity inherent to silicone rubber enables the flexible mobility of the magnetizable particles under the magnetic field. On the basis of the aforementioned properties, silicone rubber can be selected as the optimal flexible elastic matrix for fabricating MREs, and it is used widely in the production of MREs [22].

1.2.3 Additives

Along with magnetic particles and elastic matrices to prepare MREs, additives are also essential (Fig.4). The damping properties of MREs are substantially influenced by the interaction between the particles and the elastomeric matrix at their interface, and that is where additives come along with importance. Typically, silicone oil is used as an additive in the production of MREs. When the molecules of the silicone oil enter the matrix, the intermolecular spaces are widened, resulting in the reduction of conglutination of the matrix molecules. Enhancing the plasticity and fluidity of the matrix, the additives can also average the distribution of internal stress in the materials, providing a stable material property for MR elastomer materials. Carbon black, carbon nanotubes, silver nanowire, etc. are also used as additives and fillers to enhance the mechanical properties and MR effect in MREs. Most MREs have silicone oil added to them, which acts as a softening agent and reduces the storage modulus of the elastomeric matrix. Increased compatibility between the matrix and the ferromagnetic particles along with agglomeration deterrence are other benefits of using additives [23–27].

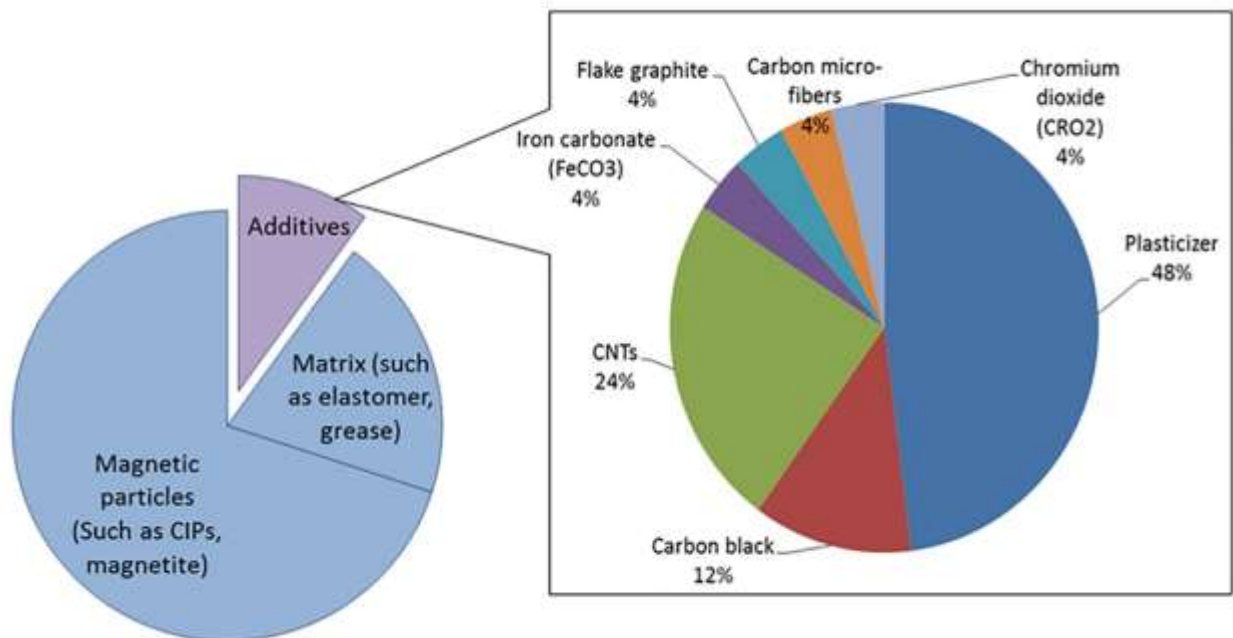


Figure 4: MRE content and the classification of additives used in MREs [23].

1.3 Fabricating methods

Fig. 5 is a streamlined representation of the conventional MRE fabricating procedure. Typically, magnetic particles and matrix material (ex. silicon rubber) are thoroughly mixed with additives to form an easily deformed mixture with a very low yield stress. This mixture is then vulcanized either at room temperature or high temperature above 120°C, namely Room-Temperature

Vulcanizing (RTV) and High-Temperature Vulcanizing (HTV), respectively. With respect to applying a magnetic field during curing, two types of MREs can be produced, isotropic and anisotropic. Curing in the absence of a magnetic field leads to uniformly dispersed magnetic particles in the matrix indicated as isotropic MREs. If a magnetic field is applied to the mixture during the vulcanizing, the magnetic particles would move in the matrix and gradually form chain-like structures parallel to the applied field's direction, resulting in anisotropic MREs. Some studies have also considered hybrid and novel fabricating methods for MREs through 3D-printing [28–30].

Since the advent of MREs, similar methods have been conducted for fabrication of MREs with different matrices, ferromagnetic particles and additive materials. Several studies have examined the factors affecting the properties of MREs, specifically the size and volume fraction of ferromagnetic particles, and the elastic property of matrix material [22, 31–33]. Considering these studies one can observe that CIPs are the most common particles used in fabrication of MREs within the range of 1-10 μ m in diameter. Silicon rubber is also the most preferable matrix and is usually mixed with Silicon oil as an additive.

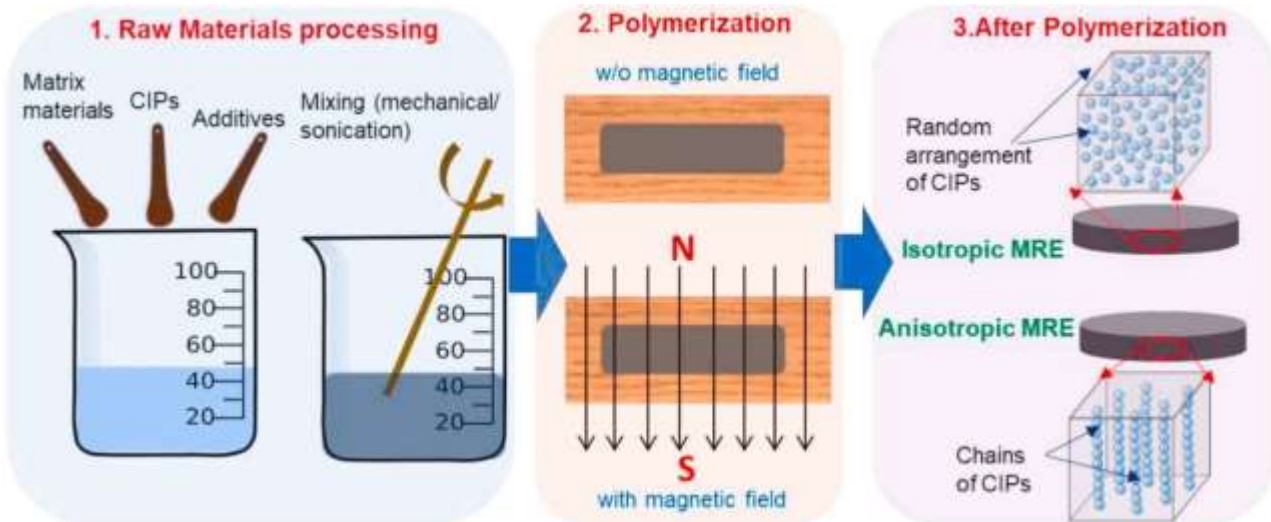


Figure 5: Schematic representation of MRE fabrication [6].

1.4 Magnetorheological Effect in MREs

A magnetic field can alter the material properties of MREs due to the magnetic field-sensitivity of the magnetic particles. Magnetorheological effect (MR effect) is defined for MREs in two ways; absolute MR effect and Relative MR effect. The absolute MR effect is the difference between the maximum value of a property achieved under a magnetic field, and that obtained without the influence of a magnetic field, while the relative MR effect is expressed as the ratio of the increase of a property at a measured magnetic field to its initial value at zero magnetic field. For instance, speaking of shear modulus, the absolute MR effect is characterized by ($\Delta G = G_{max} - G_0$) and the relative MR effect is the ratio of modulus increment ΔG at a measured magnetic field to the initial modulus G_0 , (i.e. $\Delta G / G_0$) [34].

The absolute MR effect does not change with changes in the matrix material, but the relative MR effect does change with changes in the stiffness. The relative MR effect was shown to be greater in matrices with lower stiffness and zero field modulus [16]. Thus it is preferred to lower the matrix's stiffness by using additive plasticizers or softer matrix materials [35]. Fig. 6 shows the relative MR effects of isotropic and anisotropic MREs depending on the amount of silicone oil added to the MRE [28]. As it is observed, increasing the content of silicone oil (SO) gives a higher relative MR effect, by decreasing the matrix stiffness at zero field [24].

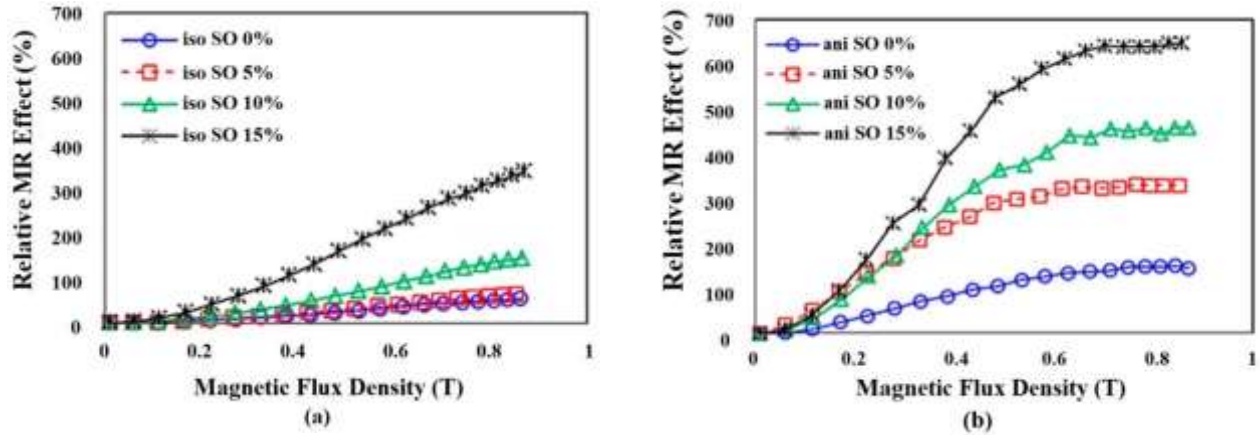


Figure 6: Relative MR effect vs magnetic field for different Silicone oil (SO) content for (a) isotropic and (b) anisotropic MRE [28].

Since sedimentation of the particles is not an issue in MREs, larger polarizable particle sizes can be used in MREs compared with MR fluids. Various sizes of CIP, ranging from $1\mu\text{m}$ to $200\mu\text{m}$ in diameter, have been used in the reported studies [16, 32, 36–38]. For instance, Qian Jin et al. [37] studied the mechanical properties of different MRE samples with iron particles of 5 different diameters ranging from $5\mu\text{m}$ to $150\mu\text{m}$, while keeping volume fraction at 30%. Their study showed that increasing the particle size, lowers the initial shear modulus G_0 , while causing the saturated magnetic-induced shear modulus G to increase to a maximum value and then decline (Fig. 7).

It is noted that due to the presence of air between the iron particles, the apparent density of iron powder is significantly lower than that of solid iron particles. In MREs, the rubbery matrix fills the interstitial space between the particles. The iron particles are in close proximity to one another when the rubber is loaded with a critical or optimum particle volume concentration (CPVC), defined as the ratio of the apparent density to real density of the particles. Getting closer to this critical content, the distances between the particles decreases and further increase in particle volume fraction means that the elastomer cannot fill the gaps between the particles properly. Hence, it is observed that around CPVC the MREs exhibit the maximum relative MR effect and further increase in particle content drops the relative MR effect [39]. The CPVC reported in the literature is in the range 27%- 29% [31, 39, 40].

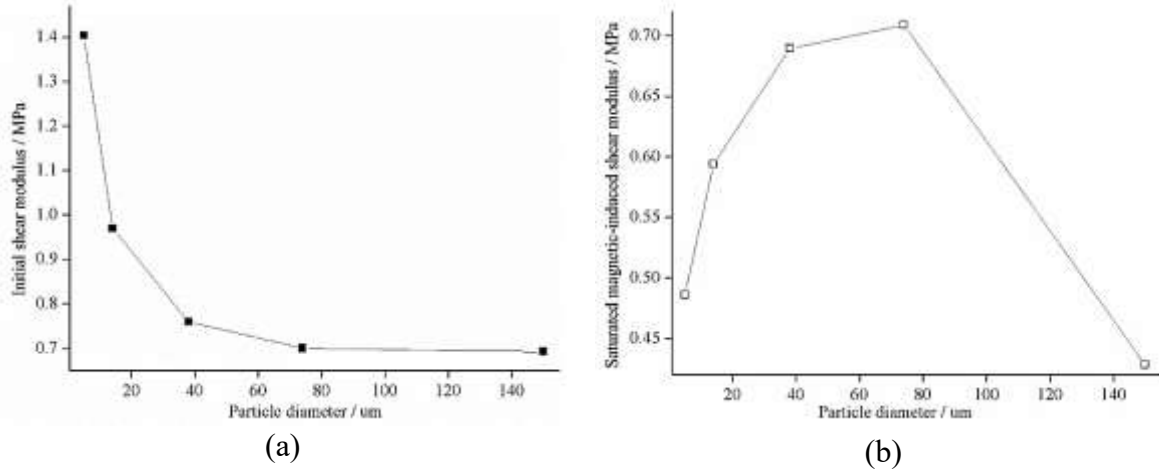


Figure 7: Shear behavior of MREs with 30% volume fraction of Iron particles with varying diameters 5 - 150 μm. (a) initial shear Modulus vs particle diameter, and (b) saturated magnetic-induced shear modulus ΔG vs particle diameter [37].

1.5 Microstructures and macroscopic properties of MREs

1.5.1 Microstructures of MREs

Fig.8 depicts typical SEM images of the microstructures of MRE with 11% volume fraction of carbonyl iron powder embedded in natural rubber at various magnifications. Figures 8(a) shows the images of the MRE sample cured in the absence of magnetic field. As depicted, the CIPs are randomly and uniformly dispersed in the matrix. Figures 8(b–f) are illustrations of the microstructures of MREs cured under magnetic field and how the magnetic particles are forming chain-like microstructures. It is clearly shown in these figures that curing under stronger magnetic field intensity leads to longer and denser magnetic particle-formed chains, stemming from the stronger magnetic interaction of neighbor particles. When the magnetic field is not strong enough, the magnetic particles may move within a limited range in the matrix, limiting their ability to produce microstructures in the form of short chains with small spaces between the chains. Intensifying the magnetic field during curing causes forming longer chains with wider space between, implying more anisotropic properties of MREs [41].

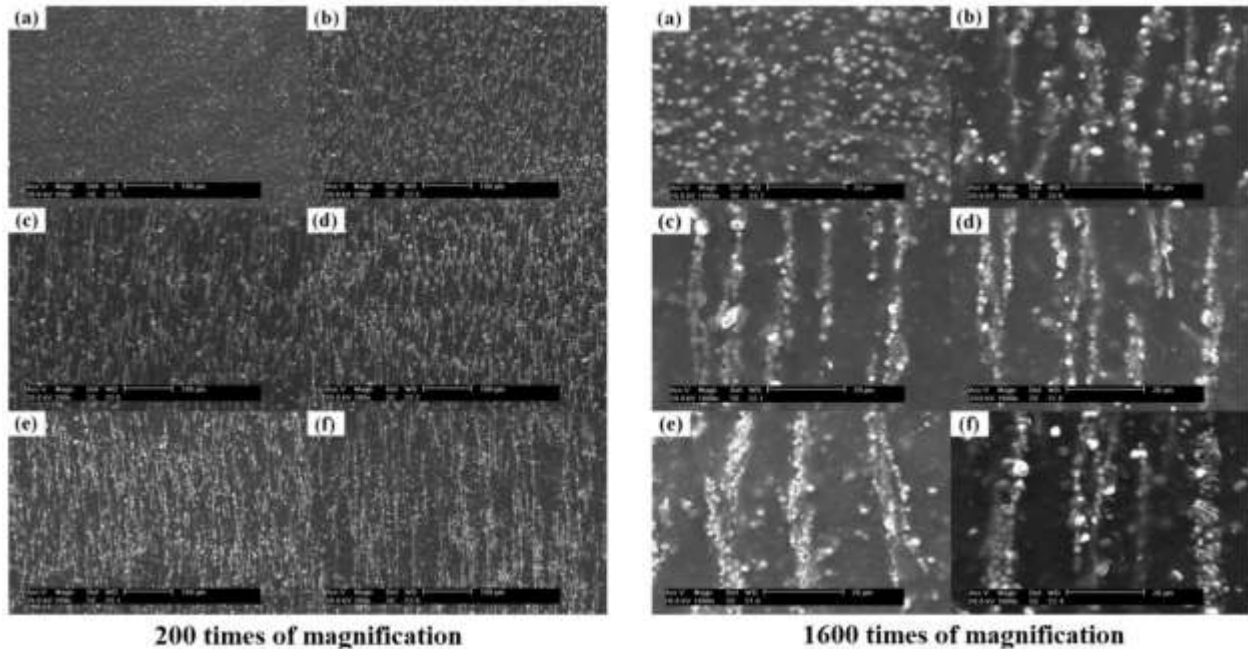


Figure 8: SEM images of MREs prepared under different magnetic flux densities B (a) No field, (b) 200 mT, (c) 400 mT, (d) 600 mT, (e) 800 mT, and (f) 1000 mT with two different magnification of 200 times and 1600 times [41].

1.5.2 Macroscopic properties of MREs

The most significant characteristic of MREs is that their macroscopic mechanical properties can be altered under the application of an external magnetic field. The magnetic field-induced change in the shear storage modulus of certain natural rubber-based MREs containing various weight fractions of CIPs can approach or exceed twice their initial magnitude. Fig. 9 shows the variation of storage modulus with respect to the applied magnetic flux density for natural rubber-based MREs containing various weight fraction of CIP. As it can be realized, the storage modulus of MREs, regardless of the weight fraction of CIP, increases by increasing magnetic flux density and reaches to saturation at magnetic flux density around 600mT [22]. Increasing the content of CIP substantially increases the storage modulus of MRE at saturation limit. For instance, increasing weight fraction of CIPs from 60% to 80%, increases the storage modulus by threefold from 2MPa to almost 6 MPa. Fig. 9 also shows the hysteresis loop stress-strain behaviour of MRE with silicon rubber as the matrix for different applied magnetic flux densities.

Results show that the area inside the loop, which represents the energy dissipation per cycle and thus damping, substantially increases by increasing the magnetic flux density. Results shown in Fig. 9 clearly show the controllable field-dependent storage and damping properties of MREs [42].

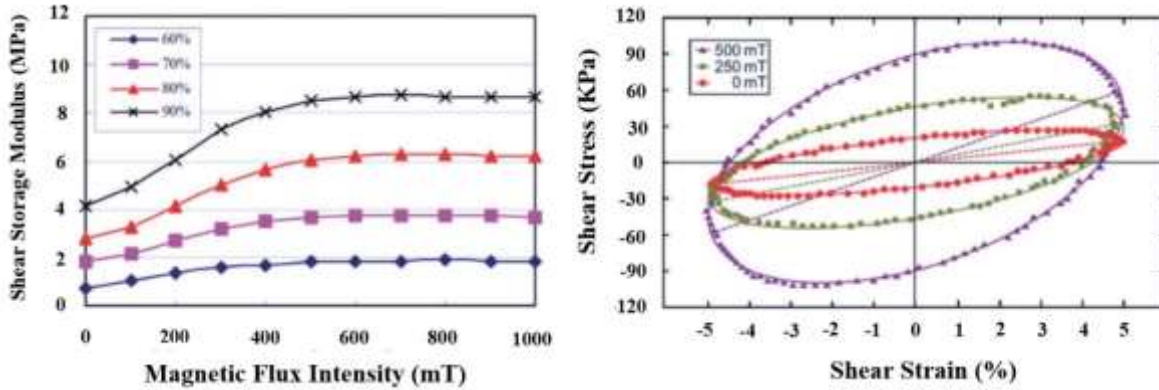


Figure 9 : Shear storage modulus of different natural rubber MRE samples consisting of 60, 70, 80, and 90% weight fraction of CIP (left) [22], and stress-strain loops of a silicone rubber MRE sample under different magnetic fields (right) [42].

1.6 Applications of MREs

MREs have several potential applications in engineering, particularly in the suppression of vibrations. In 1993, Kordonsky [43] suggested that magnetorheological effect can be a base of new adaptive devices and technologies. By possessing variable viscoelastic properties when subjected to an external magnetic field, MREs are ideal candidates for the development of MRE-based adaptive vibration absorbers and vibration isolators to attenuate vibration in a wide range of frequencies.

1.6.1 Vibration absorbers

As a passive method of vibration control, vibration absorbers are reliable and cost-effective to control vibration at the specified tuned frequency. The mass and stiffness of the passive vibration absorber are designed so that the natural frequency of the absorber matches that of the main system to provide anti-resonance in the system's overall response. However, the effective frequency range of conventional passive vibration absorbers is somewhat narrow. Moreover, passive vibration absorbers become ineffective under mistuned conditions. Since MREs have the ability to control their modulus with an applied magnetic field, they are ideal candidates for development of adaptive vibration absorbers in which their natural frequency can be varied using applied magnetic field to provide vibration control capability in broad range of frequencies. Ginder et al. [44] initially built an adaptive tuned vibration absorber with a rudimentary single-degree-of-freedom mass-spring system using MREs as adaptive spring components. Since then, significant research has been conducted on development of various types of MRE-based vibration absorbers. For instance, Deng et al. [45] focused on optimising an adaptively tuned vibration absorber (ATVA) using MREs, with field-dependent tunable modulus. Rasooli et al. [46] developed a novel semi-active adaptive tuned vibration absorber (SATVA), as shown in Fig. 10. The absorber includes a multilayer sandwich beam with MRE core layers and two U-shaped electromagnets attached to the upper and lower layers of the sandwich beam. The sandwich beam consists of two MRE layers, sandwiched between three steel layers. The MRE layers operate in pure shear mode and act as the variable stiffness unit. The sandwich beam is then incorporated with the two U-shaped electromagnets,

forming a closed loop magnetic circuit with the MRE layer serving as the gap. Electromagnets act as the oscillating active mass of the absorber to generate the magnetic field needed to activate the MRE layers. The SATVA can be attached to the host structure at one end, while the electromagnets oscillate freely.

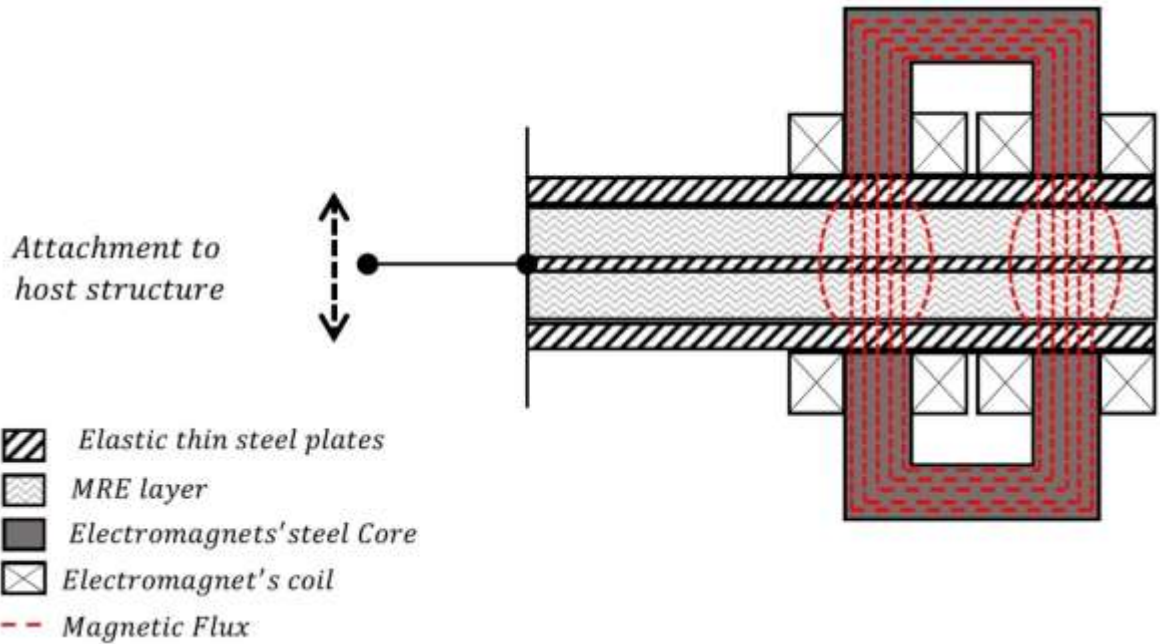


Figure 10: Schematic of the MRE-based semi-active adaptive tuned vibration absorber (SATVA) [46].

1.6.2 Vibration isolators

Vibration isolators are devices which can isolate an object, such as a piece of equipment, from the source of vibration. Vibration isolators can be categorized into two groups: base isolation and force isolation. Similar to vibration absorbers, passive vibration isolators are typically designed to isolate vibration in a very narrow frequency range and thus they lose their effectiveness under varied excitation conditions. By employing MREs, the natural frequency of vibration isolators can be modified in real-time by means of an external magnetic field. For instance, Fig. 11 is a schematic representation and also the fabricated prototype of MRE-based isolator operating under squeeze/elongation-shear mode studied by Tao et al. [47]. Their study reveals a relative increase of 66.57% in the stiffness and 45.55% in damping coefficient of the MRE-based isolator, under the application of a magnetic field. Moreover, thanks to the controllable stiffness and damping properties of MREs, the isolation transmissibility can be significantly reduced by 41.2%.

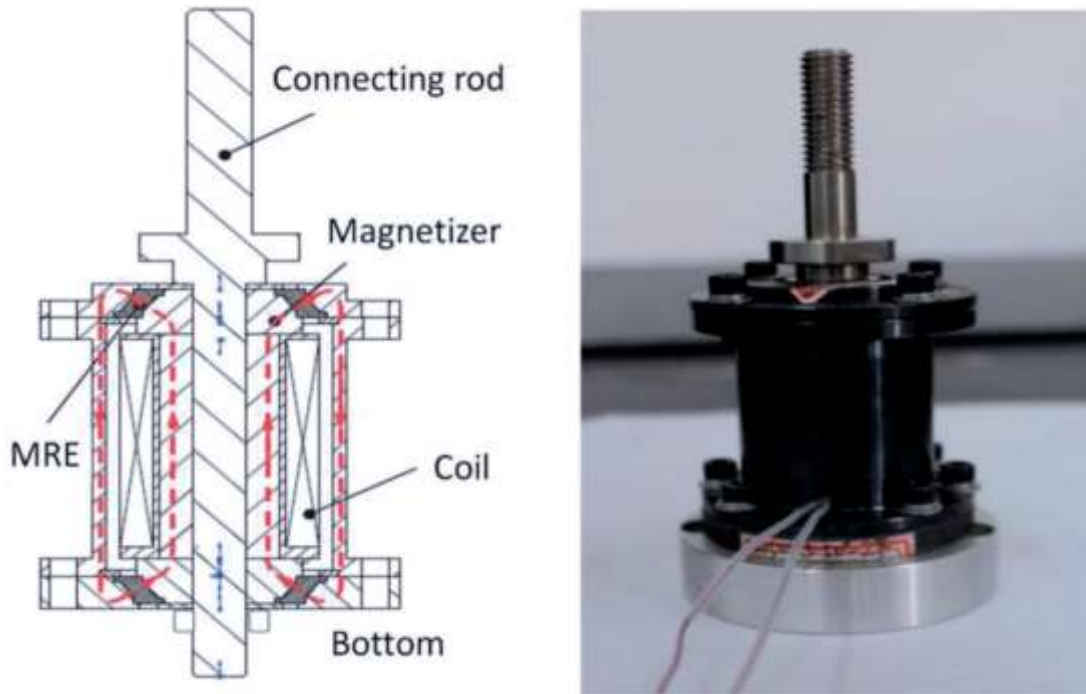


Figure 11: MRE-based isolator: cross-sectional view of designed layout (left) and the fabricated prototype (right) [47].

1.7 State-of-the-art on characterization of MREs

Within the extensive realm of research focused on MREs and their magnetic field induced viscoelastic behaviour, a thorough literature review plays a crucial role by providing essential guidance through the existing body of knowledge, shedding light on significant insights, and laying the groundwork for the current study's contribution to the field. Mark Jolly et al. [48] has pioneered the investigation on the mechanical response of anisotropic elastomer composites with embedded CIP under magnetic fields. In their study, the experimental data revealed significant changes in shear modulus of MREs with the application of magnetic fields, suggesting the potential of MREs for variable stiffness devices and adaptive structures. They also proposed a mathematical model for predicting the behaviour of anisotropic MREs. Davis [40] proposed a phenomenological model to predict the shear modulus of isotropic and anisotropic MREs, with and without magnetic field applied. His study suggested 27% of volume fraction of magnetic particles as the optimal content.

Dorfman et al. [49] examined deformation equations, for cylindrical tubes under radial magnetic fields. The results reveal increased stiffness in the azimuthal shear stress/strain response with higher magnetic field strength. Berasategi et al. [50] studied silicone-based MREs containing CIP concentrations ranging from 5% to 30% volume content in both isotropic and anisotropic fashions. Rheological analysis revealed changes in storage modulus and loss modulus as CIP content increased. High particle content in anisotropic samples exhibited a maximum MR effect of approximately 31% at low frequencies (1–2Hz). Vatandoost et al [51] investigated pre-strain effects on compression mode dynamic characteristics of MREs, considering both isotropic and

anisotropic types across various factors including particle volume fraction, frequency and magnetic flux density. Their results revealed that pre-strain significantly impacts the MRE's mechanical behavior, with elastic and loss moduli nonlinearly affected. The maximum relative MR effect of 2258% was obtained for elastic modulus in isotropic MREs containing 45% of CIP. They also proposed phenomenological models in order to predict the compressive moduli and stress-strain hysteresis of MREs. Shen et al. [52] investigated new methods of MRE fabrication using polyurethane and natural rubber, and also proposed a mathematical model for the stress-strain relationship in MREs, which aligned with experimental results. Huu Nam et al. [53] examined dynamic properties of isotropic and anisotropic MREs using experiments and numerical modeling. Their results showed that dynamic moduli decreased with increasing strain amplitude but increased with higher frequency and magnetic field strength, and anisotropic MREs outperformed their isotropic counterparts in terms of dynamic moduli and MR effect. Then, a four-parameter viscoelastic model was proposed which aligned well with experimental data for both MRE types. Syam et al. [54] conducted a finite element analysis on MREs' behavior at micro-scale, using COMSOL software. However, they used linear material model for silicone rubber as the matrix material. Their results showed increased stiffness in both linear and torsional modes under the application of magnetic field. Asadi Khanouki et al. [55] examined isotropic and anisotropic MREs both in experiments and microscale modeling, including different lattice structures. They fabricated different MRE samples with silicone rubber and various content of CIP, and conducted experiments to study their behavior under varied magnetic fields and validated their microscale modelling with the experimental results. Norouzi et al. [56] investigated the dynamic behavior of isotropic MREs subjected to harmonic tensile-compressive loads, considering varying magnetic fields, frequencies, and strain levels. They developed a generalized Maxwell viscoelastic model to describe stress-strain relationships based on input parameters. Dargahi et al. [31] fabricated six MRE samples with varying rubber matrix and ferromagnetic particle contents and conducted static and dynamic shear test on the samples. Their results showed a significant 1672% increase in storage modulus under 0.45T magnetic flux density. Ardehali et al. [57] experimentally characterized the viscoelastic properties of MREs, containing 15% NdFeB magnetic particle content, operating in shear mode under varying excitation frequency and magnetic flux density using a rotational magneto-rheometer. Moreover, a field-dependent phenomenological model was proposed to predict changes in storage and loss moduli under different conditions. Sun et al. [58] conducted a finite element analysis on MRE shear deformation under the application of magnetic field, using the concept of RVE in 2D fashion for anisotropic MREs in COMSOL. However, instead of using a B-H curve to take the saturation and nonlinearity into account, they used a linear method and assumed the relative permeability of CIP to be 100. Inspired by their work, Xu et al. [59] tried conducting 3D modeling of isotropic MREs in tensile mode under the application of magnetic field in COMSOL. However, they could not conduct modeling when assuming nonlinear hyper-elastic material models for the rubber material, and used linear material properties to describe the rubber behaviour and also linear magnetic properties for CIP. They conducted their modeling with magnetic field of 0T, 0.05 T and 0.28 T, but their model was not able to predict the MRE behaviour with acceptable accuracy compared to experiments. They proposed several methods to include nonlinearity, however none of which were successful. Kiarie et al. [60] adopted a 2D RVE approach using COMSOL to predict the magnetic field-

induced strain in MREs, they employed Mooney-Rivlin nonlinear material model for the host rubber, however, their problem did not include any mechanical load or displacement imposed on the RVE. Li et al [61] studied the magnetic field induced shear behaviour of MREs using a 2D RVE approach in COMSOL for both isotropic and anisotropic MREs, however, they assumed the magnetic particles (Hydroxy iron powder) to have a very high relative permeability of 5000, and silicone rubber behaviour as a linear elastic matrix.

1.8 Current Study and Contributions

The motivation behind this thesis stems from versatile applications of MREs, and the necessary expensive experimental procedures to characterize their behaviour under the effect of various factors, especially the volume fraction of CIP. Experiments on MREs involves fabricating different samples and repeating the experiments for each sample separately. Proposing a promising analytical model offers several benefits over experiments, including controlled simulations, broader scenario exploration, cost-effectiveness, and environmental sustainability. To the best of the authors' knowledge and reviewing the literature, a comprehensive FE model has not been successfully developed yet and studies have faced issues in taking the inherent nonlinear behaviour of MRE materials into account. As discussed in the previous section, some studies have investigated characterizing macroscale properties of MREs through microscale RVE approach. So, this was the key derive for us to investigate the RVE approach with the nonlinear inherent properties taken into account.

To achieve this, the first step is to define the appropriate RVE size for modeling the MRE. Once the optimum RVE size is determined, Periodic Boundary Condition (PBC) is chosen and defined to be imposed on the boundaries. Experiments are then carried out on host rubber samples (silicone rubber) to obtain the stress-strain data. This data will be used to formulate the Ogden strain energy to describe the nonlinear hyper-elastic behaviour of the rubber material. The other nonlinearity in the MREs is attributed to the magnetic behaviour of CIP, which is described through a B-H curve, considering the saturation, instead of using a high relative permeability as used in previous studies.

COMSOL Multiphysics offers the interaction of different physics in modeling, so it is chosen as the finite element software to develop the finite element model. The RVE is then generated in COMSOL in two configurations, 2D and 3D. The material properties are defined and pure shear deformation is incrementally applied on the RVE while PBC is imposed on the RVE boundaries. Simultaneously, a homogeneous magnetic field is created in the surrounding air domain perpendicular to the shear direction, and the Maxwell stress tensor is defined on the CIP inclusion. Different factors like CIP volume fraction, magnetic field intensity and host rubber's mechanical behaviour are investigated. The 2D model is able to describe the shear behaviour of MREs within $\pm 20\%$ difference with the experimental results in the literature [55], however, it is not capable of capturing the whole MR behaviour within a good agreement. The 3D model shows significant credibility in predicting the MRE shear behaviour with a relative error of less than 4%. The proposed RVE model has a substantial potential to be used for the prediction of MREs' mechanical behaviour, thus offering a reliable alternative to costly experiments.

1.9 Thesis Organization

This research dissertation comprises five chapters that methodically outline the research process and developments. In Chapter 1, an introduction to the thesis is presented, encompassing the context of MREs, their characteristics, their structure and fabrication process, and their diverse applications. This chapter also conducts a comprehensive literature review on the past efforts aimed at characterizing and modeling the performance of MREs under the application of magnetic field, while shedding light on the motivations driving the current thesis.

In chapter 2, a meticulous and thorough study of physical and mathematical concepts and methods has been provided. The concept of Representative Volume Element (RVE) has been rigorously explored, the associated boundary conditions are comprehensively explained, and the appropriate RVE size for modeling MREs is evaluated. This chapter also studies the governing equations and the interaction of mechanical and magnetic physics in this thesis project.

Chapter 3 outlines the fabrication of the MRE's host rubbers, silicone rubber Ecoflex 30 and Ecoflex 50, and the conducted experiments to obtain their mechanical characteristics. It follows by exploring the strain energy function and explaining the optimization carried out in order to identify the rubber behaviour through Ogden strain energy function. Carbonyl Iron Particle's mechanical and magnetic properties are also determined.

Chapter 4 delves into the Finite Element (FE) modeling of shear behavior in the developed MRE-RVE, executed using COMSOL, and thoroughly examines the ensuing results. This chapter is organized in two major sections for 2D and 3D modeling fashions and explores the credibility of the obtained results within each modeling scheme, validating them through comparison with experimental data from the literature. In this chapter the MRE-RVE's shear behaviour is explored under the application of different magnetic flux densities, and moreover, the effect of CIP volume fraction and the matrix stiffness is also investigated.

Finally, Chapter 5 provides a concise summary of the thesis's major findings and contributions, emphasizing their significance in the field. It also offers thoughtful recommendations for future research directions, underlining the importance of building upon the current work to advance the subject further.

Chapter 2: Methodology and Mathematical Concepts

In this chapter a thorough study will be conducted on the concept of Representative Volume Element (RVE), as outlined in the existing literature. Among the most important aspects of RVEs is determining their optimal size to accurately depict the structural characteristics representative of the entire macroscale structure. This chapter provides a comprehensive study on different fundamental factors influencing the RVE size determination, including the particles' shape, size and distribution. Considering the composition of non-overlapping hard spherical particles dispersed within extremely soft elastomeric matrices in MREs, the ideal RVE size for these materials is then evaluated.

The primary objective is to establish a uniform continuum that aligns with the mechanical behavior of the real heterogeneous material. Within any numerical homogenization methodology, a pivotal phase revolves around the appropriate choice of microscopic boundary conditions. Consequently, this study delves into an investigation of various microscale boundary conditions to determine the most suitable one for describing RVEs. Periodic Boundary Conditions (PBC) emerge as the most appropriate choice. The study follows by conducting an in-depth investigation on PBC's fundamental physical and mathematical concepts, particularly in homogenization method, in order to evaluate the macroscale effective elastic properties, both in 2D and 3D configurations.

Given that MREs operate under coupled magneto-mechanical loading conditions, this chapter continues by delving deeper into examining the fundamental magnetic equations incorporated in this study. Finally, the governing equations are established to be considered in this study.

2.1 Representative Volume Element (RVE):

A fundamental goal in the field of heterogeneous materials physics is to ascertain the effective properties of these materials by leveraging the fundamental laws and analyzing the spatial distribution of their components. The pursuit of determining these effective properties, like mechanical properties or thermal conductivity, has led to the continual advancement of sophisticated and efficient homogenization techniques. Among these techniques, Representative Volume Element (RVE) homogenization stands out as a method that utilizes a statistically homogeneous representation of heterogeneous materials at microscale to derive their effective properties on a macroscale. A fundamental phenomenon that has been a research topic for years is the determination of the proper size of RVE. Many researchers have suggested different aspects to be considered in evaluation of the RVE size. The following are some prominent proposed definitions of RVE.

Hill (1963) defined RVE as a microscale specimen that exhibits structural characteristics that are representative of the entire mixture on average, and contains an adequate number of inclusions [62]. Hashin (1983) stated that the RVE should possess adequate dimensions to encompass a substantial amount of microstructural information, ensuring its representativeness. Nonetheless, it is crucial for the RVE to maintain a significantly smaller size compared to the macroscopic body [63]. Evesque (2000) suggested that the dimensions of the RVE should be sufficiently large

compared to the size of individual grains to accurately determine global properties such as stress and strain. However, the dimensions should also be sufficiently small to avoid obscuring macroscopic heterogeneity [64].

A more pragmatic definition of the RVE may be found within the context of homogenization. In this paradigm, a numerical RVE is defined as the minimal volume element that exhibits an equivalent target attribute or behaviour to that of the whole material at a macroscopic scale. Nevertheless, it is evident from these definitions that the RVE must include a substantial amount of information about the microstructure and must be much smaller in size compared to the macroscopic dimensions of the structure. It is necessary to adequately define the statistical characteristics associated with random microstructures in order to ensure comprehensive understanding [65].

As discussed, the most controversial phenomenon in RVEs, has found to be size determination. Various efforts have been undertaken to measure the dimensions of the RVE using statistical and numerical approaches, considering the effect of various parameters such as the desired outcome properties, i.e. thermal or mechanical properties, inclusion's shape and volume fraction, inclusions' distribution type and etc. According to Madi et al. [66] the researchers reached the conclusion that the two-dimensional RVE exhibits a bigger RVE size compared to the three-dimensional RVE. Additionally, it was observed that the RVE size seems to be lower in the nonlinear cases as opposed to the linear cases.

El Moumen et al. [67] demonstrated that the RVE dimensions of composites reinforced with randomly distributed particles exhibit an increase as the geometric form of the particles gets more intricate. The smallest RVE size can be attributed to composites including spherical particles. The absence of preferred orientation in the case of spheres might account for this phenomenon.

Moreover, the study conducted by Dirrenberger et al. [68] has shown that some microstructures, characterised by the presence of enormous fibres or fibres of infinite length, may result in very large RVE sizes or even the absence of an RVE altogether. This phenomenon, referred to as non-homogenizability according to Auriault's definition [69], highlights the inability to achieve homogenization in such cases. Fig. 12 shows the scale fluctuation of the RVE size. As shown in this figure, the larger RVE is characterised by significantly sized fibres, while the smaller RVE consists of spherical particles. It is important to note that the relative differences in physical attributes are maintained the same in both cases.

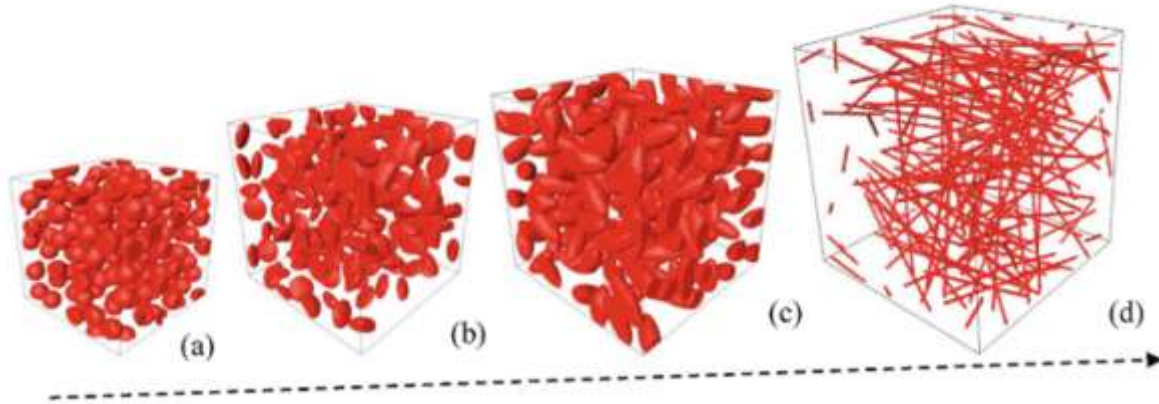


Figure 12: The RVE size regarding different reinforcement particle shapes: (a) spherical particles, (b) oblate spheroids, (c) prolate spheroids and (d) gigantic fibers [65].

It is noteworthy to acknowledge that the repulsion distance between adjacent particles also influences the size of the RVE. For instance, a study conducted by El Moumen et al. [70] revealed that the RVE microstructures using hard sphere models, where particles can not overlap, is 13 times smaller than the RVE size of microstructures utilising Boolean models, where spheres may overlap. Fig. 13 depicts the morphological characterization of the impact of repulsion distance on the RVE size, as described in their study.

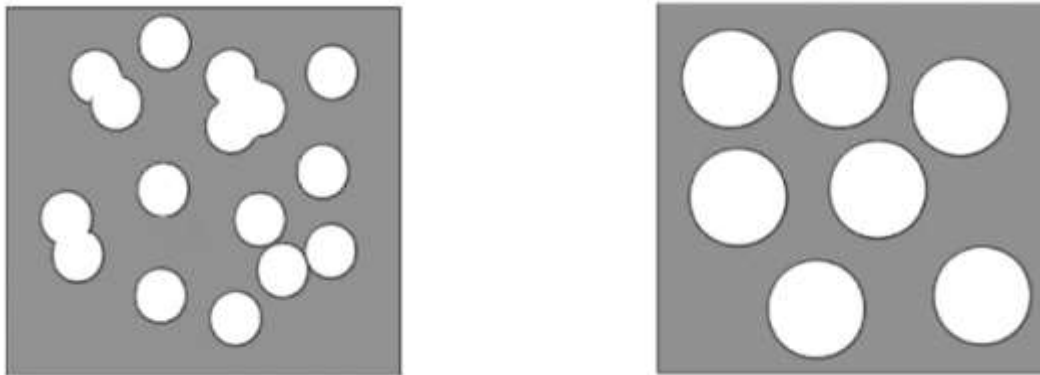


Figure 13: Morphological equivalence between RVEs of overlapping and non-overlapping spheres [70].

The study on RVE size conducted by El moumen et al [65], revealed that the hard spheres model fails to accurately represent the microstructure with a large volume percentage due to the imposed jamming limit. The model yields a maximum volume percentage of 27%.

2.2 The RVE Size for Models Containing Hard Particles

El moumen et al [65] adopted a combined numerical-statistical approach in order to investigate the variation in the RVE size with respect to the parameters of the microstructure. In their study, a computational methodology was presented for determining the variation of RVE size in random

microstructures. For this purpose, they used the fundamental concept of the integral range “ A ” in the context of composite materials. This geostatistical parameter is used to relate the size of the RVE with other microstructure parameters and was defined by previous researchers [70-72].

It is feasible to establish an integral range that provides insights into the size of the domain for which the parameters measured within this volume exhibit a high degree of statistical representativeness. The integral range depends on the particle size in RVE and is independent of the RVE volume, V_{RVE} [71]. It is chosen to be sufficiently large in order to maintain the stationary nature of the field, hence, minimising the impact of boundary conditions [72]. In the case of hard particles, however, it depends on the volume of inclusions inside the RVE [70].

RVE is contingent upon the volume of a single inclusion inside the RVE, which is integrated in the particle volume fraction, denoted as ϕ . The integral range for random microstructures with a volume fraction ϕ may be expressed as [67]:

$$A = \frac{\phi}{V_{RVE}} \quad (1)$$

To obtain an accurate estimation of the effective properties, it is essential to establish a correlation between the size of the RVE and the various morphological, mechanical, and thermal factors associated with microstructures. The primary parameters include the mechanical characteristics of different phases, the particles volume fraction ϕ , and several statistical factors. For a stationary random function Z , the variance of Z , $D_Z^2(V)$, over the volume V is attainable as a function of the integral range A and the point variance S_Z^2 [65].

$$D_Z^2(V) = S_Z^2 \frac{A}{V} \quad (2)$$

In the comprehensive study conducted by El moumen et al [65], they examined a stochastic microstructure composed of two distinct phases, denoted as F_1 and F_2 . The phase F_1 occupies a volume percentage of ϕ , while the phase F_2 occupies a volume fraction of $(1 - \phi)$. Each phase has distinct real characteristics, namely z_1 for phase F_1 and z_2 for phase F_2 . The point variance S_Z^2 of the random variable z in the context of a two-phase material is provided as:

$$S_Z^2 = \phi (1 - \phi)(z_1 - z_2)^2 \quad (3)$$

Given the current context, whereby the mechanical properties are represented as the random variable z , and using Eqs. (2) and (3), the volume variance, $D_Z^2(V)$, can be evaluated as:

$$D_Z^2(V) = \phi (1 - \phi)(z_1 - z_2)^2 \frac{A}{V} \quad (4)$$

Where, $D_Z^2(V)$ is the variance of the volume V , and A is the integral range. To determine the RVE parameters, the number of realizations n and the absolute error ε_{abs} were used to express $D_Z^2(V)$ as follows [61]:

$$4D_z^2(V) = \varepsilon_{abs}^2 n \quad (5)$$

It should be acknowledged that the determination of the size of the RVE involves defining the volume at which the number of realisations is equivalent to 1 [73].

$$n(V = V_{RVE}) = 1 \quad (6)$$

Therefore, from Equations (1) and (4) – (6), we can write:

$$V_{RVE} = \frac{4 \phi^2 (1 - \phi)(z_1 - z_2)^2}{\varepsilon_{abs}^2 V_{RVE}} \quad (7)$$

By using Equation (7), we can investigate the variation of volume of the RVE with respect to the particle volume fraction (ϕ) and the contrast ratio (c) in mechanical characteristics, which is defined as the ratio of mechanical properties, z_2 to z_1 in phases F_2 and F_1 , respectively. The representativity of the estimated characteristics in random microstructures may be determined by considering the volume size, with respect to the desired error ε_{abs} , as follows:

$$V_{RVE} = \sqrt{\frac{4 \phi^2 (1 - \phi) z_2^2 (1 - c)^2}{\varepsilon_{abs}^2}} \quad (8)$$

Hence, the relationship between the size of the RVE and the volume fraction (ϕ) and contrast ratio (c) in random microstructures may be described as the fluctuation of the two-variable function $f(c, \phi) = V_{RVE}(c, \phi)$.

$$V_{RVE}(c, \phi) = \frac{2 z_2 |1 - c| \phi \sqrt{(1 - \phi)}}{\varepsilon_{abs}} \quad (9)$$

where, as mentioned before, the contrast ratio c is defined as $c = z_2/z_1$, in which z_2 represents the matrix property (phase F_2).

Introducing the relative error as $\varepsilon_r = \varepsilon_{abs}/z_2$, the final expression for RVE size would be:

$$V_{RVE}(c, \phi) = \frac{2 |1 - c| \phi \sqrt{(1 - \phi)}}{\varepsilon_r} \quad (10)$$

Eq. (10) provides a clear relationship between the representative volume element (RVE) of random microstructures and both the volume fraction and contrast ratio, while also accounting for desirable and fixed relative error.

2.3 Determining the RVE Size for MREs with Spherical Particles

For MREs, two phases include soft elastomeric phase (F_2) impregnated with hard solid spherical inclusions, phase (F_1), represented by the micron-sized Carbonyl Iron Powder (CIP). Thus, for MREs, the contrast ratio c which here represents the ratio of modulus of rubbery matrix to solid inclusions is nearly negligible compared with unity. Thus, using Eq. (10) and assuming $c = 0$, the RVE size can be determined for different particle volume fractions and the desired relative error. Tuning the aforementioned parameters to a negligible relative error, the equation leads us to an RVE with one CIP inclusion in a cubic rubber matrix, which is the same RVE size presented by Davis [40], as shown in Fig. 14.

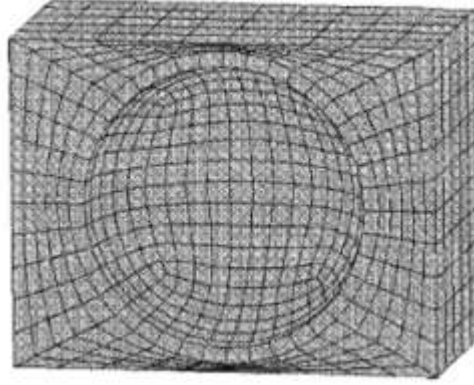


Figure 14: The MRE-RVE, containing finite element mesh used in calculation of shear modulus [40].

As discussed in Davis' study [40], the model considers two consequent spheres in MRE as presented in Fig. 15. Where R is the radius of the particles (assumed to be identical) and the gap between the two particles is denoted as $2w$.

For a rectangular prism (Cuboid) unit cell with square base, containing one particle as shown in Fig. 16, to determine the stress resulting from a shear deformation in the square plane, let us consider the x and y axes to be aligned with the edges of the square plane, and z direction along the assumed chain of subsequent particles. For this unit cell with width and height of D and $(2R + 2w)$, respectively, the volume fraction of particles can be obtained as:

$$\phi = \frac{4\pi/3 R^3}{(2R + 2w)D^2} \quad (11)$$

When $D = (2R + 2w)$, the unit cell would have a simple cubic arrangement. It is noted that, when the gap between the particles ($2w$) is reduced while keeping the same volume fraction, the model represents chain-like MRE model.

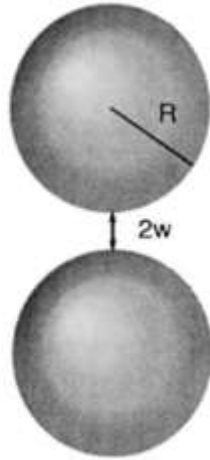


Figure 15: The gap region between two consequent particles, with radius R and the gap being $2w$ [40].

Davis [40] investigated the relationship between shear stress and shear strain in a filled elastomer material including spherical iron particles. The finite element analysis was conducted using the ABAQUS software, to simulate a pure shear deformation, without the presence of an externally induced magnetic field.

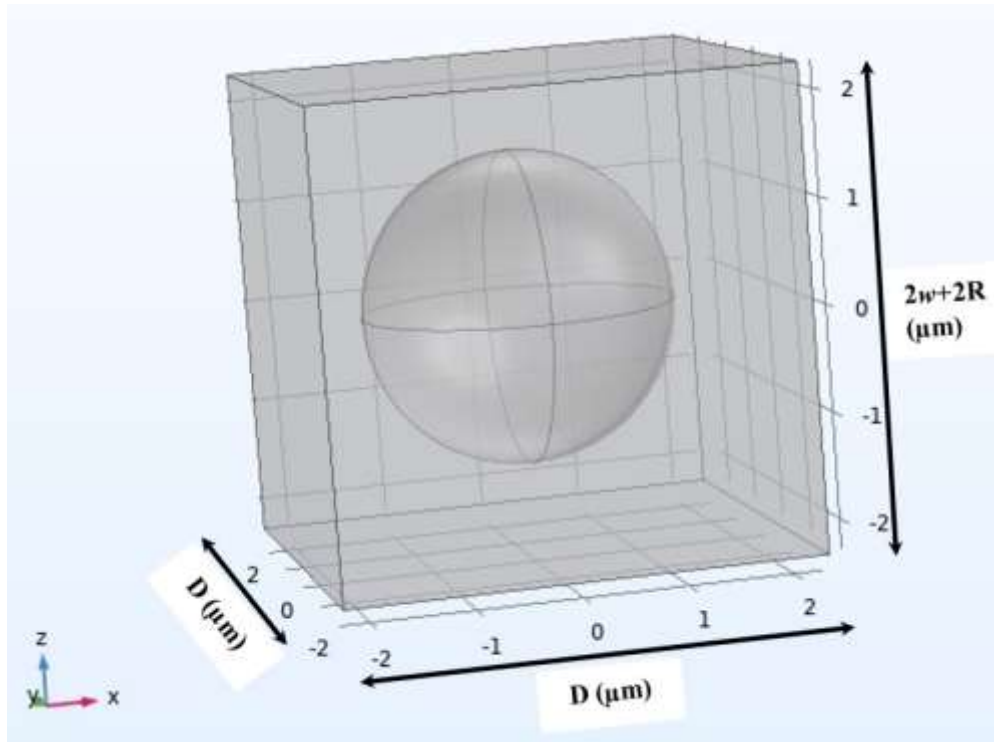


Figure 16: The schematic representation of a unit cell with one particle included.

Fig.17 illustrates the effect of the particles gap on the shear modulus of the MRE unit cell model while the volume fraction of particles is kept to be 0.27. The term "SC" represents a configuration in which particles are arranged in a simple cubic manner, whereas the dashed line labelled "matrix" refers to the unfilled elastomer. The study also examines the effect of particle volume fraction on the shear modulus of the MRE, concluding that the optimum volume fraction is roughly 27%, as shown in Fig. 18.

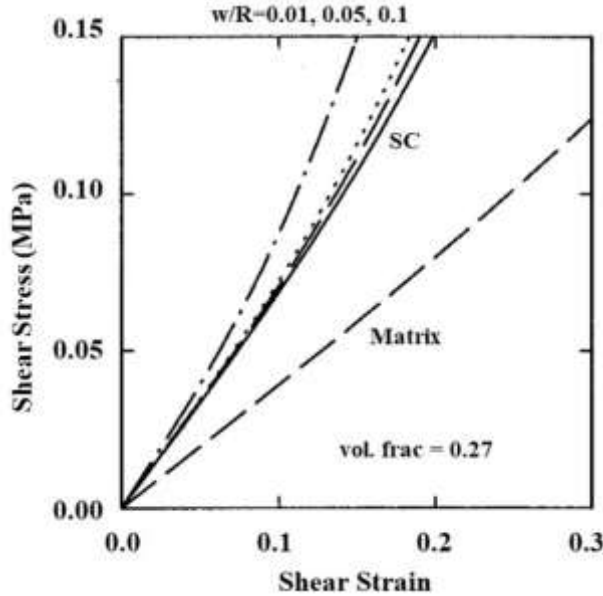


Figure 17: The effect of the gap between two subsequent particles on shear modulus of MRE as the ratio of the gap to particle's radius (w/R) [40].

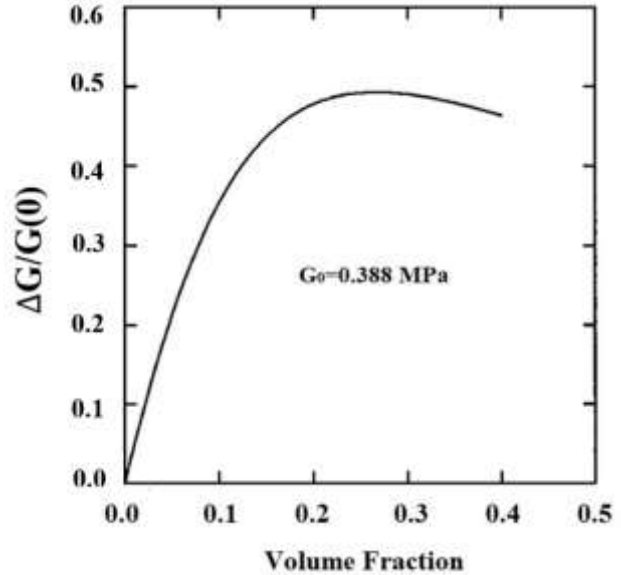


Figure 18: The change in modulus ($\Delta G = G - G_0$) at saturation, normalized to the initial modulus in the absence of the magnetic field (G_0), with respect to volume percentage of particles [40].

2.4 RVE Boundary Conditions

As of already addressed in the concept of RVE, the main goal is to define an equivalent homogeneous continuum that matches the average mechanical response of the actual heterogeneous material. In any numerical homogenization approach, a critical step involves the selection of appropriate microscopic boundary conditions. These conditions are applied to the RVE, and subsequently, the RVE's averaged response is used to determine effective material properties.

The commonly employed boundary conditions in micromechanics fall into two categories of uniform boundary conditions, as kinematic uniform boundary conditions, also known as Dirichlet or essential boundary conditions, where uniform displacements are enforced on the boundary, and static uniform or Neumann boundary conditions, where uniform tractions are prescribed along the sample's boundaries. Neumann, also known as Traction Boundary Conditions, basically specify the distribution of forces or stresses acting on the RVE's boundary, while Dirichlet, also known as Displacement Boundary Conditions, specify how points on the RVE's boundary respond to external forces or constraints [74]. According to Hill [62], an RVE is considered well-defined

when the responses under Dirichlet and Neumann boundary conditions coincide. This convergence is a crucial criterion in ensuring the accuracy and reliability of homogenization results.

2.4.1 Displacement Boundary Conditions (DBC)

DBC describe how the displacement field behaves at the boundaries of the RVE. They are typically expressed as:

$$u_i(\Gamma) = \varepsilon_{ij}^0 x_j, \forall x_j \in \Gamma \quad (12)$$

Here, ε_{ij}^0 represents a uniform strain that is independent of the location x_j , and Γ represents the surface boundary of the RVE. This condition implies that the material experiences the same strain throughout the entire boundary.

2.4.2 Traction Boundary Conditions (TBC)

TBCs specify how stress or traction is distributed on the RVE's boundaries and can be expressed as:

$$t_i(\Gamma) = \sigma_{ij}^0 n_j, \forall x_j \in \Gamma \quad (13)$$

In this equation, σ_{ij}^0 represents a uniform stress independent of location x_j , n_j is the unit normal vector to the boundary Γ at the point x_j , and t is the traction.

It's important to note that under both DBCs and TBCs, the unit strain or stress can be applied component-by-component to the RVE. This means that one can apply strains or stresses independently in different directions. The resulting stresses or strains lead to the determination of stiffness and compliance properties, respectively, which are essential for understanding how the material responds to external loading conditions.

In addition to the uniform boundary conditions mentioned earlier, researchers have also introduced mixed boundary conditions [75–77]. These were proposed because achieving uniform boundary conditions in experimental setups can be challenging. For a more visualized understanding of mixed boundary conditions, one can consider a specimen, where one part of it undergoes prescribed displacements while forces are prescribed on remaining parts. Studies have indicated that mixed boundary conditions often yield more accurate approximations of effective material properties compared with uniform conditions.

Furthermore, researchers have also developed Periodic Boundary Conditions (PBC) [78–80]. These conditions are typically applied to unit cells in cases where the heterogeneous material exhibits a periodic structure. For instance, Terada et al. [80] demonstrated that even for general heterogeneous materials lacking exact geometric periodicity, periodic boundary conditions with relatively small unit cell sizes can provide reasonable estimates of the effective properties. In a research conducted by Van der Sluis et al. [81] a thorough study was conducted on Mixed and

Periodic boundary conditions and their study showed that PBC contributes to better results and is less sensitive to the RVE size or inclusion position in the unit cell.

2.4.3 Periodic Boundary Conditions (PBC)

Research has demonstrated that Periodic Boundary Conditions (PBC) yields more precise effective moduli estimates compared with other conventional boundary conditions [81]. Okereke et al. [82] proposed a method for applying periodic boundary conditions to 3D RVEs. The method which was based on the work conducted originally by of Van der Sluis et al. [81], who applied PBC to 2D RVEs. In the following, PBCs in 2D and 3D configuration are discussed.

2.4.3.1 Periodic Boundary Conditions in 2D

For their study on 2D boundary conditions, Van der Sluis et al. [81] investigated a plate featuring a regular square unit with spherical inclusions under tensile loading. Two types of unit cells were established: a symmetric unit cell and an asymmetric unit cell (Fig.19). The goal was to ensure that these unit cells ultimately yield an identical set of effective parameters for the equivalent homogeneous continuum, while perfect bonding was assumed to exist between the two phases.

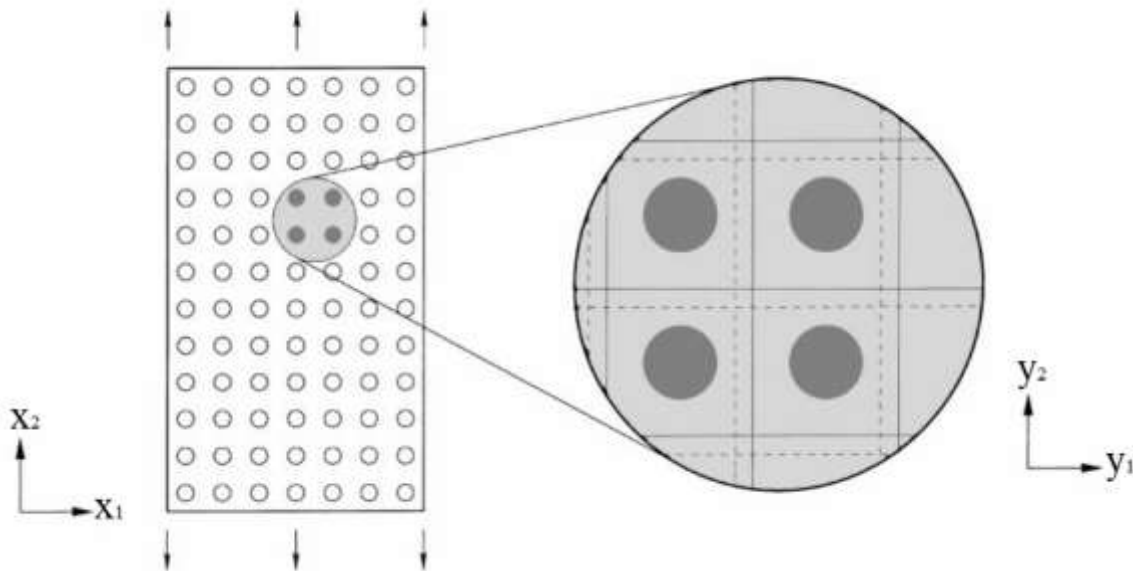


Figure 19: Selected unit cells to analyze a heterogeneous material behaviour under tensile loading 1) Symmetric unit cell (solid line) and 2) asymmetric (dashed line) [81].

Considering the periodic structure of the macroscopic body, a square unit cell of size “ a ” could be defined where; $R = \{(y \in \mathbb{R}^2) \mid -a/2 < y_i < a/2 ; i = 1, 2\}$.

Assuming a two-dimensional orthonormal base (e_1, e_2) aligned with the axes (x_1, x_2) , both boundary pairs Γ_1 and Γ_2 comprise opposing edges [83]. For each boundary pair Γ_p , compatibility

is essential, in line with the periodicity assumption. This implies that the deformation of each boundary pair is identical, and the stress vectors have opposite signs on each pair [78, 79]. Smit et al. [84], derived the suitable displacement boundary conditions as:

$$\begin{aligned} u_{12} - u_{v_4} &= u_{11} - u_{v_1} \\ u_{22} - u_{v_2} &= u_{21} - u_{v_2} \end{aligned} \tag{14}$$

Where, u_{ij} denotes the displacement vector associated with any material point situated on the corresponding boundary Γ_{ij} , while u_{v_i} represents the displacement vector attributed to each vertex v_i , as illustrated in Fig. 20.

Furthermore, when considering vertex v_3 , a constraint equation can be established by utilizing either of the two equations provided in Eq. (14) as:

$$u_{v_3} - u_{v_2} = u_{v_4} - u_{v_1} \tag{15}$$

Eq. (15) essentially defines the relationship between the displacement vectors at vertex v_3 and the surrounding vertices, which plays a crucial role in ensuring compatibility and consistency within the considered model.

To eliminate rigid body motions, it is necessary to impose $u_{v_k} = 0$ for any k within the set $k \in \{1,2,4\}$. This requirement ensures that rigid body translations or rotations are prevented. Upon analyzing the periodicity equations (14) and (15), it becomes evident that certain entities are considered as retained (independent), including Γ_{11} , Γ_{21} , v_1 , v_2 and v_4 . Conversely, other entities are deemed tied (dependent), comprising Γ_{22} , Γ_{12} and v_3 . Hence, it will be sufficient to prescribe displacements for the three retained vertices, to effectively control and constrain the behavior of the entire system while eliminating rigid body motions.

2.4.3.2 Computational homogenization in 2D

In a general context, macroscopic quantities are typically computed as averages of their corresponding microscopic state variables. Within deterministic theories proposed in the literature, this averaging process involves calculating the average of a quantity ψ over the region R occupied by the unit cell [81]. Mathematically, this averaging operation is represented as:

$$\langle \psi \rangle (x) = \frac{1}{S} \int_R \psi(x, y) dy ; S = \int_R dy \tag{16}$$

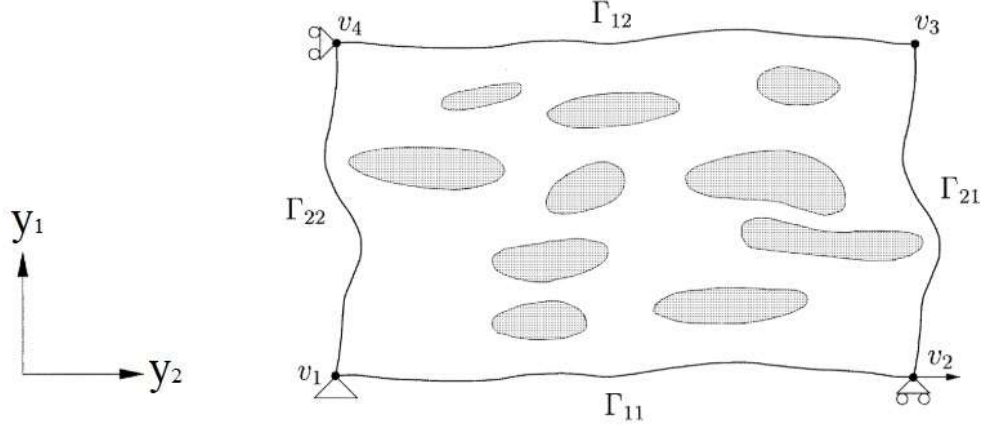


Figure 20: Periodically deformed 2D unit cell, with boundaries Γ_{ij} and vertices v_i [81].

Here, x pertains to the coordinate system of the macroscopic body, and y corresponds to the coordinate system within the unit cell (as illustrated in Fig.19). With this specific definition of the averaging operator, we can establish the following micro-macro relations for the total stress and strain tensors:

$$\begin{aligned}\sigma_{ij}(\text{macro}) &= \langle \sigma_{ij} \rangle (x) \\ \varepsilon_{ij}(\text{macro}) &= \langle \varepsilon_{ij} \rangle (x)\end{aligned}\tag{17}$$

Where, $\sigma_{ij}(\text{macro})$ and $\varepsilon_{ij}(\text{macro})$ signify the macroscopic total stress and strain tensors, respectively, while $\langle \sigma_{ij} \rangle (x)$ and $\langle \varepsilon_{ij} \rangle (x)$ represent the corresponding microscopic averages.

It should be considered that, during a tensile test conducted on the unit cell, the equivalent stresses in the unit cell must not exceed the local yield limit of the matrix material. Utilizing the averaged elastic constitutive equations (17), we obtain the following expressions for the affective elastic properties:

$$E_{11}^{eff} = \frac{\sigma_{11}(\text{macro})}{\varepsilon_{11}(\text{macro})}, \quad \nu_{12}^{eff} = -\frac{\varepsilon_{22}(\text{macro})}{\varepsilon_{11}(\text{macro})}\tag{18}$$

Where, E_{11}^{eff} is the effective Young's modulus, and ν_{12}^{eff} denotes the effective Poisson's ratio.

2.4.3.3 Periodic Boundary Conditions in 3D

In their study, Okereke et al. [82] introduced the concept of Ω_{RVE} as the bounding domain of a 3D RVE, featuring a periodic microstructure. This domain contains both fiber and matrix constituents and typically takes the form of a cube with dimensions represented by 'D'. Ω_{RVE} is defined by six surfaces, ensuring that any two parallel surfaces (e.g., X_{pos} and X_{neg}) always maintain parallel

alignment along either the x, y, or z-axes. Specifically, the X_{pos} surface corresponds to the y-z plane situated at the maximum x-axis cubic dimension (i.e., $x = D$), while the X_{neg} surface is located at the minimum x-axis cubic dimension (i.e., $x = 0$), as illustrated in Fig.21.

Each of these surfaces consists of nodes, and nodes located on the X_{pos} surface are referred to as ' $X_{posNodes}$ '. Similar terminology applies to the other five faces. Within this domain, edge nodes as nodes shared by two intersecting surfaces are identified. Assuming that the 3D domain, Ω_{RVE} , exists in the three-dimensional real space (R^3), the set of nodes for a specific surface is defined as S_{np} , where 'n' represents the reference frames (X, Y, Z), and 'p' encompasses either the positive or negative faces along a given axis. Consequently, we can describe the set of surface nodes as follows:

$$S_{\Omega_{RVE}} = \{S_{XPOS} \cup S_{XNEG}\} \cup \{S_{YPOS} \cup S_{YNEG}\} \cup \{S_{ZPOS} \cup S_{ZNEG}\} \quad (19)$$

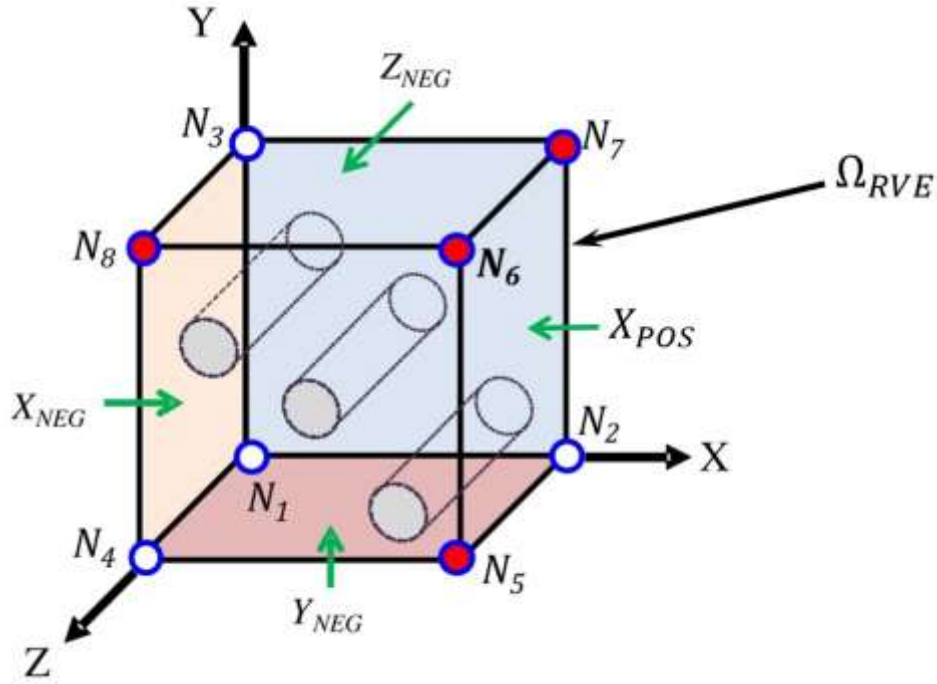


Figure 21: A typical 3D RVE, containing fibers, with the bounding domain of Ω_{RVE} [82].

As a consequence of Equation (19), no group of nodes is common to any two parallel surfaces. Instead, a collection of edge nodes should arise from the intersection of orthogonal surfaces. Similarly, corner nodes, denoted as N_1, N_2, \dots, N_8 , are defined as the nodes resulting from the intersection of the three mutually perpendicular surfaces at any of the eight vertices within the 3D RVE domain.

When applying periodic boundary conditions to the 3D RVE domain, Ω_{RVE} , it should be ensured that all six surfaces and twelve edges of the domain undergo uniform deformation. This condition

is met when any pair of surfaces (e.g., S_{XPOS} and S_{XNEG}) or pair of edges are kinematically tied. Various approaches exist to implement this requirement within a numerical framework, including those for periodic meshes [84], and those for non-periodic meshes [85].

Referring to Fig. 21 and considering the 3D RVE domain, Ω_{RVE} , the position vector for surface nodes is established as: $U_i^{S_{np}}$, where S_{np} is as previously defined, and 'i' ranges from 1 to N, with N representing the total number of nodes per surface. Additionally, the position vector for corner nodes is established as: U^{N_j} , where the corner nodes are labeled as $j = 1, 2, \dots, 8$. Within this context, four reference nodes are then identified, namely $N_1, N_2, N_3,$ and N_4 , referred to as "retained nodes", (marked as unfilled circles in Fig.21). These retained nodes serve as points of focus for prescribing the necessary boundary conditions to replicate a desired load scenario. The remaining corner nodes, N_5 through N_8 (marked as red circles in Fig. 21), and surfaces, denoted as ($U_i^{S_{XPOS}}, U_i^{S_{YPOS}}, U_i^{S_{ZPOS}}$), are referred to as "tied" or "slave" nodes and surfaces, respectively. These tied entities are dependent on or "slaved" to any displacements or loads applied to the retained nodes. Consequently, the mathematical expressions governing the imposition of periodic deformation on all nodes in the three dimensions of the 3D RVE domain can be mathematically described as follows:

$$\begin{aligned} U_i^{S_{XPOS}} - U_i^{S_{XNEG}} - U^{N_2} + U^{N_1} &= 0 \\ U_i^{S_{YPOS}} - U_i^{S_{YNEG}} - U^{N_3} + U^{N_1} &= 0 \\ U_i^{S_{ZPOS}} - U_i^{S_{ZNEG}} - U^{N_4} + U^{N_1} &= 0 \end{aligned} \quad (20)$$

Enforcing periodic boundary conditions requires stress equilibrium across opposite surfaces within the RVE domain. For every surface (S_{np}) in the 3D RVE, a specific unit outward normal vector is defined as (n_{np}). Assuming that the domain is experiencing stress, the condition for stress equilibrium across opposing pairs of surfaces is achieved when:

$$\begin{aligned} \sigma n_{XPOS}(y, z) &= -\sigma n_{XNEG}(y, z) \\ \sigma n_{YPOS}(x, z) &= -\sigma n_{YNEG}(x, z) \\ \sigma n_{ZPOS}(x, y) &= -\sigma n_{ZNEG}(x, y) \end{aligned} \quad (21)$$

where, σ is the stress tensor.

Considering the described periodic boundary condition approach, where all nodes except the retained nodes are constrained, only the retained nodes serve as points for applying various load scenarios within the 3D RVE domain, Ω_{RVE} . To facilitate uniaxial and shear load cases, we need to apply specific constraints to these retained nodes.

For uniaxial loading, let us consider the 3D cubic RVE domain shown in Fig. 22, where the retained nodes are $N_1, N_2, N_3,$ and N_4 , while N_1 is restricted to have zero displacement in order to prevent rigid body motions. Uniaxial loads can be applied along the x-, y-, or z-axes, as depicted in Fig. 22 To create a tensile uniaxial load along any of these axes, prescribed positive displacements (δ) is applied to nodes $N_2, N_3,$ or N_4 , respectively. Conversely, compressive loads result from applying negative displacement values ($-\delta$).

In the same fashion, for shear loading the retained node N_1 is set to zero displacement to prevent rigid body motions and nodes N_2 to N_4 are utilized to impose the desired shear load case. Fig.23 provides a schematic representation of the shear load cases and the associated nodal constraints.

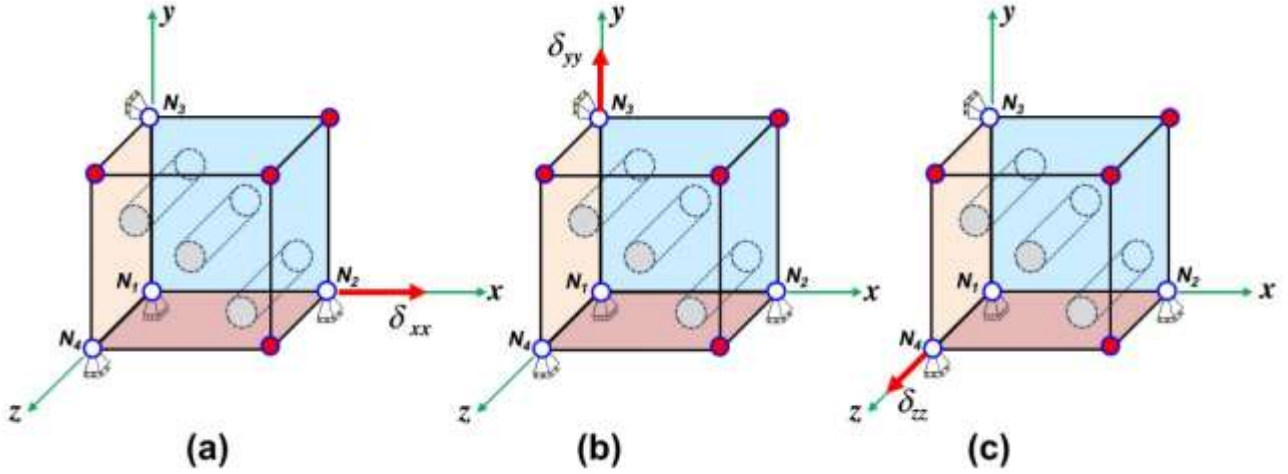


Figure 22: Tensile loading applied to 3D RVE in a) X , b) Y and c) Z direction, respectively [82].

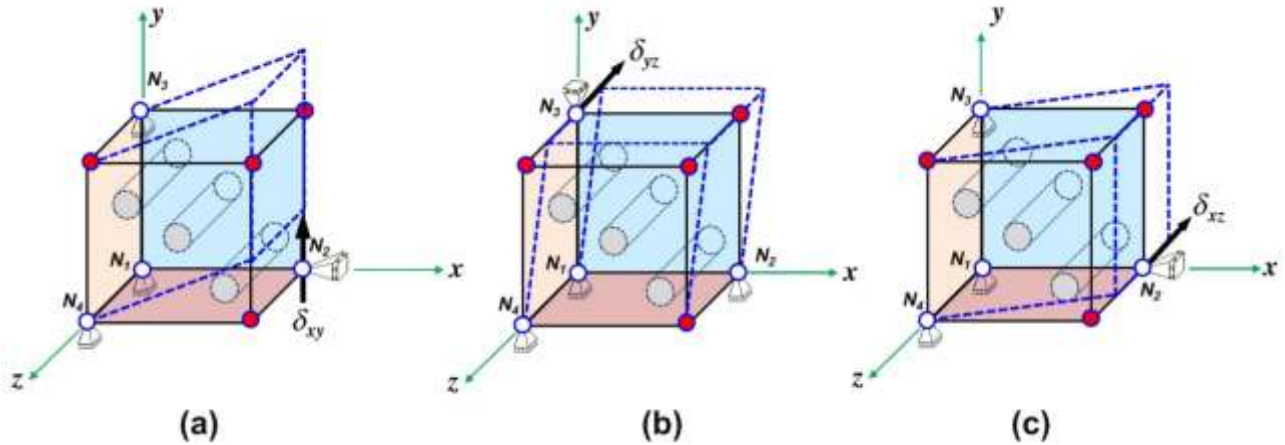


Figure 23: Shear loading applied to 3D RVE in a) XY , b) YZ and c) XZ plane, respectively [82].

2.4.3.1 Computational Homogenization in 3D

Let us consider a test composite within a macroscale domain (Ω_{MACRO}), as depicted in Fig. 24. Assuming statistical homogeneity in the material, we isolate a 3D microscale RVE within Ω_{RVE} , with L_{macro} and L_{RVE} denoting the macroscale and microscale length scales. We assume that Ω_{MACRO} length scale greatly exceeds Ω_{RVE} length scale, ensuring $\frac{L_{RVE}}{L_{macro}} \ll 1$ for any Ω_{RVE} chosen as a test composite RVE. Periodic boundary conditions are then applied to Ω_{RVE} (called

$\Omega_{PBC-RVE}$), equivalent to the 3D domain in Fig. 21. Computational homogenization is subsequently used to link the macro- and micro-fields.

Within the $\Omega_{PBC-RVE}$ domain, where a stress tensor σ is applied at a material point x within the enclosed volume V , the outward flux of stress through a specific surface, S_{np} , within the $\Omega_{PBC-RVE}$ can be expressed as the volume integral of the divergence within the region enclosed by that surface, given as:

$$\int_V \nabla \cdot (\sigma \times X) dV = \int_V [X \times \nabla \cdot \sigma + \nabla X^T \sigma] dV = \int_V \sigma dV \quad (22)$$

Eq. (22) holds when stress equilibrium is assumed, as $\nabla \cdot \sigma = 0$ (with no body forces) and $\nabla X^T = \nabla X = I$. Additionally, the outward normal, $n_{S_{np}}$, is defined as a vector always perpendicular to the surface, S_{np} . Using Gauss or divergence theorem, the integration over the volume in Eq. (22) can be related to the surface area (A) integral denoted as:

$$\int_V \sigma dV = \int_A (\sigma \times X) \cdot n_{S_{np}} dA = \int_A X \times t_{S_{np}} dA \quad (23)$$

Here, σ represents the symmetric stress tensor, where the surface traction is denoted as; $t_{S_{np}} = \sigma n_{S_{np}}$. Ultimately, the volume-averaged stress within the periodically deformed RVE domain, $\Omega_{PBC-RVE}$ (as illustrated in Fig. 24), can be expressed as:

$$\langle \sigma \rangle = \frac{1}{V} \int_V \sigma dV = \frac{1}{V} \int_A X \times t_{S_{np}} dA \quad (24)$$

Where the volume-averaged stress is denoted as $\langle \sigma \rangle$. This particular expression is applicable to a 3D RVE where nodal forces and displacement are applied at retained nodes, specifically N_1 , N_2 , N_3 , and N_4 .

Due to the periodicity constraints established within the $\Omega_{PBC-RVE}$ domain, all surface tractions cancel out during the volume-averaging process. This results in only the nodal forces applied to the retained nodes on that surface being considered. In other words, $t_{S_{np}} = 0$ for surface S_{np} , leaving us with the representation of the retained nodal forces as f_{N_i} , where $i = 1, 2, \dots, 4$. Here, X_i corresponds to the coordinate position of reference node N_i . Essentially, f_{N_i} represents the external forces applied at the retained nodes N_i .

$$\langle \sigma \rangle = \frac{1}{V} \int_V \sum_{i=1}^4 [X_i \times f_{N_i}] \quad (25)$$

Eq. (25) characterizes the volume-averaged stress within an RVE domain with periodic deformation, computed through the virtual work contributions arising from the presence of four retained nodal forces and the displacements of the 3D RVE domain.

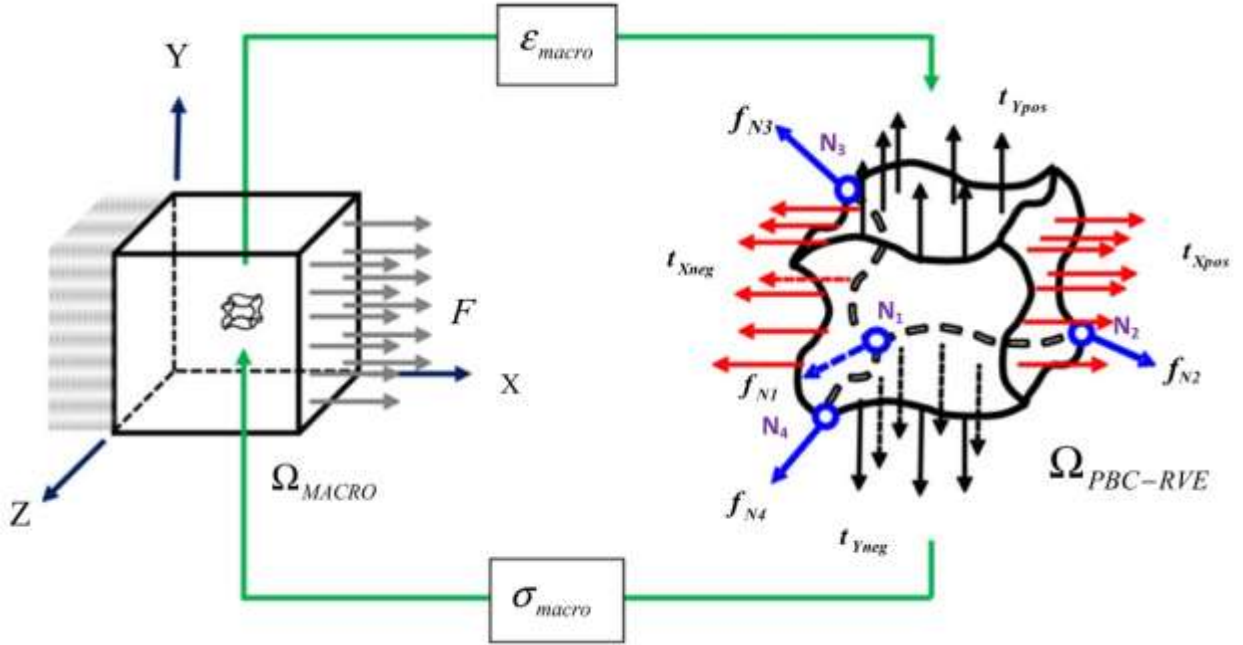


Figure 24: A schematic representation of macro- and micro-field relationship in 3D-RVE [82].

Under the assumption of global periodicity within the $\Omega_{PBC-RVE}$ domain, the overall macroscopic stress and the global strain are expressed as $\langle \sigma \rangle = \sigma_{macro}$ and ϵ_{macro} respectively. ϵ_{macro} is determined based on the displacements of the retained nodes, keeping in mind that u_1 is restricted to be zero to avoid rigid body motion. Consequently, the displacements of the remaining retained nodes are calculated as follows:

$$\begin{aligned}
 u_2 &= \epsilon_{macro}(X_2 - X_1), \\
 u_3 &= \epsilon_{macro}(X_3 - X_1), \\
 u_4 &= \epsilon_{macro}(X_4 - X_1)
 \end{aligned} \tag{26}$$

Here, u_i represents the displacement vector of retained node, i , in relation to its coordinate position, X_i , where $u_i = [u_{i,x}, u_{i,y}, u_{i,z}]$.

To comprehensively predict all possible effective elastic properties of the given test composite, displacement-controlled simulations were conducted by Okreke et.al. [82] as explained above. The effective properties were denoted as E_{ii}^{eff} being the effective Young's modulus along the i axis of the 3D RVE domain, ν_{ij}^{eff} representing the effective Poisson Ratio on an ij -plane, and G_{ij}^{eff} being the effective shear modulus on an ij -plane (for $i, j = 1, 2, 3$). Therefore, relying on volume-averaged stresses derived from microscale simulations, the following equations enable the determination of effective properties for the test composite:

For uniaxial deformation along X axis :

$$E_{11}^{eff} = \frac{\sigma_{11} (macro)}{\epsilon_{11} (macro)} , \quad \nu_{12}^{eff} = - \frac{\sigma_{22} (macro)}{\epsilon_{11} (macro)} , \quad \nu_{13}^{eff} = - \frac{\sigma_{33} (macro)}{\epsilon_{11} (macro)} \quad (27)$$

where, indices 1, 2 and 3 represent axes X, Y and Z respectively. Similarly, uniaxial deformation along Y and Z axes will result in following effective properties denoted in Eq. (28) and (29), respectively.

$$E_{22}^{eff} = \frac{\sigma_{22} (macro)}{\epsilon_{22} (macro)} , \quad \nu_{23}^{eff} = - \frac{\epsilon_{33} (macro)}{\epsilon_{22} (macro)} , \quad \nu_{21}^{eff} = - \frac{\epsilon_{11} (macro)}{\epsilon_{22} (macro)} \quad (28)$$

$$E_{33}^{eff} = \frac{\sigma_{33} (macro)}{\epsilon_{33} (macro)} , \quad \nu_{31}^{eff} = - \frac{\epsilon_{11} (macro)}{\epsilon_{33} (macro)} , \quad \nu_{32}^{eff} = - \frac{\epsilon_{22} (macro)}{\epsilon_{33} (macro)} \quad (29)$$

In the same fashion, the following are the effective shear moduli obtained from simple shear deformation along XY, XZ and YZ planes, respectively.

$$G_{12}^{eff} = \frac{\tau_{12} (macro)}{\gamma_{12} (macro)} , \quad G_{13}^{eff} = \frac{\tau_{13} (macro)}{\gamma_{13} (macro)} , \quad G_{23}^{eff} = \frac{\tau_{23} (macro)}{\gamma_{23} (macro)} \quad (30)$$

where, τ and γ are shear stress and shear strain, respectively.

2.5 Maxwell Equations

The Maxwell equations, originally formulated by James Clerk Maxwell in 1864, encapsulate the fundamental principles of electromagnetism, and are groundwork of our understanding of electromagnetism and the interactions between electric charges, currents, and magnetic fields. In the vacuum, all electromagnetic phenomena can be elucidated using a pair of field variables: one for the electric field and another for the magnetic field. Specifically, the electric field is denoted by the electric field intensity, often represented as E . In scenarios where the magnetic field originates from permanent magnets, it is typically described using the magnetic field intensity, referred to as H . Alternatively, when the field emanates from electric currents, it is represented by the magnetic induction, known as B . Finally, for scenarios involving the electric field between capacitors, an additional field variable known as the electric displacement, labeled as D , comes into play [86, 87]. In vacuum conditions, certain fundamental relationships hold as $B = \mu_0 H$ and $D = \epsilon_0 E$.

These equations involve two universal constants: μ_0 and ϵ_0 , vacuum permeability and permittivity, respectively. It's noteworthy that these constants are interconnected through the equation $\epsilon_0 \mu_0 = 1/c_0^2$, where c_0 denotes the speed of light in a vacuum. In Maxwell's original treatise, all four aforementioned field variables are employed, and the governing equations are as follows:

$$\begin{cases} \nabla \cdot \mathbf{B} = 0 \\ \nabla \times \mathbf{E} + \frac{\partial \mathbf{B}}{\partial t} = 0 \\ \nabla \cdot \mathbf{D} - \varphi = 0 \\ \nabla \times \mathbf{H} = \frac{\partial \mathbf{D}}{\partial t} + \mathbf{J} \end{cases} \quad (31)$$

In the above equations, φ represents the free charge density, and \mathbf{J} represents the free current density. The relationships between \mathbf{D} , \mathbf{J} , and \mathbf{H} with \mathbf{E} and \mathbf{B} , respectively, for linear isotropic materials are defined by the following constitutive equations:

$$\begin{cases} \mathbf{D} = \epsilon \mathbf{E} \\ \mathbf{B} = \mu \mathbf{H} \\ \mathbf{J} = Q \mathbf{E} \end{cases} \quad (32)$$

Here, ϵ is known as the dielectric constant, μ represents the magnetic permeability, and Q denotes the electric conductivity. The Maxwell equations, as represented by Eq. (31), are not standalone equations but are interconnected. By examining the three first sets of Eq. (31) we can derive the equation governing the conservation of charge:

$$\nabla \cdot \mathbf{J} + \partial \varphi / \partial t = 0 \quad (33)$$

When dealing with material media, two additional variables are introduced: the polarization density \mathbf{P} (representing the electric moment per unit volume) and the magnetization density \mathbf{M} (representing the magnetic moment per unit volume). These two variables relate to the other four as follows:

$$\begin{aligned} \mathbf{B} &\equiv \mu_0 (\mathbf{H} + \mathbf{M}) \\ \mathbf{D} &\equiv \epsilon_0 \mathbf{E} + \mathbf{P} \end{aligned} \quad (34)$$

Expressed in terms of \mathbf{E} , \mathbf{B} , \mathbf{P} , and \mathbf{M} , Maxwell equations in Eq. (31) can be rewritten as:

$$\begin{cases} \nabla \cdot \mathbf{B} = 0 \\ \nabla \times \mathbf{E} + \frac{\partial \mathbf{B}}{\partial t} = 0 \\ \epsilon_0 \nabla \cdot \mathbf{E} + \nabla \cdot \mathbf{P} - \varphi = 0 \\ \mu_0^{-1} \nabla \times \mathbf{B} - \epsilon_0 \frac{\partial \mathbf{E}}{\partial t} = \frac{\partial \mathbf{P}}{\partial t} + \nabla \times \mathbf{M} + \mathbf{J} \end{cases} \quad (35)$$

These equations, expressed in terms of \mathbf{E} , \mathbf{B} , \mathbf{P} , and \mathbf{M} , provide a comprehensive framework for understanding electromagnetic phenomena in both vacuum and material media [88].

2.6 Maxwell's Stress Tensor

Indeed, the force acting on a point charge q moving with velocity “ v ” in the presence of both an electric field E and a magnetic field B is described by the Lorentz force equation. This equation is a fundamental concept in electromagnetism and is expressed as [88]:

$$F = q(E + v \times B) \quad (36)$$

Likewise, the force exerted on a charge density φ within a volume V , expressed as the force per unit volume, f , can be represented as:

$$f = \varphi(E + v \times B) \quad (37)$$

Using Eq. (32), Eq. (37) could also be written in terms of current density, J :

$$f = \varphi E + J \times B \quad (38)$$

Eliminating φ and J by employing the last two sets of Maxwell's equations (Eq. 31), we have:

$$\begin{aligned} \varphi &= \epsilon_0 \nabla \cdot E \\ J &= \mu_0^{-1} \nabla \times B - \epsilon_0 \frac{\partial E}{\partial t} \end{aligned} \quad (39)$$

Substituting Eq. (39) in Eq. (38) yields:

$$f = \epsilon_0 (\nabla \cdot E) E + (\mu_0^{-1} \nabla \times B - \epsilon_0 \frac{\partial E}{\partial t}) \times B \quad (40)$$

Considering the relation:

$$\frac{\partial E}{\partial t} \times B = \frac{\partial(E \times B)}{\partial t} - \frac{\partial B}{\partial t} \times E \quad (41)$$

and faraday's induction law as:

$$\frac{\partial B}{\partial t} = -\nabla \times E \quad (42)$$

Eq. (40) can be cast into the following form:

$$f = \epsilon_0 [(\nabla \cdot E) E - E \times (\nabla \times E)] + [\mu_0^{-1} (\nabla \times B) \times B] - \epsilon_0 \frac{\partial(E \times B)}{\partial t} \quad (43)$$

To maintain symmetry, we can introduce an additional term $(\nabla \cdot \mathbf{B}) \mathbf{B}$. Importantly, because due to the Gauss law in magnetism $\nabla \cdot \mathbf{B} = 0$, this adjustment does not incur any alteration in the outcome, and follows as:

$$f = \epsilon_0 [(\nabla \cdot \mathbf{E})\mathbf{E} - \mathbf{E} \times (\nabla \times \mathbf{E})] + \mu_0^{-1} [(\nabla \cdot \mathbf{B})\mathbf{B} - \mathbf{B} \times (\nabla \times \mathbf{B})] - \epsilon_0 \frac{\partial(\mathbf{E} \times \mathbf{B})}{\partial t} \quad (44)$$

Considering the following equation from gradient properties in algebra for two arbitrary vectors \mathbf{X} and \mathbf{Y} :

$$\nabla(\mathbf{X} \cdot \mathbf{Y}) = \mathbf{X} \times \nabla \times \mathbf{Y} + \mathbf{Y} \times \nabla \times \mathbf{X} + (\mathbf{X} \cdot \nabla)\mathbf{Y} + (\mathbf{Y} \cdot \nabla)\mathbf{X} \quad (45)$$

And, taking into account that $\nabla(\mathbf{X}^2) = \nabla(\mathbf{X} \cdot \mathbf{X})$ and applying it to \mathbf{E} and \mathbf{B} using Eq. (45), we can rewrite Eq. (44) in the following form:

$$f = \epsilon_0 [(\nabla \cdot \mathbf{E})\mathbf{E} - (\mathbf{E} \cdot \nabla)\mathbf{E}] + \mu_0^{-1} [(\nabla \cdot \mathbf{B})\mathbf{B} - (\mathbf{B} \cdot \nabla)\mathbf{B}] - \left[\frac{1}{2} \epsilon_0 \nabla(\mathbf{E}^2) + \frac{1}{2\mu_0} \nabla(\mathbf{B}^2) \right] - \epsilon_0 \frac{\partial(\mathbf{E} \times \mathbf{B})}{\partial t} \quad (46)$$

Rewriting this equation in tensor form, we can introduce Maxwell Stress tensor as follows:

$$T_{ij} = \epsilon_0 (E_i E_j - \frac{1}{2} \delta_{ij} E^2) + \frac{1}{\mu_0} (B_i B_j - \frac{1}{2} \delta_{ij} B^2) \quad (47)$$

where, δ_{ij} is the Kronecker delta which is defined as:

$$\begin{cases} \delta_{ij} = 1 & ; i = j \\ \delta_{ij} = 0 & ; i \neq j \end{cases} \quad (48)$$

In the MRE materials, and specifically in this study, MREs are only exposed to uniform magnetic fields, so the first part of Eq. (47), containing the electric field, will be eliminated, leaving the Maxwell stress tensor to be reduced to:

$$T_{ij} = \frac{1}{\mu_0} (B_i B_j - \frac{1}{2} \delta_{ij} B^2) \quad (49)$$

2.7 Governing Equations

In this sub-section the constitutive equations in the context of continuum mechanics are discussed. By considering the basic balance principles of continuum mechanics, such as the linear momentum and angular momentum balance principles, there exists the equation of mechanical equilibrium as follows [87]:

$$\nabla \cdot \boldsymbol{\sigma} + \rho \mathbf{f} = \rho \dot{\mathbf{v}} \quad (50)$$

Here, σ represents the stress tensor, ρ is density, f represents the body forces, and v is the velocity. In the case of stationary or quasi static conditions ($\dot{v} = 0$), the force balance equation simplifies to:

$$\nabla \cdot \sigma + \rho f = 0 \quad (51)$$

When coupling magnetic and elastic behavior, different methods can be used to define body forces and stresses. The deformation of the material due to a magnetic field can be incorporated into the force balance equation in terms of the magnetic force per unit volume, denoted as f_m . Considering that the only other body force which is the weight is negligible, we have:

$$\nabla \cdot \sigma + \rho (f_m) = 0 \quad (52)$$

Alternatively, Eq. (52) can be expressed in terms of the total stress tensor \mathbf{T} :

$$\nabla \cdot \mathbf{T} = 0 ; \quad \mathbf{T} = \sigma + T \quad (53)$$

Here, T contributes to the sum of mechanical and magnetic stress tensors as $\mathbf{T} = \sigma + T$, where T follows as predefined Eq. (49).

2.8 Summary and Conclusion

This chapter, an extensive exploration of the Representative Volume Element (RVE) concept, particularly on determining their optimal dimensions to ensure projecting the structural characteristics of the entire macroscale structure was provided. Conducting a thorough investigation into various fundamental factors influencing the determination of RVE size, such as particle shape, size, and distribution, and considering the inherent structure of MREs with non-overlapping hard spherical particles dispersed within remarkably soft elastomeric matrices, the ideal RVE dimensions for these materials was evaluated to be a simple cube of the host elastomer, containing one magnetic inclusion.

In order to establish a coherent continuum that mirrors the mechanical behavior of the authentic heterogeneous material, a critical phase involves meticulously selecting microscopic boundary conditions. Thus, in this chapter diverse microscale boundary conditions were investigated to identify the most suitable for characterizing RVEs. Periodic Boundary Conditions (PBC) emerged as the most fitting choice. Subsequently, the study conducted an in-depth investigation into the fundamental physical and mathematical principles of PBC, particularly within the homogenization method, to determine the macroscale effective elastic properties in both 2D and 3D configurations. The homogenization methods to identify the effective elastic material properties were also comprehensively outlined, in both configurations.

Due to the fact that MREs operate under coupled magneto-mechanical loading conditions, this chapter further delved into a comprehensive examination of the fundamental magnetic equations integrated into this study, defining the Maxwell stress tensor. Ultimately, the governing equation to incorporate both mechanical and magnetic stress tensors was established.

Chapter 3: Characterization of Elastomeric Matrix and Magnetic Inclusion in MREs

As discussed in chapters 1 and 2, MREs comprise an elastomeric matrix interspersed with magnetic inclusions. Establishing the RVE for finite element (FE) modeling requires characterizing the material properties inherent in both phases. In this chapter, the experimental data concerning the elastic properties of the host elastomer and the magnetic behavior of the ferromagnetic particles are utilized to articulate and integrate their behaviors into the modeling process.

For the host elastomer, two different types of silicone rubber, represented as Ecoflex 30 and Ecoflex 50 are chosen. Identical rectangular molds are fabricated using a 3D-printer, in order to fabricate the silicone rubber samples. The platinum-based silicone rubbers Ecoflex 30 and Ecoflex 50 are prepared, poured into the molds and cured at room temperature. The cured samples, then, undergo pure tensile test and the force-displacement data is extracted. The study follows by a comprehensive investigation on the strain energy function and the Ogden hyper-elastic material model. The extracted force-displacement data is then used to characterize the optimum parameters in the Ogden material model, through the Least-Square (LS) minimization method.

As of the magnetic particles, Carbonyl Iron Particles (CIPs) are considered in this study. Hence, this chapter follows by identifying the magnetic behavior of CIPs, using the nonlinear B-H curve provided by the manufacturer, however, the data does not capture the magnetic saturation. Consequently, the B-H curve is extrapolated up to saturation. Furthermore, the mechanical properties of CIP, along with the magnetic properties of silicone rubber are also identified.

3.1 Silicone Rubber Tensile Test

3.1.1 Sample Fabrication

In order to generate the RVE for predicting the shear modulus of MRE, two data sets are required: the mechanical and magnetic properties of the pure rubber material (the matrix) and Carbonyl Iron Particle (CIP) (the ferromagnetic inclusions). As of the rubber material, silicone rubber was chosen and produced in the laboratory using two different types of silicone rubber, represented as Ecoflex 30 and Ecoflex 50. In order to fabricate identical samples in terms of shape and dimensions, two rectangular molds of $37 \times 6 \times 3$ [mm] were fabricated using a 3D-printer (Original Prusa i3 MK3S+), as shown in Fig.25.

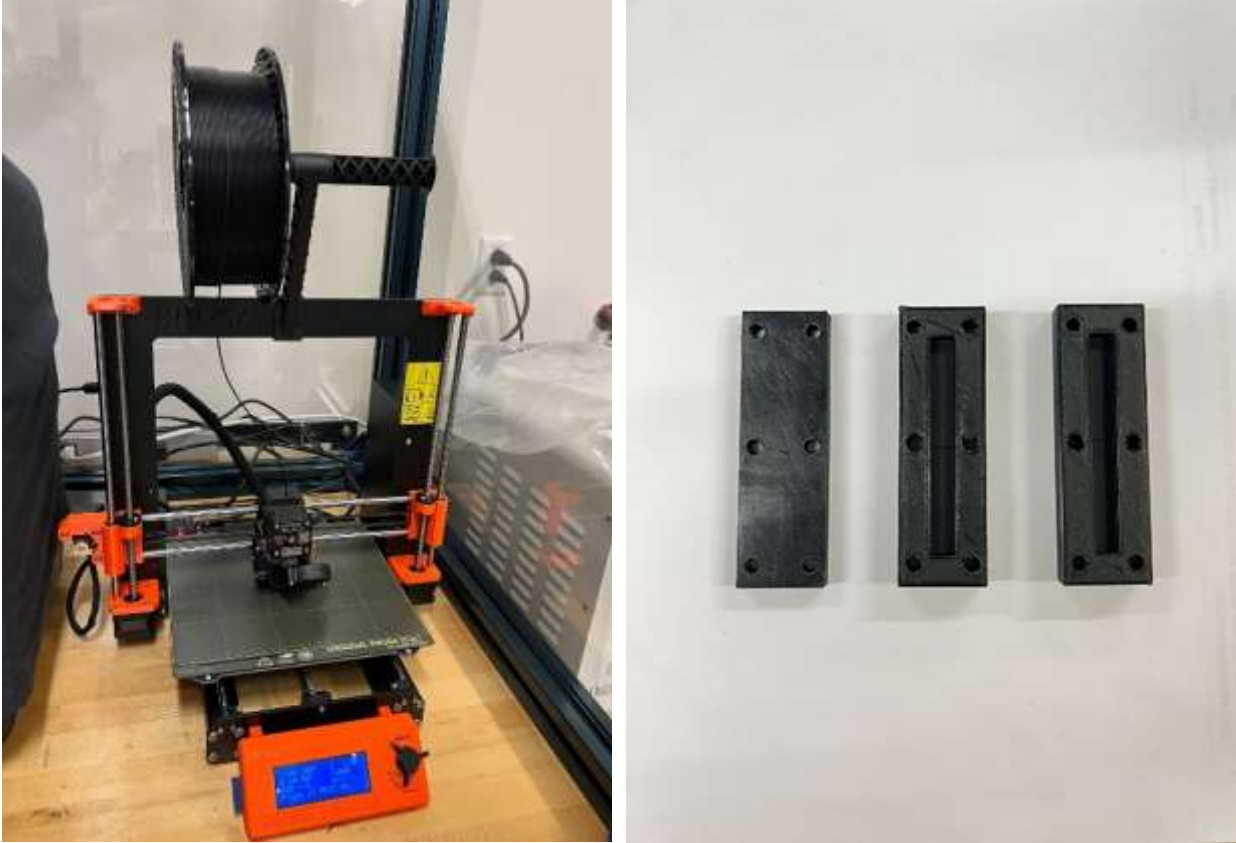


Figure 25: Fabricating the molds using a 3D-printer (Original Prusa i3 MK3S+) (left), and the fabricated molds (right).

To fabricate the silicone rubber samples, platinum-based silicone rubber from Smooth-on Inc. USA were used, comprising of two parts to be thoroughly mixed and cured. The two parts denoted as the rubber part (A) and the catalyst part (B), as shown in Fig 26.a, were added and stirred by 50-50 weight fraction. The primary mixture was then placed in the conditioning vacuum mixer (Thinky: ARV-200) for 40 seconds under 2000rpm to be thoroughly mixed and degassed. The final mixture was then poured into the molds and cured at room temperature for 15 hours (Fig. 26.b). Finally, the vulcanized samples were removed from the molds and were ready for the conducting the tensile test. Fig. 26.c shows the fabricated samples. The technical properties of silicone rubber Ecoflex 30 and Ecoflex 50 are provided in Appendix 1.

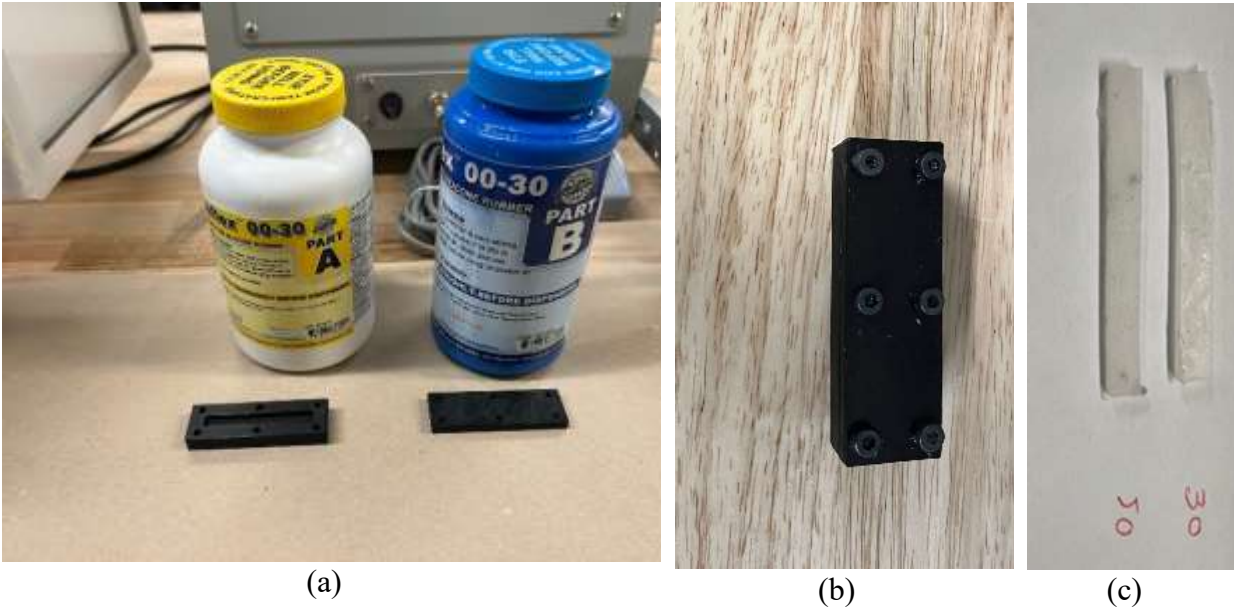


Figure 26: (a) Parts A and B for fabricating silicone rubber Ecoflex 30, (b) the pressed mold containing the mixture to be cured , and (c) the cured final samples (30 indicates EcoFlex 30 and 50 refers to EcoFlex 50).

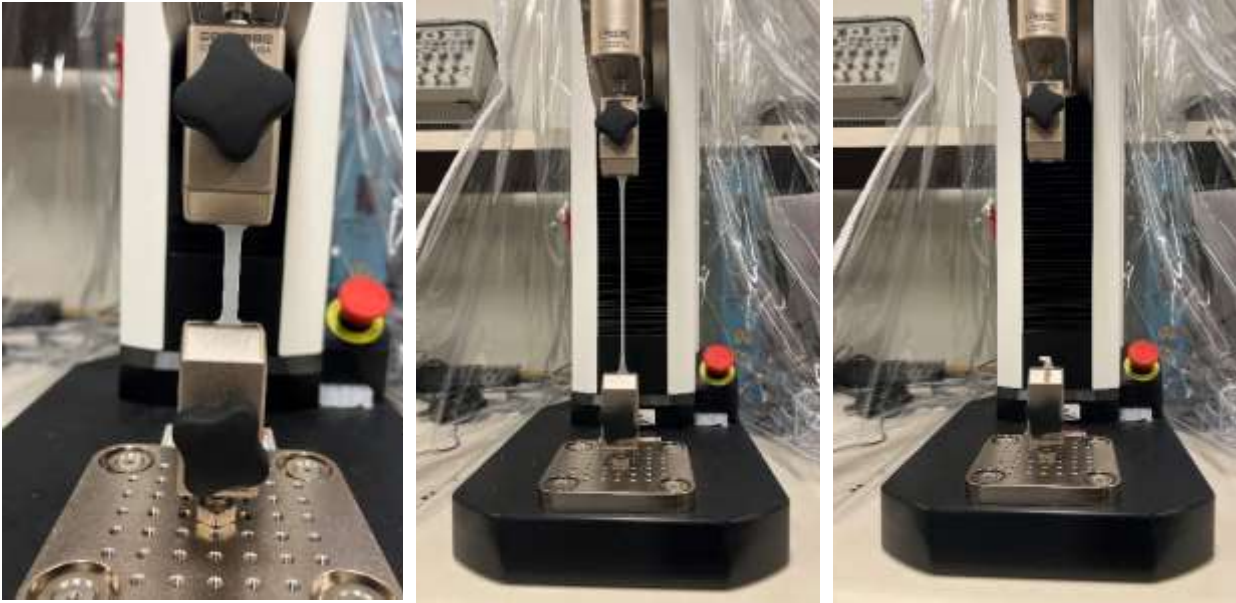
3.1.2 Characterization of the MRE's Elastomeric Matrix, using Uniaxial Tensile Test

In pursuit of determining the viscoelastic properties of silicone rubber samples, both samples underwent pure tensile to failure test, using an MTS machine (F1505-IM, Mark-10). Figs. 27 and 28 illustrate the three significant steps of the conducted test for silicone rubber EcoFlex 30 and Ecoflex 50, respectively.

The extracted force-displacement experimental data for silicone rubber EcoFlex 30 and EcoFlex 50 are shown and compared in Fig. 29. As it can be realized for the given force, silicone rubber EcoFlex 30 experiences larger displacement compared with EcoFlex 50 due to its lower stiffness. The force-displacement data were then used to obtain stress-stretch data which were subsequently utilized to identify the material parameters of hyper-elastic Ogden material model [89]. Compared with other hyperelastic models such as Neo-Hookean and Mooney-Rivlin, the Ogden model provides the best estimation.



(a) (b) (c)
Figure 27: (a) silicone rubber sample (Ecoflex 30) assembled on MTS machine prior to the tensile test, (b) sample through final steps of tensile test, and (c) the failed sample.



(a) (b) (c)
Figure 28: (a) silicone rubber sample (Ecoflex 50) assembled on MTS machine prior to the tensile test, (b) sample through final steps of tensile test, and (c) the failed sample.

3.2 Hyper-Elastic Strain Energy Function

In the theory of hyper-elasticity, the mechanical properties of materials are conveniently represented by the strain energy function, denoted as W , per unit volume. The strain energy function represents the stored energy in the material during the deformation. This function is dependent on the principal stretches (λ_1, λ_2 , and λ_3) characterized as follows [90, 91]:

$$x_1 = \lambda_1 X_1, \quad x_2 = \lambda_2 X_2, \quad x_3 = \lambda_3 X_3 \quad (54)$$

Rubber materials can be generally considered incompressible. Thus, the following constraint must be satisfied.

$$\lambda_1 \lambda_2 \lambda_3 = 1 \quad (55)$$

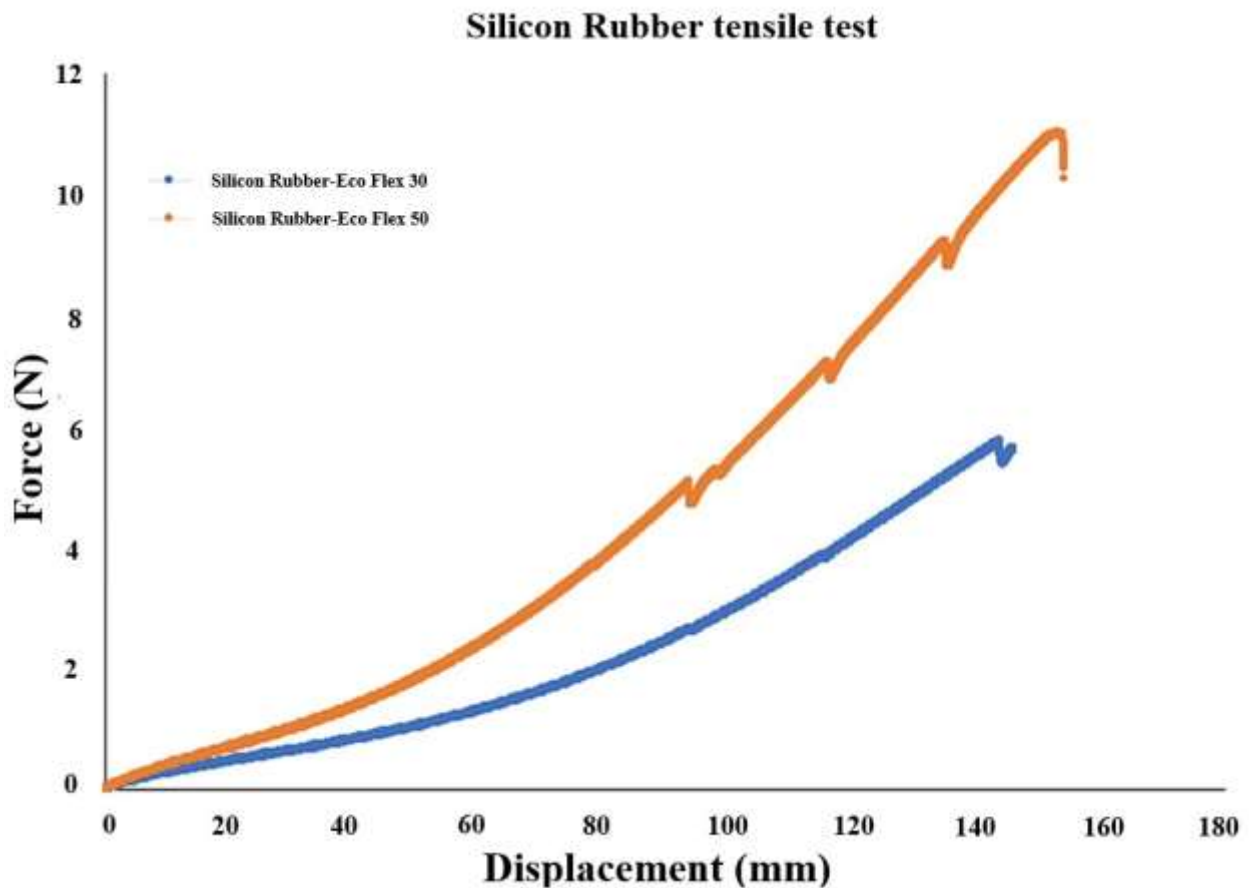


Figure 29: The extracted raw data of the conducted pure tensile to failure test, for silicone rubber-Ecoflex30 and Ecoflex50.

It is noted that principal stretches, λ_i , are stretch ratios (deformed length divided by the original length) for the unit fibers oriented along the principal directions. For the case of pure tension, the principal directions 1, 2 and 3 are aligned with three axes of Cartesian coordinate system, x (axis

of sample), y and z. Strain-energy function is essential for comparing theoretical and numerical models with experimental data in standard protocols. Let us first define the three invariants of Cauchy-Green strain tensor, using the aforementioned principal stretches as [90, 91]:

$$I_1 = \lambda_1^2 + \lambda_2^2 + \lambda_3^2, \quad I_2 = \lambda_1^{-2} + \lambda_2^{-2} + \lambda_3^{-2}, \quad I_3 = \lambda_1^2 \lambda_2^2 \lambda_3^2 = 1 \quad (56)$$

Considering the conducted experimental test, being pure tension, and based on Eq. (55), we have: $\lambda_1 = \lambda$ and $\lambda_2 = \lambda_3 = \lambda^{-\frac{1}{2}}$, and therefore the strain energy can be expressed as a function of the only independent stretch, λ . This could be represented as: $\bar{W}(\lambda) = W(I_1, I_2, I_3)$.

Moreover, the invariants in Eq. (56) reduce to the following form:

$$I_1 = \lambda^2 + 2/\lambda, \quad I_2 = 1/\lambda^2 + 2\lambda, \quad I_3 = 1 \quad (57)$$

The principal Cauchy stresses, denoted as σ_i ($i=1,2,3$), are intricately connected to the stretches through the derivative of the strain-energy function, as expressed by the following equations [92]:

$$\sigma_i = \lambda_i \frac{\partial W}{\partial \lambda_i} - L \quad (58)$$

Here, the index “ i ” does not represent a dummy index and there will be no summation over it, and L serves as an unknown Lagrange multiplier, associated with the constraint represented by Eq. (55). When examining pure tension scenarios, we have: $\sigma_2 = \sigma_3 = 0$, and hence:

$$(\sigma_1 - \sigma_2) = (\sigma_1 - \sigma_3) = \sigma_1 \quad (59)$$

Substituting Eq. (58) in Eq. (59), will effectively eliminate the unknown Lagrange multiplier L . Under uniaxial tension with stretch ratio given as $\lambda = l/l_0$ where l and l_0 are the deformed and unreformed length of the samples, respectively, and assuming incompressible materials ($\lambda_1 = \lambda$ and $\lambda_2 = \lambda_3 = \lambda^{-\frac{1}{2}}$), the relation for principal Cauchy stress along the tensile direction can be obtained as:

$$\sigma = \sigma_1 = \lambda \frac{\partial \bar{W}}{\partial \lambda} \equiv 2(\lambda - \lambda^{-2}) \left(\frac{\partial W}{\partial I_1} + \frac{1}{\lambda} \frac{\partial W}{\partial I_2} \right) \quad (60)$$

3.2.1 Ogden Hyper-Elastic Material Model

The Ogden strain energy function was proposed to describe the nonlinear behaviour of hyper-elastic materials. For incompressible materials, the strain energy function takes the following form [92]:

$$W = \sum_{p=1}^N \frac{\mu_p}{\alpha_p} (\lambda_1^{\alpha_p} + \lambda_2^{\alpha_p} + \lambda_3^{\alpha_p} - 3) \quad (61)$$

Here, each μ_p and α_p represents a material constant, to be determined. For practical application, the summation in Eq. (61) is confined to a finite number of terms. However, to maintain consistency with classical theory of incompressible isotropic elasticity, these constants must adhere to the condition:

$$\sum_{p=1}^N \mu_p \alpha_p = 2G \quad (62)$$

where, N is a positive integer, and G is the shear modulus of the material in its undeformed stress-free (natural) configuration, which implies that $\sum_{p=1}^N \mu_p \alpha_p > 0$.

In the present research study, the three term Ogden model ($N=3$) was adopted due to its better accuracy compared to one-term and two-term Ogden model [89]. Using the three term Ogden strain energy function in Eq. (61), and substituting it in Eq. (60), the principal value of the Cauchy stress can be obtained as:

$$\sigma = \sum_{p=1}^3 \mu_p (\lambda_i^{\alpha_p - 1} - \lambda_i^{-\frac{1}{2}\alpha_p + 1}) \quad (63)$$

3.3 Identification of Ogden Model Parameters

The extracted data from the pure tensile test was then employed to determine the material parameters in Ogden strain-energy function through least squares (LS) optimization technique. Let us consider a vector $\Lambda = [\Lambda_1, \Lambda_2, \dots, \Lambda_m]^T$, representing a collection of experimental deformation values, and associated vector $S = [S_1, S_2, \dots, S_m]^T$, corresponding to stress values, in which m represents the number of datasets.

For the given deformation vector Λ , using Ogden material model, the principal Cauchy stress in Eq. (63) can be expressed as $\sigma(\mu_p, \alpha_p)$, in which the material parameters μ_p and α_p are unknown. It is noted that, for the three term Ogden model $p=1$ to 3 and thus the number of unknown material parameters are 6 (i.e. $\mu_1, \mu_2, \mu_3, \alpha_1, \alpha_2, \alpha_3$). A least square minimization problem has been subsequently formulated to identify the material parameters in order to minimize the error between experiment and model results. The error function may thus be defined as:

$$E_r = \sum_{j=1}^m \left[1 - \frac{\sigma(\mu_p, \alpha_p)}{S_j} \right]^2 \quad (64)$$

Now, considering Eq. (63), the optimization problem can be formulated as:

Find the design variables: $\{\mu_1, \mu_2, \mu_3, \alpha_1, \alpha_2, \alpha_3\}$

To minimize E_r ;

$$E_r = \sum_{j=1}^m \left[1 - \frac{\sum_{p=1}^3 \mu_p (\lambda_j^{\alpha_p - 1} - \lambda_j^{-\frac{1}{2}(\alpha_p + 1)})}{S_j} \right]^2 \quad (65)$$

Subjected to: $\sum_{p=1}^3 (-\mu_p \alpha_p) < 0$

The optimization problem in Eq. (65) has been solved using stochastic based Genetic Algorithm (GA) and hybrid method based on the combination of GA and gradient based Sequential Quadratic Programming (SQP) method. The GA is known to provide near global optimum solution while SQP can accurately catch the local optimum solution close to the initial point. In the hybrid method, the optimal solution from GA has been fed into the SQP as the initial point in an attempt to accurately identify the global optimum solution.

The identified optimal Ogden material parameters using GA and GA+SQP for both Ecoflex 30 and Ecoflex 50 silicone rubbers, are provided in Table 1. Table 2, also provides the basic mechanical and magnetic properties of silicone rubber.

Table 1: The optimized parameters gained through curve fitting the experimental data with the Ogden strain energy function

Material	Optimization method	μ_1 (Pa)	α_1	μ_2 (Pa)	α_2	μ_3 (Pa)	α_3	G (kPa)
Silicone Rubber Ecoflex 50	GA	0.0849e ⁶	1.0000	0.0005e ⁶	5.5354	-0.0001e ⁶	-1.000	43.88385
	GA+ SQP	0.0001e ⁶	1.0000	0.0088e ⁶	3.4927	-0.0076e ⁶	-5.3724	35.833
Silicone Rubber Ecoflex 30	GA	-6.9874e ⁶	1.6760	5.2412e ⁶	1.5601	1.8713e ⁶	1.9162	25.84939
	GA+ SQP	4.3891e ⁶	1.4354	-4.3380e ⁶	1.4529	0.0163e ⁶	3.1195	24.14089

Table 2: Material properties of silicone rubber

Material	Material properties	Value
Silicone Rubber	Density ρ	920 (Kg/m ³)
	Poisson ratio ν	~0.5 (incompressible material)
	Magnetic Relative Permeability μ_r	2

Figs. 30 and 31, respectively, show the stress-stretch response of silicone rubber Ecoflex 30 and Ecoflex 50 samples extracted from experiments with those obtained using Ogden model based on optimal material parameters identified using GA and GA+SQP. Results clearly show that Ogden material model, with optimal material parameters identified using GA+SQP, provides reasonable agreement with the experimental data.

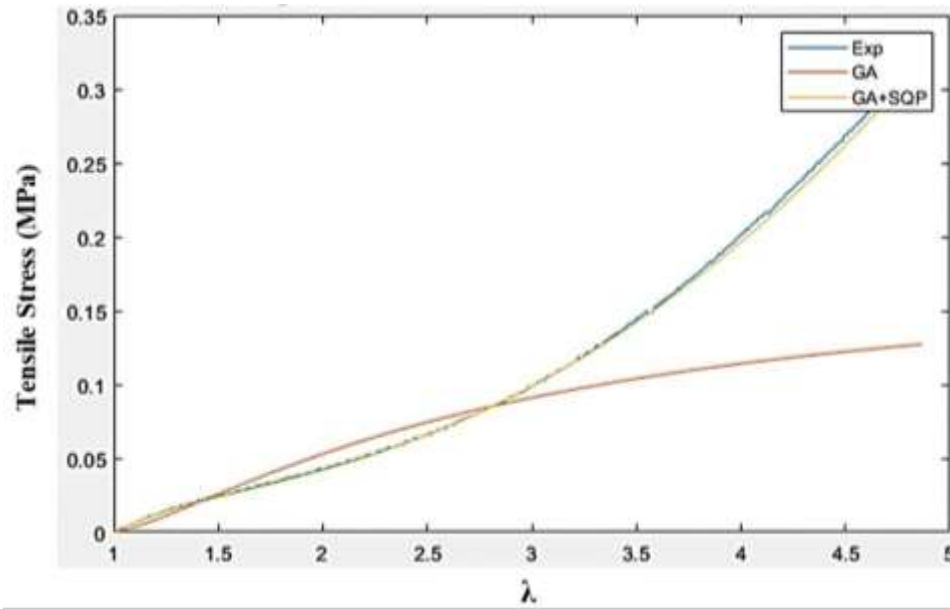


Figure 30: Curve-fitted plots for silicone rubber Ecoflex30 using least-square method, using GA and hybrid GA+SQP methods.

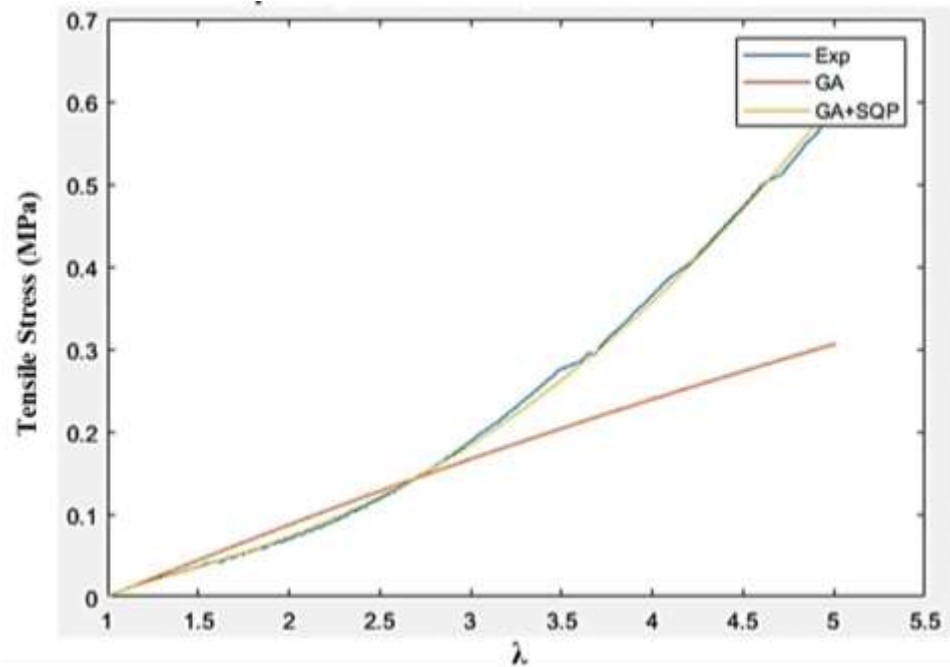


Figure 31: Curve-fitted plots for silicone rubber Ecoflex50 using least-square method, using GA and hybrid GA+SQP methods.

3.4 Magnetic Properties of Carbonyl Iron Particles

For the physic-based modeling of MREs, besides mechanical properties of elastomeric matrix, magnetic properties of micron-sized Carbonyl Iron Particles (CIP) should be accurately identified. The magnetic properties of CIPs, in the form of hysteresis B-H curve, were provided by the

manufacturer, Mekatronik Ilmenau, Germany, as depicted in Fig. 32. Using the experimental B-H data, the following equation can be effectively used to predict B-H response of CIPs up to saturation [93].

$$B(H) = B_s(1 - ae^{-bH}) + \mu_0 H \quad (66)$$

In which, B and H are magnetic flux density and magnetic field intensity, respectively. B_s is the magnetic flux density at saturation, a and b are unknown magnetic parameters and $\mu_0 = 4\pi \times 10^{-7} \left[\frac{N}{A^2}\right]$. Using Eq. (66), the following B-H curve shown in Fig.33 was interpolated and extrapolated for CIP, using the provided COMSOL Multiphysics plug-in.

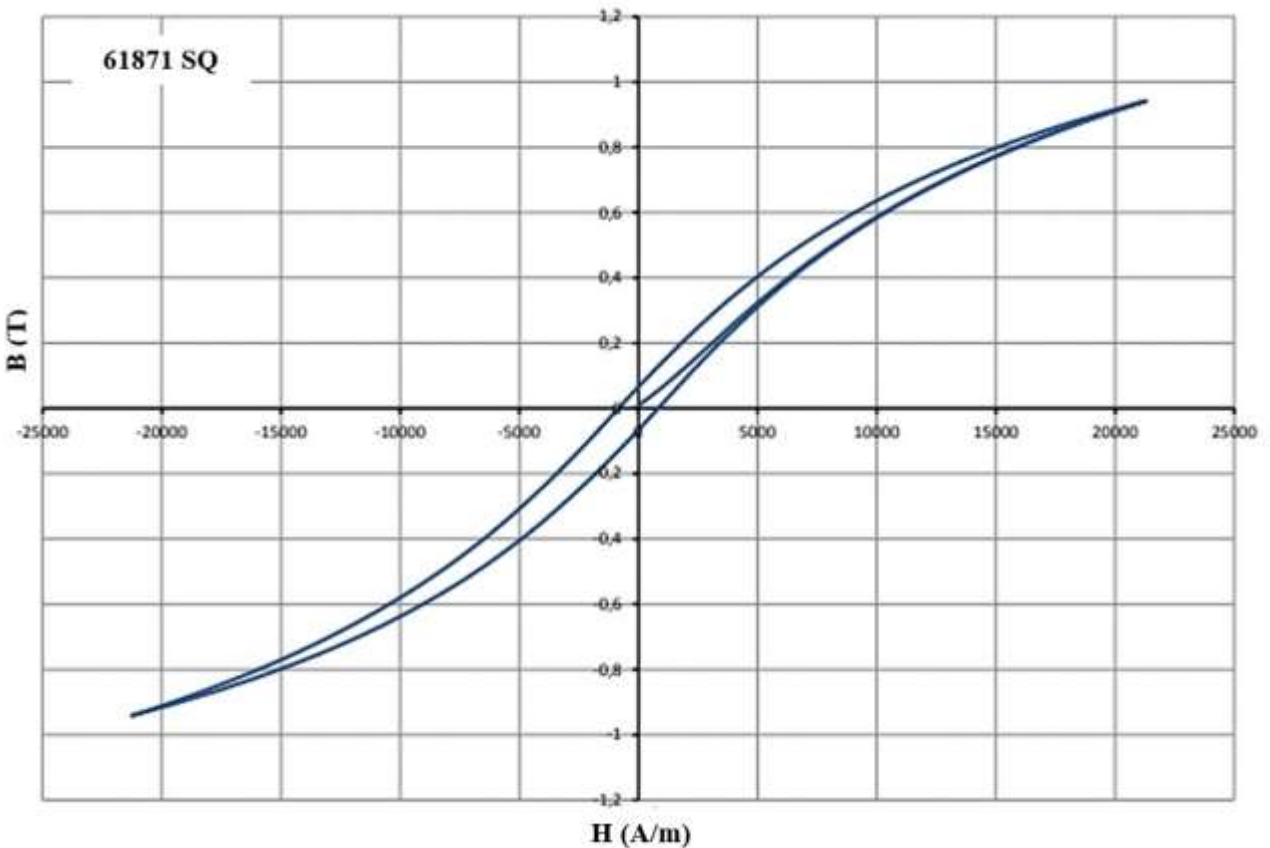


Figure 32: B-H curve for CIP provided by the manufacturer (Mekatronik Ilmenau, Germany).

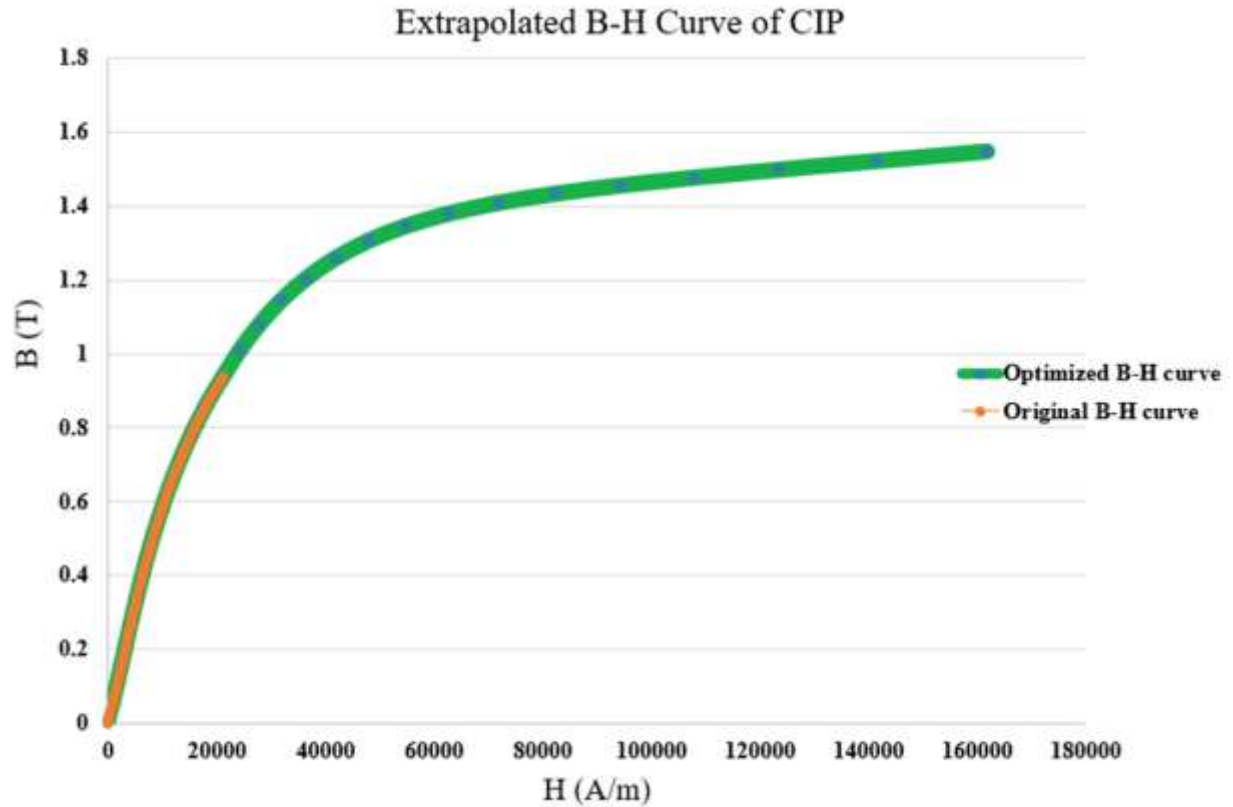


Figure 33: Extrapolated B-H curve of CIP. Vertical data represents Magnetic flux density (B) in Tesla and the Horizontal is the field intensity in A/m.

The identified material properties to be considered in the modeling, along with the optimized parameters for interpolation and extrapolation conducted on the B-H curve of CIP, using Eq. (66) are provided in Table 3.

Table 3: Material properties of air and CIP

Material	Material properties	Value
Air	Relative Permeability μ_r	1
CIP	Young's Modulus E	210 GPa
	Poisson ratio ν	0.33
	Density ρ	7870 Kg/m ³
Optimized Extrapolation Parameters for CIP B-H Curve	a	6.1746
	b	6.1943
	B_s	1.38 T

3.5 Summary and Conclusion

As comprehensively explored in chapter 1 and 2, MREs consist of an elastomeric matrix with magnetic inclusions dispersed in. For the purpose of the current study, an RVE should be generated for finite element (FE) analysis of MREs with silicone rubber as the host elastomer containing CIP as the ferromagnetic particles. This requires characterizing the material properties of both silicone rubber and CIP. This chapter conducted a detailed study on the experimental data concerning both silicone rubber and CIP, to be utilized to integrate their behaviors into the modeling process.

For the silicone rubber, two different platinum-based types, represented as Ecoflex 30 and Ecoflex 50 were chosen. In order to investigate their elastic behaviour, one sample of each was fabricated and underwent pure tensile test. It is noted that for the elastic behaviour of the silicone rubber samples to be comparable, two identical samples were fabricated, using two identical rectangular moulds manufactured using a 3D-printer. To fabricate the samples, silicone rubbers, consisting of two separate parts as the rubber part (A) and the catalyst part (B) were thoroughly mixed and vulcanized using a conditioning vacuum mixer. The prepared mixtures were then poured into the fabricated moulds and cured at room temperature for 15 hours. The cured samples, then, underwent pure tensile to failure test and the force-displacement data was extracted.

Among the strain energy functions proposed for predicting the hyper-elastic materials behavior, three term Ogden hyper-elastic material model was chosen due to its high accuracy compared with other models. The extracted force-displacement data was then used to characterize the optimum parameters in the Ogden material model, through the Least-Square (LS) minimization method. The optimization was conducted using stochastic based Genetic Algorithm (GA) and hybrid method based on the combination of GA and gradient based Sequential Quadratic Programming (SQP) method. The hybrid method provided a very high accuracy in predicting the nonlinear material behavior in both samples.

Subsequently, the magnetic behavior of CIPs was identified, using the nonlinear B-H curve provided by the manufacturer. The provided data set did not include the magnetic saturation. Consequently, the B-H curve was extrapolated up to saturation. Furthermore, the mechanical properties of CIP, along with the magnetic properties of silicone rubber were also identified.

Chapter 4: Finite Element Modeling of MRE, using Representative Volume Element (RVE)

In this Chapter, using the material properties for the matrix and inclusions, discussed in Chapter 3, 2D and 3D Representative Volume Elements (RVEs) have been developed for MREs, using Comsol Multiphysics (6.0). Following sections will investigate these two modeling fashions. It is worth mentioning that the simple cubic model which was previously verified in section 2.3 and proposed by Davis [40] and Jolly et. al. [48] was considered as the basis for modeling.

In this research study the focus is on isotropic MREs. In isotropic MREs, the magnetic particles are uniformly and randomly distributed with the host elastomeric matrix. In the subsequent sections, we initially delve into the modeling of MRE-RVE for isotropic MREs first in 2D configuration and then extend it to the 3D RVE configuration. The modeling in both configurations, concerns the pure shear deformation of MRE-RVEs under the application of external magnetic field. The modeling investigates the influence of varied magnetic flux densities, CIP content and the host rubber's hyper-elastic behavior on the shear modulus of the MREs. The MR effect behavior of the MRE-RVEs are also studied and compared.

4.1 Modeling the 2D MRE-RVE in Comsol

4.1.1 Isotropic MRE-RVE

The 2D MRE-RVE was generated in Comsol using a simple cube containing one CIP inclusion (Fig. 34). The mechanical and magnetic data associated with each part (matrix, inclusion and the surrounding air domain) were defined precisely, according to the previous chapter. In order to validate the model, the first modeling is done for silicone rubber Ecoflex50 with 15% volume fraction of CIP to compare with the experimental results from literature [55].

4.1.2 Meshing Pattern

A user-defined mesh approach has been employed to discretize the matrix, CIP, and the surrounding air. This methodology ensures precise control over meshing details, allowing for a finer mesh size in specific regions, such as boundaries, and coarsening where needed, especially within the air domain.

A mesh sensitivity analysis was performed to determine the most efficient number of elements, balancing computational cost with the attainment of reasonable results. Results for 2D MRE-RVE with 15% volume fraction of iron particles and exposed to magnetic flux density of 0.2T is provided for Ecoflex 50, in Fig. 35 as an example.

A relative error between the shear modulus obtained from the MRE-RVE modeling and the experimental results [55] is then defined as: $\frac{G_{MRE-RVE} - G_{Exp}}{G_{Exp}} \times 100$. As it can be realized, the decrease in the relative error is negligible for number of elements exceeding almost 3000.

Fig. 36 shows the FE model of the 2D MRE-RVE. As depicted in Fig. 36 (a) and as previously discussed, the mesh employed in the air domain gets coarser as it recedes the RVE boundaries. This is decided as the minimal mechanical or magnetic loading and displacements expected within this region. In contrary, the mesh is finely dispersed around the inclusion, using four boundary layers to ensure the necessary precision in that region. This is essential due to the concentrated interaction of magnetic and mechanical forces within this area. Fig. 36 (b) illustrates the boundary layers surrounding the inclusion. It is noteworthy that a total number of 3348 triangular elements were used to discretize the entire MRE-RVE including the surrounding air domain.

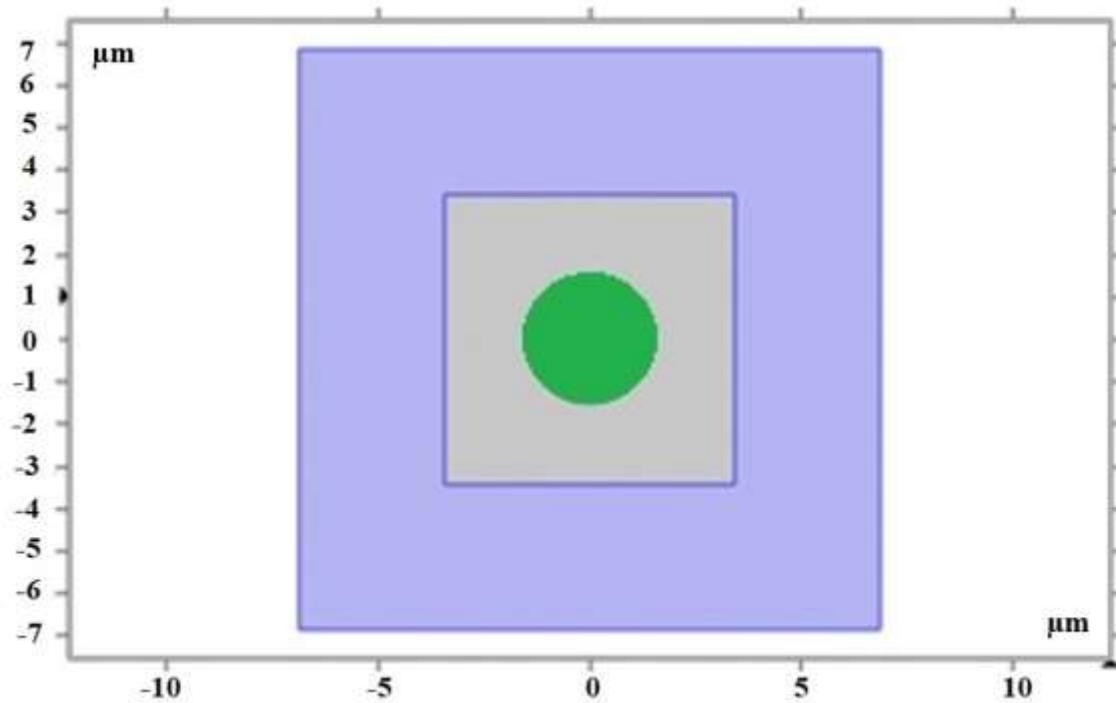


Figure 34: The 2D RVE generated in Comsol, Carbonyl Iron inclusion (Circle) inside the silicone rubber matrix (the gray square) surrounded by air domain (the purple square)

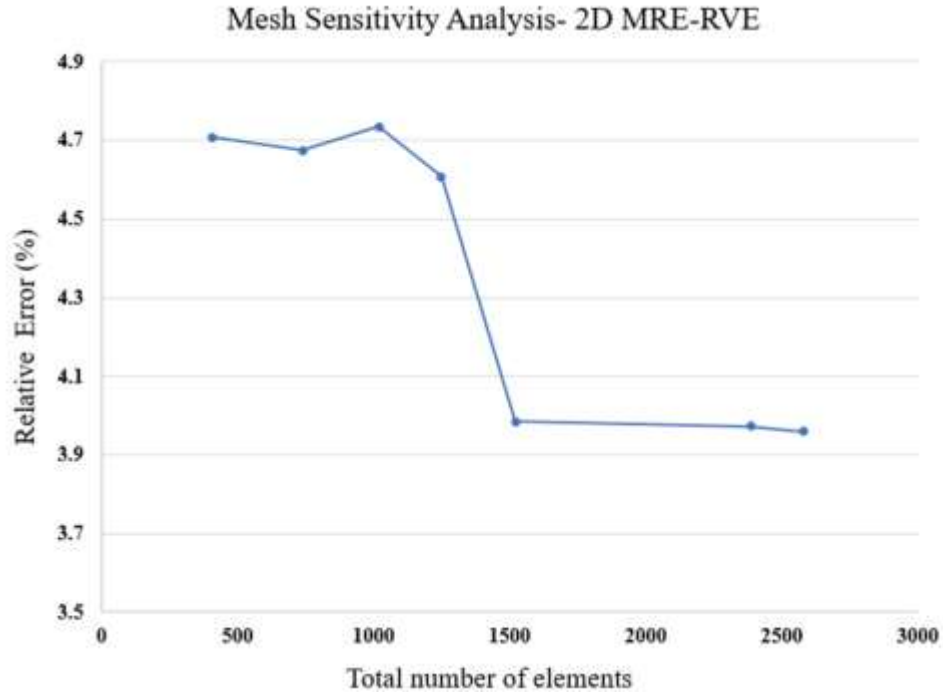


Figure 35: Mesh sensitivity analysis graph for 2D MRE-RVE model, Ecoflex 50 ($\phi=15\%$, $B= 0.2T$).

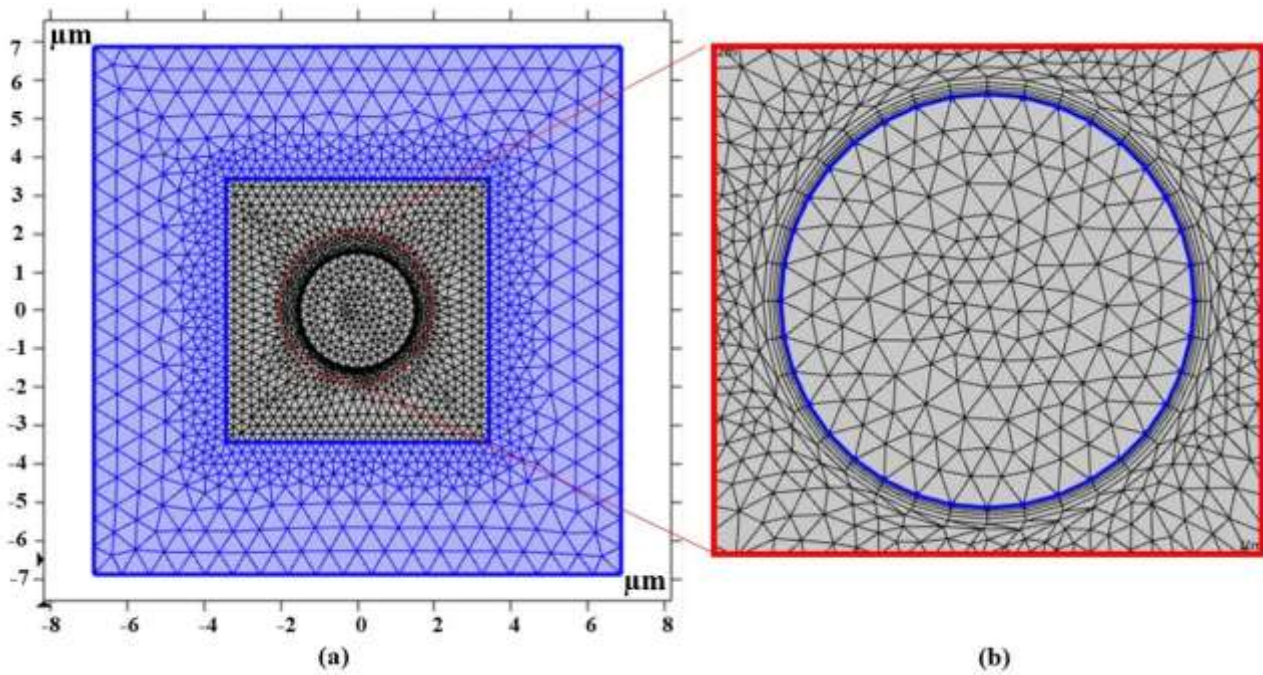


Figure 36: (a) The mesh pattern of MRE-RVE surrounded by the air domain (purple square), (b) The boundary layers implemented to enhance precision around the inclusion.

4.1.3 Shear Deformation of Isotropic MRE-RVE

Once the MRE-RVE is constructed, a shear deformation is incrementally applied on the top face of RVE up to 30% shear strain while the periodic boundary conditions are enforced on the edges. The shear deformation is conducted under magnetic field flux densities ranging from 0 to 0.7T applied perpendicular to the shear direction. Fig. 37 provides an illustration of the applied magnetic field on the RVE and the distortion of the magnetic field around CIP inclusion, as being absorbed by the inclusion. The induced uniform magnetic flux density inside the inclusion is also obvious in this figure. Moreover, Fig. 38 depicts the shear deformation of the RVE under the application of the magnetic field while periodic boundary conditions are applied on the RVE edges. It is noted that the results are provided for the silicone rubber Ecoflex50 MRE-RVE, with 15% volume fraction of CIP under the application of 0.4T magnetic flux density. In all figures, the smaller square indicates the RVE boundaries while the bigger one represents the air domain boundaries.

Maxwell stress tensor is applied on the inclusion boundaries and in combination with the mechanical stress, the total shear stress generated in the RVE is calculated. Fig. 39 presents the magnetic boundary loads on the CIP inclusion created by Maxwell stress under the application of magnetic field, and Fig. 40 shows the shear stress developed in the whole MRE-RVE.

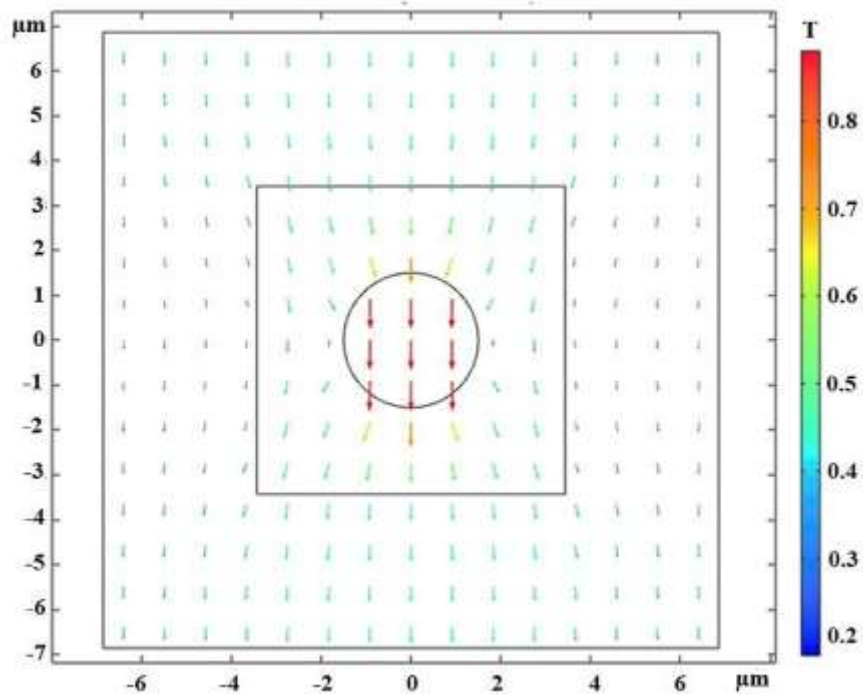


Figure 37: The magnetic field distortion around the CIP inclusion (the circle), while the small square indicates the RVE boundaries, and the big square is the air domain boundary. The color definition bar depicts the magnetic flux density in Tesla.

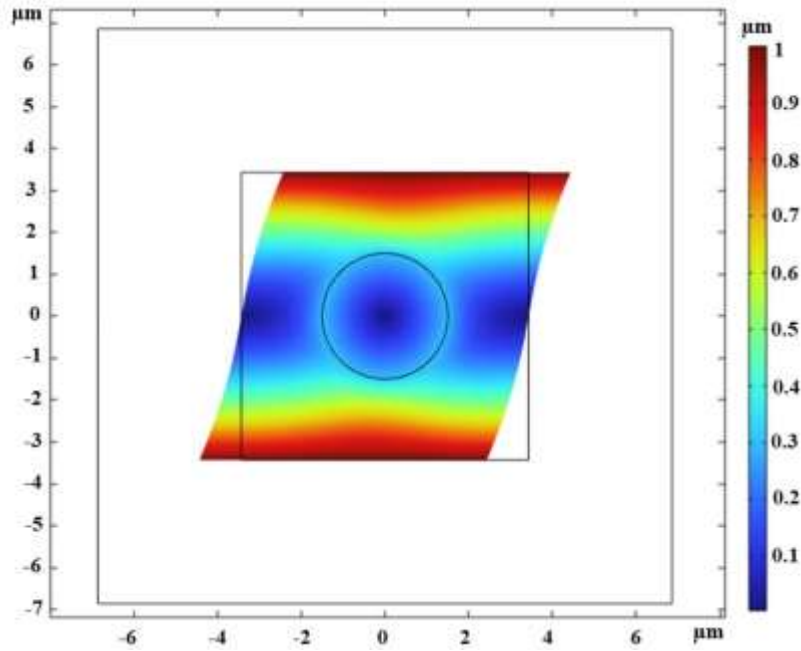


Figure 38: The shear deformation of MRE-RVE under 30% shear strain, while the periodic boundary conditions are being applied on the RVE boundaries. The color definition bar depicts the displacement magnitude in μm .

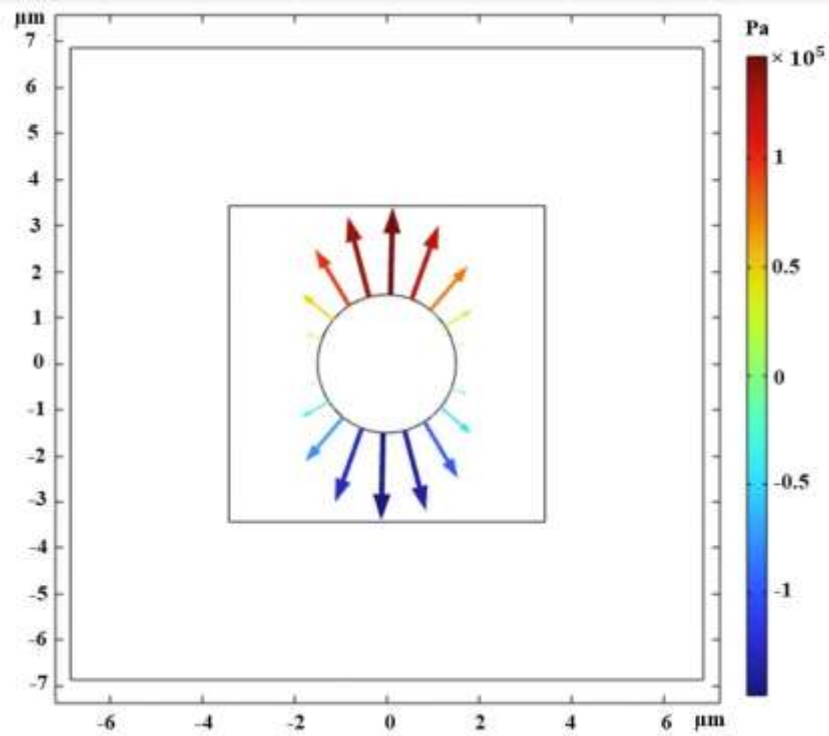


Figure 39: The magnetic boundary loads applied on the CIP inclusion boundaries. The color definition bar depicts the Maxwell upward stress tensor in Pa.

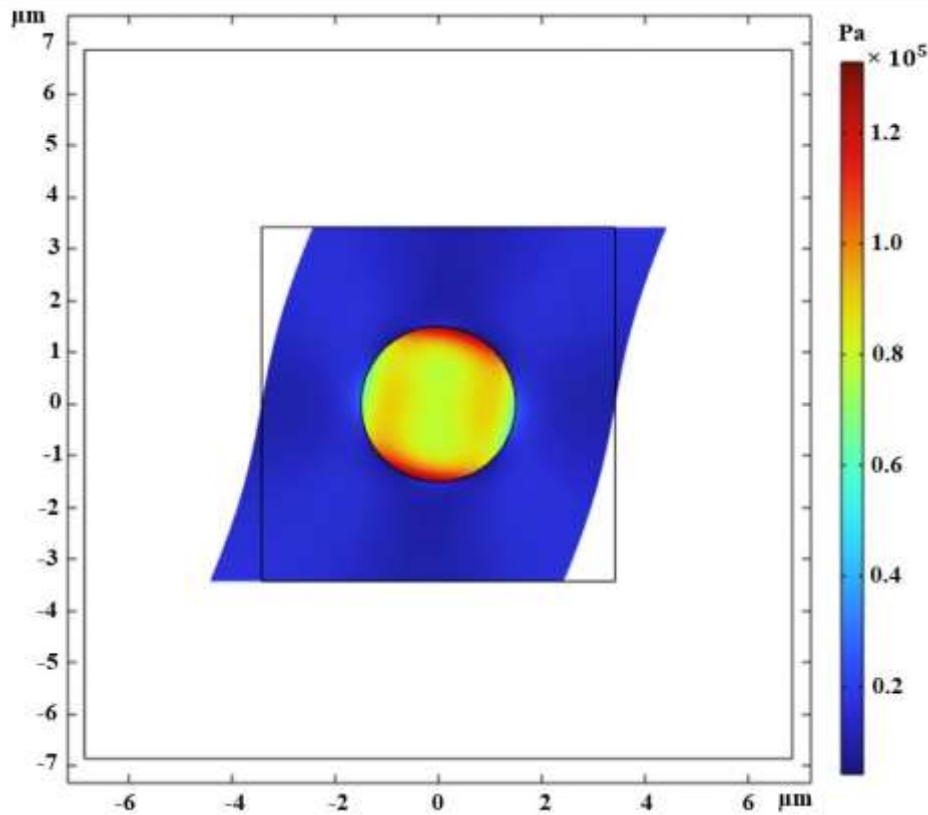


Figure 40: The whole shear stress (combination of magnetic and mechanical stress) in the RVE. The color definition bar depicts the stress magnitude in Pa.

Finally, the pure shear analysis was conducted to obtain stress stress-shear strain response of MRE-RVE under the application of different magnetic flux densities. Fig. 41 represents the homogenized shear stress versus shear strain of the silicone rubber Ecoflex 50 MRE-RVE containing 15% CIP in volume fraction under the application of magnetic flux densities ranging from 0 to 0.7T.

Examination of results in Fig. 41 reveals that shear modulus representing the slope of the shear stress-shear strain curves substantially increases by increasing the magnetic field intensity. This is evident from the increase in the shear stress developed for the given shear strain as the magnetic field strength increases. For instance, at nearly 30% shear strain, the generated shear stress increases almost 50% from nearly 20 kPa to almost over 30 kPa by increasing the magnetic flux density from 0 to 0.7T, respectively. The variation of the shear modulus with respect to the magnetic flux density using simulation based on 2D isotropic MRE-RVE and its comparison with the reported experimental results is shown in Fig. 42.

The zero-field shear modulus of MRE-RVE obtained from Comsol FE modeling is 59.9 kPa, which is 10% higher than the zero-field shear modulus of MRE given by experimental results, being 54.43 kPa. Moreover, Fig. 42 illustrates that the field-induced shear modulus of MRE-RVE reaches saturation at magnetic flux density of nearly 0.65T as also evident from Fig. 41, while that of experiment keeps increasing up to 0.8T of applied magnetic field.

The differences between modeling and experimental results are quantified in Table 4. Results show that while 2D isotropic MRE-RVE model may provide acceptable results for shear modulus results under lower magnetic field, it cannot capture the magneto-mechanical behaviour of MREs under higher magnetic field. For example, the differences between shear moduli from FE modeling and experiment are 10% at 0T, -11% at 0.4 T and -20% at 0.7 T.

This difference in the results could be attributed to the incapability of 2D model to capture the whole physical phenomenon. It is noted that in 2D RVE model, an extruded depth should be assigned to the plane geometry. Thus, the inclusion is in fact considered as a cylindrical short fiber which is different from the geometry of the nearly spherical inclusion in reality.

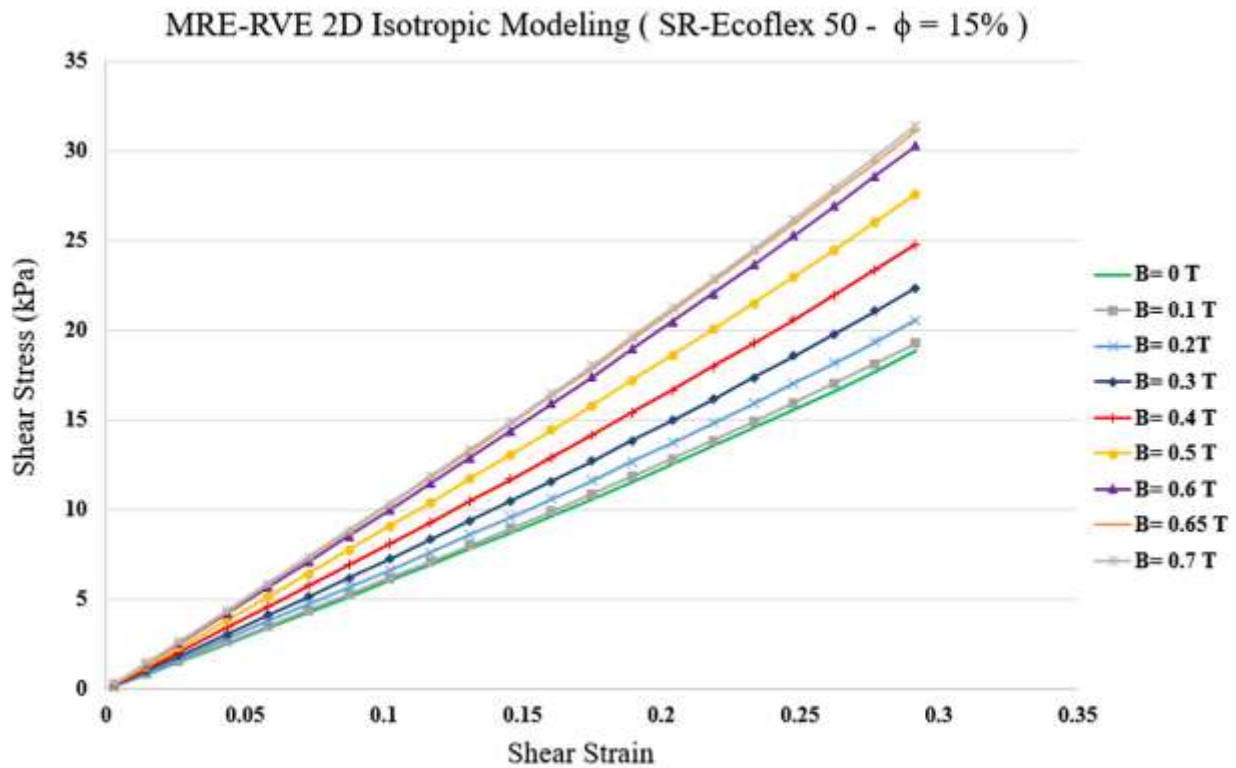


Figure 41: Shear stress- shear strain plot for 2D MRE-RVE under different applied magnetic fields.

Table 4: Comparing the results of 2D MRE-RVE and the Experiments.

	Zero-field shear modulus (kPa)	Maximum shear modulus (kPa)	Saturation magnetic flux density (T)	MR-Effect ($\Delta G/G_0$)
MRE-RVE	59.9	102.27	0.65	70.73%
Experiments [55]	54.43	146.59	0.8	169%

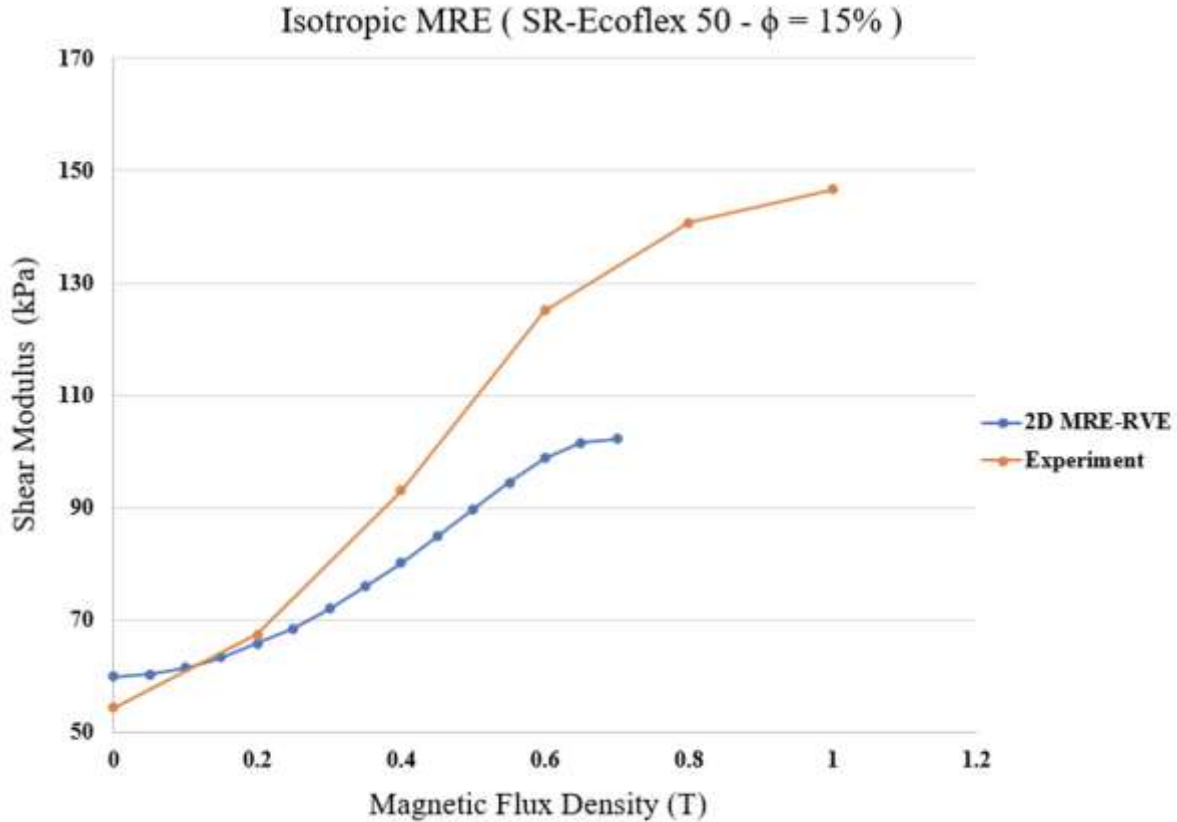


Figure 42: Comparison of shear modulus versus magnetic flux density obtained from Comsol FE modeling of 2D isotropic MRE-RVE with the experimental results [55] for silicone rubber Ecoflex 50-MRE with 15% VF of CIP.

The developed 2D isotropic MRE-RVE FE model was subsequently used to qualitatively investigate the effect of CIP volume fraction on the shear modulus. Figs. 43 (a - f) show the results for the shear stress-shear strain response behaviour of MREs under different magnetic flux densities for CIP volume fraction ranging from 5% to 40%. Results show that increasing the volume fraction of CIP, results in higher field-induced shear modulus. For instance, under shear strain of 30%, the shear stress increases from nearly 16 kPa to almost 23 kPa and from 35 kPa to 65 kPa for CIP volume fraction of 5% and 40%, respectively by increasing the magnetic flux density from 0 to 0.7T.

As the CIP volume fraction increases, the gap between two subsequent curves in each figure (a – f) increases, implying that the influence of magnetic field on shear modulus, and consequently, the MR effect increases as the volume fraction increases. The variation of MR effect with respect to CIP volume fraction is also shown in Fig. 44. Results suggest that the MR effect increases by increasing the CIP volume fraction. Although the MR effect is supposed to reach a maximum at around $\phi=27\%$ and then drop, the 2D modeling is not able to capture this behaviour and the MR effect keeps increasing as the volume fraction goes up.

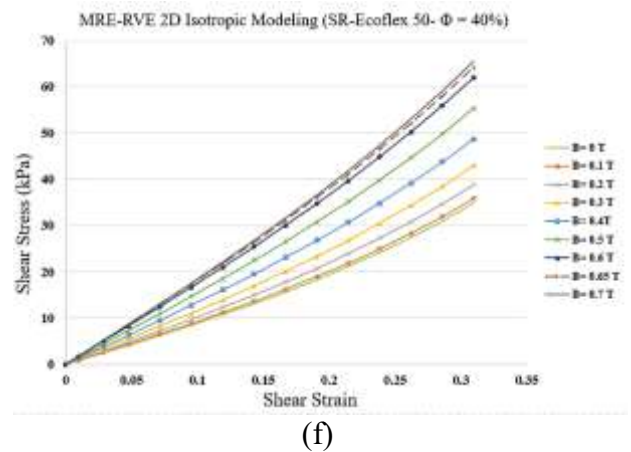
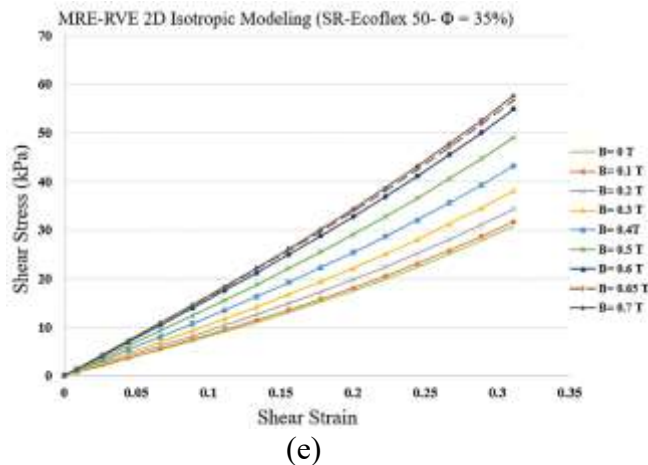
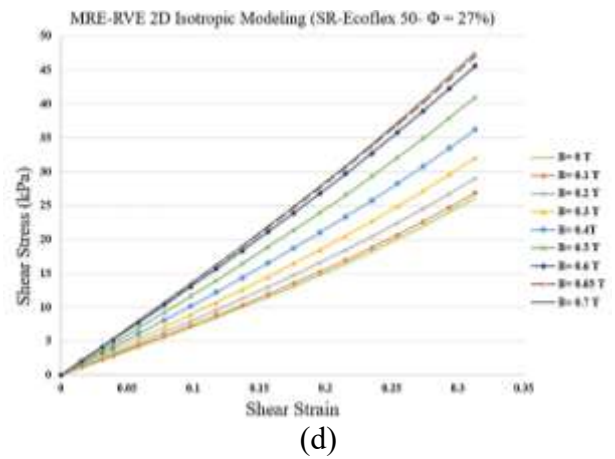
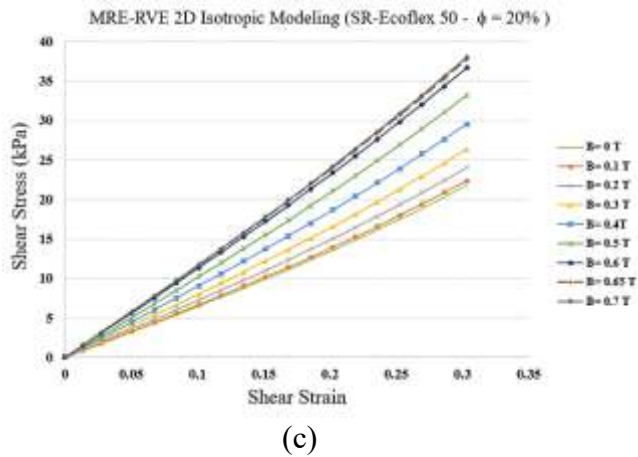
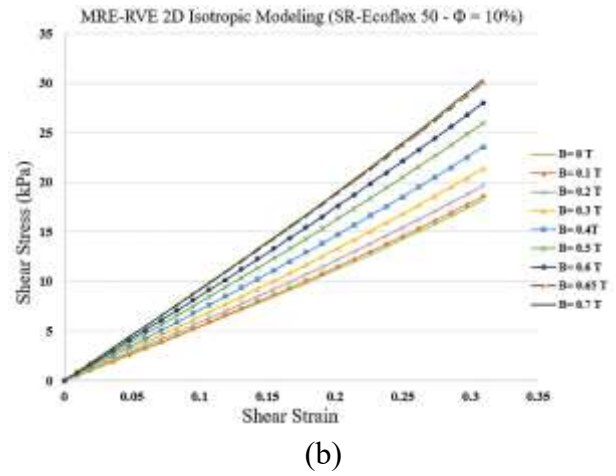
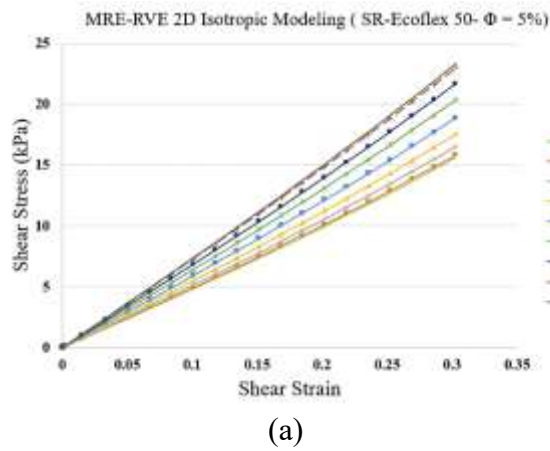


Figure 43: Shear stress- shear strain plot for 2D MRE-RVE under different applied magnetic fields for silicone rubber Ecoflex 50 with (a) 5%, (b) 10%, (c) 20%, (d) 27%, (e) 35%, and (f) 40% of CIP in volume fraction.

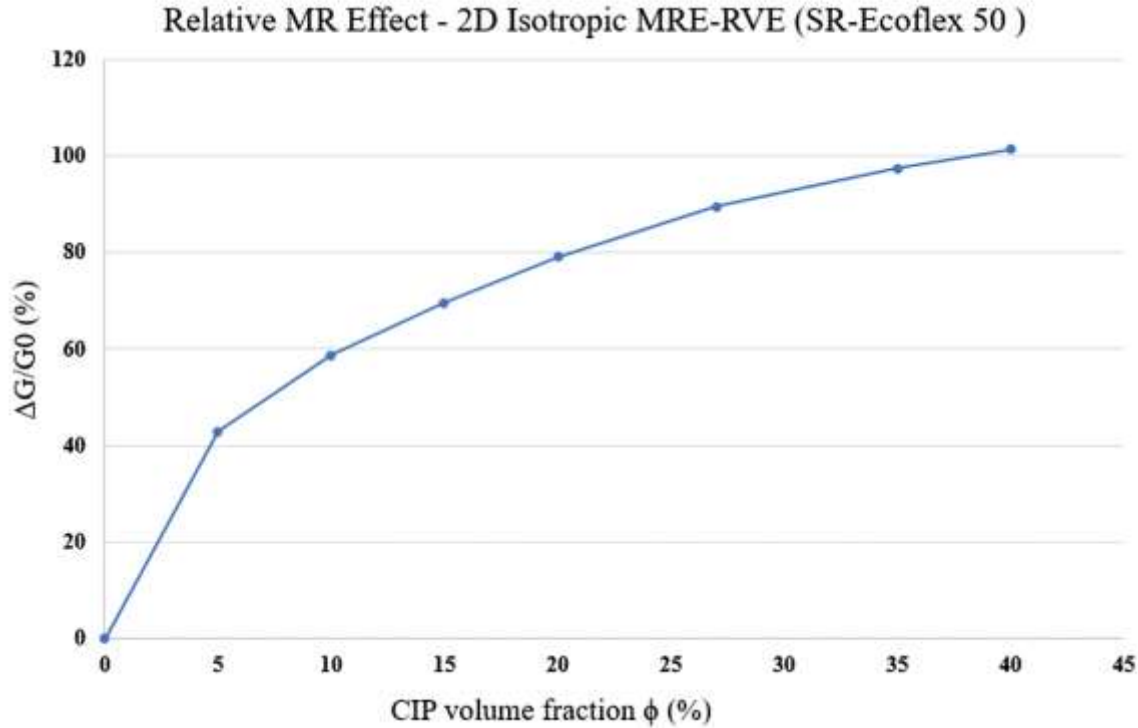


Figure 44: MR effect behaviour in 2D modeling of silicone rubber (SR) Ecoflex50 MRE-RVE with respect to CIP volume fraction.

The same procedure of FE modeling used for silicone rubber Ecoflex50 MRE-RVE, was conducted on silicone rubber Ecoflex30 MRE-RVE. The influence of different magnetic flux densities, ranging from 0- 0.7T, was also studied on the shear stress-shear strain response of the silicone rubber Ecoflex 30 MRE-RVEs, containing various CIP content. Then, a comparison was conducted on the results obtained for the two MRE-RVEs with different matrix materials (Ecoflex 30 and Ecoflex 50).

Fig. 45, presents the variation of shear moduli of the two MRE-RVEs, containing 15% CIP in volume fraction, with respect to the applied magnetic field. As shown in Fig. 45, in both MRE-RVEs, increasing the magnetic flux density results in obtaining a higher shear modulus, however, due to the lower zero-field shear modulus in the MRE with softer matrix material (Ecoflex 30) the relative increase in shear modulus in this MRE-RVE is more pronounced by applying the same magnetic flux density. For instance, the shear modulus in MRE-RVE with Ecoflex 30 reaches from roughly 40 kPa to around 80 kPa at 0.7T, indicating a 100% increase, while the shear modulus in MRE-RVE with Ecoflex 50 experiences a 70% increase, from 60 kPa at 0T to 102 kPa at 0.7T.

Fig. 46 is provided to further investigate the influence of magnetic flux density on the MR effect of the MRE-RVEs. As shown in Fig. 46 the relative MR effect in the MRE-RVE with softer matrix (Ecoflex 30) reaches a maximum of 154%, while the Ecoflex 50 MRE-RVE peaks at 100%, both containing 40% CIP in volume fraction. Although showing a higher relative MR effect in MREs with softer matrix is anticipated due to the experimental data in the literature [31, 55], the relative

MR effect is supposed to reach a peak at the optimum CIP volume fraction, and then decrease as the volume fraction goes up, which the 2D MRE-RVE modeling cannot capture this behaviour.

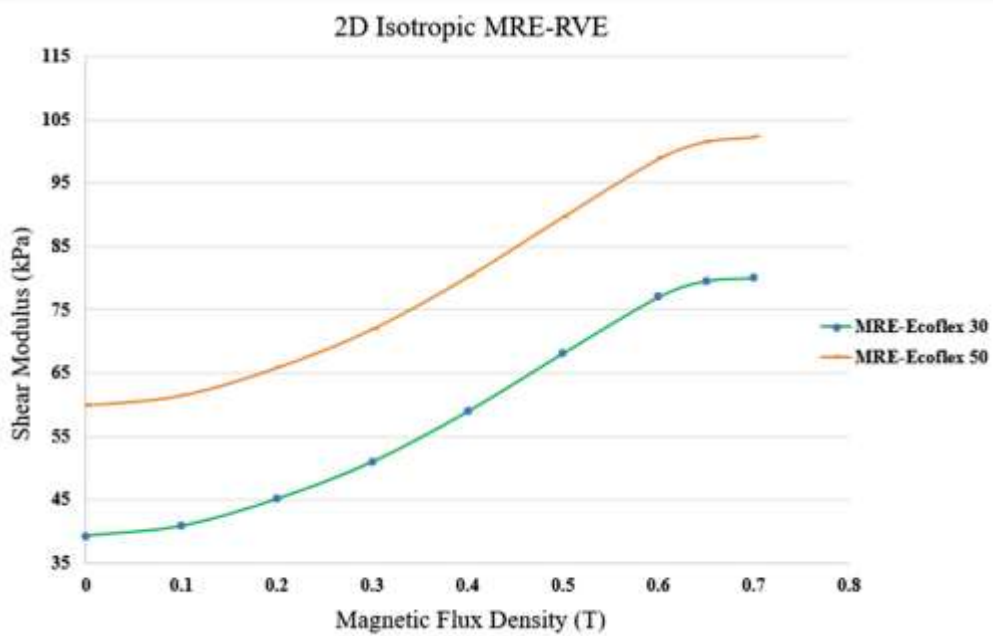


Figure 45: Comparison of shear modulus variation with respect to the applied magnetic flux density, for 2D MRE-RVEs with silicone rubber Ecoflex 30 and Ecoflex 50 as the matrix material.

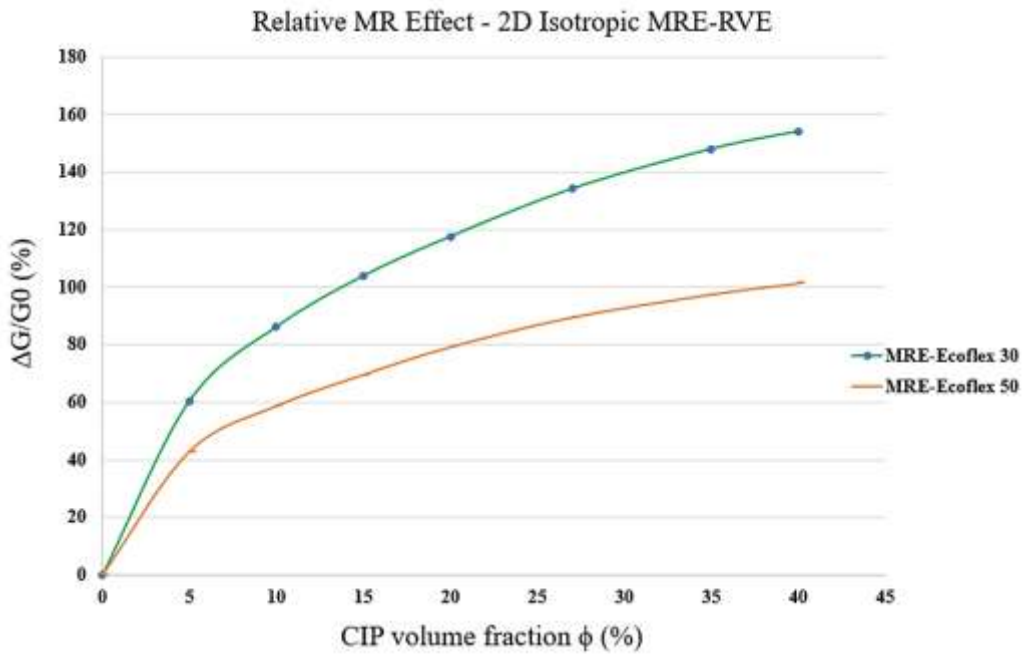


Figure 46: Comparison of the MR effect behaviour in 2D isotropic MRE-RVEs with different matrix materials (Ecoflex 50 and Ecoflex 30), with respect to CIP volume fraction.

4.2 Modeling the 3D MRE-RVE in Comsol

4.2.1 Isotropic MRE-RVE

As investigated in the previous section, 2D MRE-RVE was not able to properly capture the coupled magneto-mechanical response of MREs to predict the field-dependent shear modulus, as shown in Fig. 42. In this section, the approach has been extended to 3D. Different common RVE arrangements were modeled using silicone rubber Ecoflex 50, as the matrix material, containing 15% CIP in volume fraction. Fig. 47 illustrates the considered various RVE arrangements.

The shear deformation analysis similar to that for 2D RVE was conducted on different MRE-RVE arrangements shown in Fig. 47, while no magnetic field was applied. Comparing the obtained results with the results in the experiments [55], confirmed that the simple cubic RVE with one inclusion in the center provides the best agreement with the experimental results, while being simple and less computationally expensive. The zero-field shear modulus given by this RVE arrangement has a negligible 1.3% difference with the experimental results, while other arrangements lead to a higher difference in shear modulus, as detailed in Table 5. Thus, the further FE analyses were conducted on the simple cubic (SC) RVE arrangement.

The 3D MRE-RVE was generated in Comsol in the same fashion as that of 2D modeling. One CIP inclusion is generated and placed inside a simple cube of matrix material and surrounded by a larger cube of air, as shown in Fig. 48. The mechanical and magnetic data associated with each part (matrix, magnetic particles inclusion and the surrounding air domain) were also defined precisely, as explained before.

To validate the model, we initiated the modeling process with silicone rubber Ecoflex50 containing 15% volume fraction of CIP. Subsequently, we conducted a comparison with the experimental data reported in the literature [55].

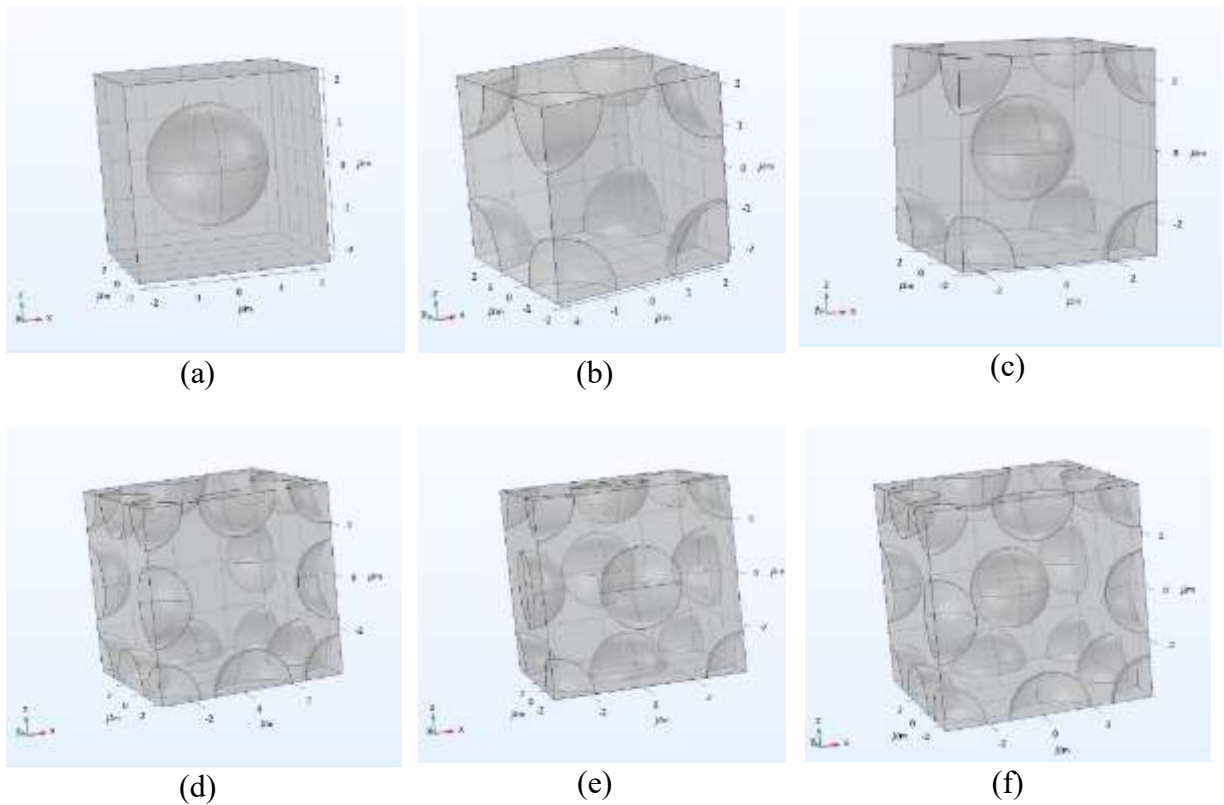


Figure 47: Different RVE arrangements (a) Simple Cubic (SC)-Davis (b) Simple Cubic (SC) (c) Body-Centered Cubic (BCC) (d) Face-Centered Cubic (FCC) (e) End-Centered Cubic (ECC) (f) Body- and End-Centered Cubic (BECC)

Table 5: Comparison of the initial shear moduli of different MRE-RVE arrangements with experimental data (No field applied) for MREs (silicone rubber Ecoflex50- $\Phi = 15\%$).

RVE Arrangement	SC-Davis	SC	BCC	FCC	ECC	BECC
Zero-Field Shear Modulus (kPa)	55.15	62.11	62.86	61.34	58.78	58.82
Difference with Experiments [55] (54.43 kPa)	1.3%	14%	15.5%	12.7%	7.9%	8%

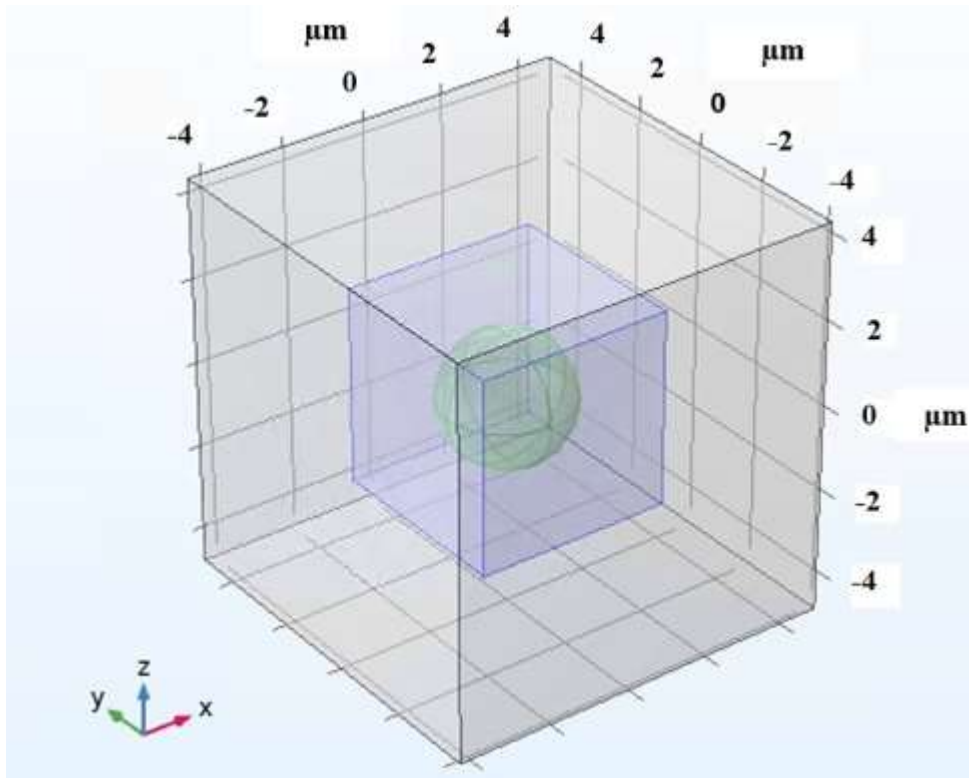


Figure 48: The 3D RVE generated in Comsol, Carbonyl Iron inclusion (the sphere) inside the silicone rubber matrix (the purple cube), surrounded by air domain (the gray cube).

4.2.2 Meshing Pattern

In order to create a complex and customized structure, the RVE underwent a detailed meshing procedure. We decided to utilize the "user-defined mesh" method, similar to the approach used in the 2D configuration. This decision grants us the capability to have comprehensive control over mesh intricacies. It allows for a finer element size and distribution in areas that demand precision, while employing coarser elements in regions where complex displacement or loading is not expected. A tetrahedron mesh type is used, as it provides more flexibility for meshing the curved boundaries, here, the spherical magnetic particle.

A methodical mesh sensitivity analysis was then systematically performed to reach the optimal mesh pattern, ensuring that computational resources were not needlessly burdened. Results in relative error between the shear modulus obtained from the 3D MRE-RVE modeling and the experimental results [55], defined as: $\frac{G_{MRE-RVE} - G_{exp}}{G_{exp}} \times 100$, for different number of elements are provided in Fig. 49. Just as described in the 2D modeling section, we explored various meshing configurations while creating the 3D model. Results in Fig. 49 shows that the relative error

between the shear modulus obtained from 3D MRE-RVE and experiments decreases as the total number of tetrahedron elements increases, indicating the convergence of the shear modulus.

Hence, based on this finding and evaluating the computational cost, we opted for the mesh configuration consisting of 30492 tetrahedral elements to balance between the computational cost and accuracy.

A visual representation of the mesh pattern applied in the 3D MRE-RVE modeling is provided in Fig. 50 (a). As previously explained, the mesh density in the air domain progressively coarsens as it moves away from the RVE boundaries, for the anticipation of minimal mechanical or magnetic loading and displacements in this particular zone. Conversely, the mesh is finely adjusted in the vicinity of the inclusion, to ensure the required precision in that area due to the intensified interaction of magnetic and mechanical forces. Fig. 50 (b) further illustrates the mesh quality in all regions.

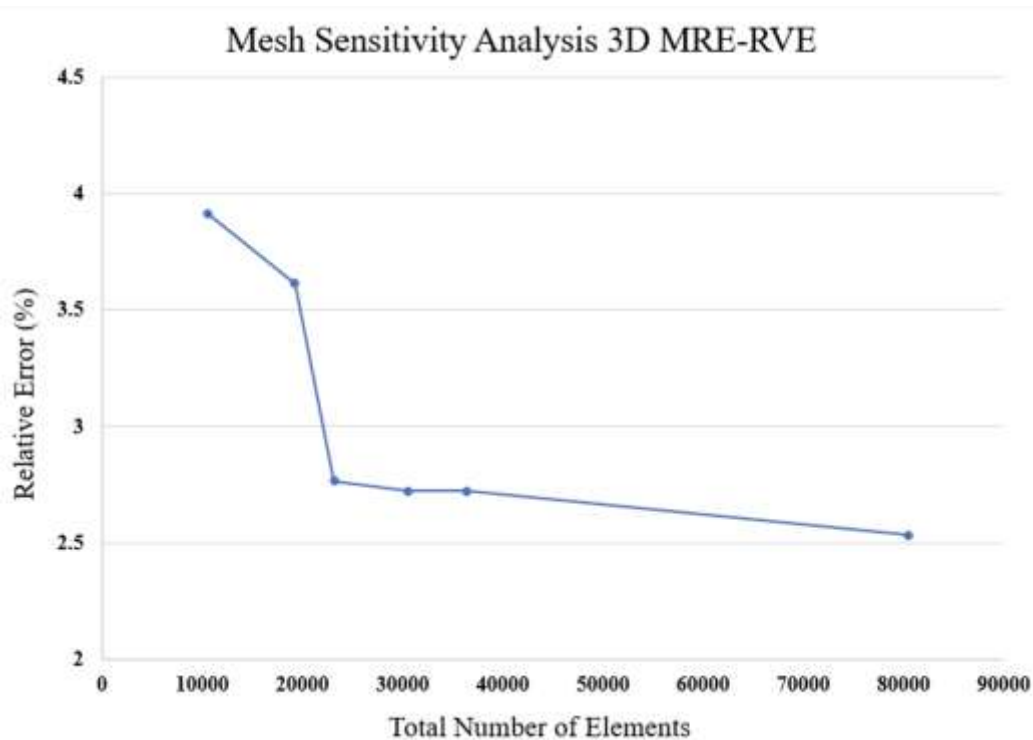


Figure 49: Mesh sensitivity analysis graph for 3D MRE-RVE model, ($\phi=15\%$, $B= 0.1T$) using different meshing schemes.

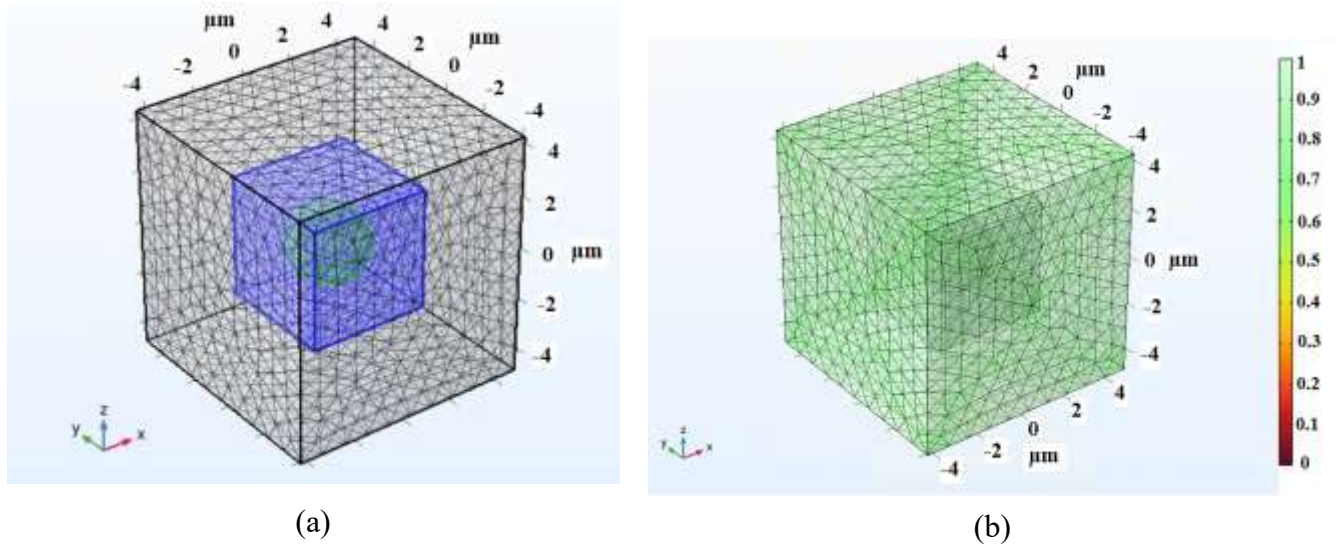


Figure 50: (a) The mesh pattern of MRE-RVE surrounded by the air domain, (b) The mesh quality in all regions with the color bar representing the quality of mesh in scale of 0 to 1.

4.2.3 Shear Deformation of Isotropic MRE-RVE

In the following, first the 3D-RVE model has been developed for MRE with Ecoflex 50 as the elastomeric matrix for comparison with available experimental data in the literature [55]. The effect of changing the matrix material to Ecoflex 30 on the shear response of MRE was subsequently investigated.

4.2.3.1 Silicone Rubber Ecoflex 50 MRE-RVE

As of shear analysis, we systematically subjected the RVE to incremental pure shear deformation, gradually reaching a shear strain of 30%. To maintain consistency, we imposed periodic boundary conditions along all surface boundaries. Concurrently, a magnetic field was applied perpendicular to the shear direction, spanning a range of magnitudes from 0 to 0.4T.

The visual representation in Fig. 51 clearly portrays the magnetic field's interaction with the RVE, particularly highlighting the distortion of the field as it encounters the CIP inclusion. This inclusion acts as a focal point for absorbing the magnetic field, with the high induced magnetic flux density within the inclusion clearly visible.

The Maxwell stress tensor was applied on the boundaries of the inclusion, and by integrating this with the mechanical stress, the overall shear stress generated within the 3D MRE-RVE was determined. Fig.52 illustrates the magnetic boundary loads exerted on the CIP inclusion due to Maxwell stress, when a magnetic field of 0.1T is applied.

Fig.53 illustrates a visualization of the shear deformation of the MRE-RVE under shear strain of 30%, and the shear stress distribution throughout the entire MRE-RVE. The RVE boundaries are

consistently depicted by the smaller cube, while the larger cube delineates the boundaries of the air domain. It's worth noting that all figures in this section feature the silicone rubber Ecoflex50 MRE_RVE with a 15% volume fraction of CIP, subjected to a magnetic field intensity of 0.1T.

Finally, the pure shear analysis was conducted on the MRE-RVE under the application of different magnetic field ranging 0- 0.4T. Results for the homogenized shear stress versus shear strain of the silicone rubber Ecoflex 50 MRE-RVE containing 15% CIP in volume fraction under the application of varied magnetic flux densities are shown in Fig. 54.

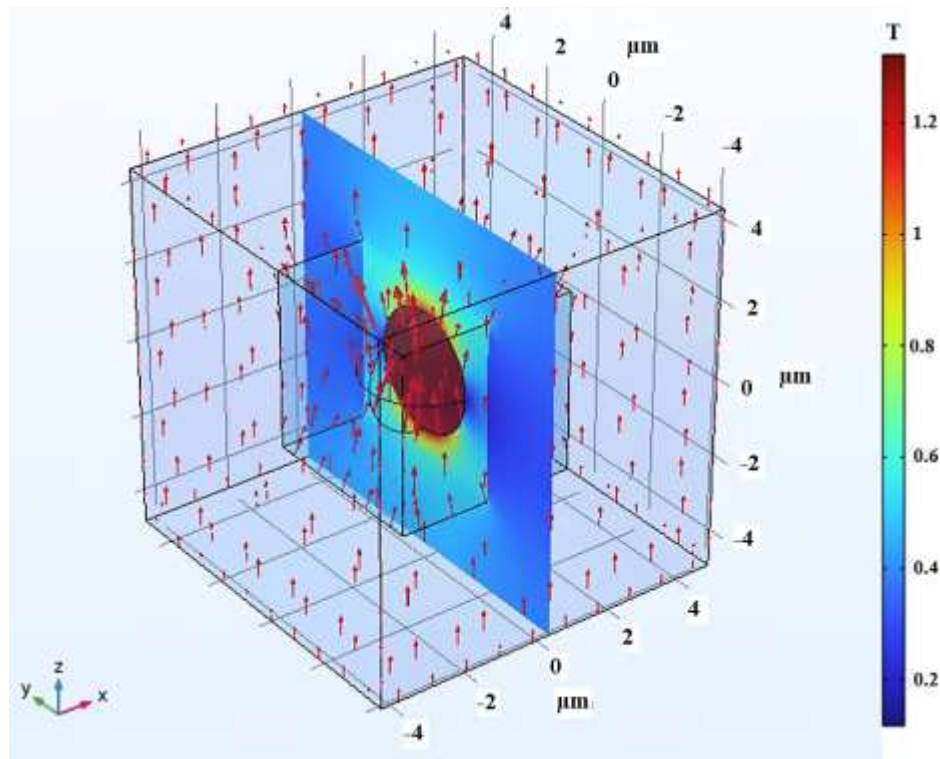


Figure 51: The magnetic field distortion around the CIP inclusion inside the 3D RVE, red arrows represent the magnetic field intensity and direction (0.1 T, upward), the color definition bar describes the magnetic flux density (T) in the air and MRE-RVE domain referring to the hypothetical cut out surface in the middle of the model.

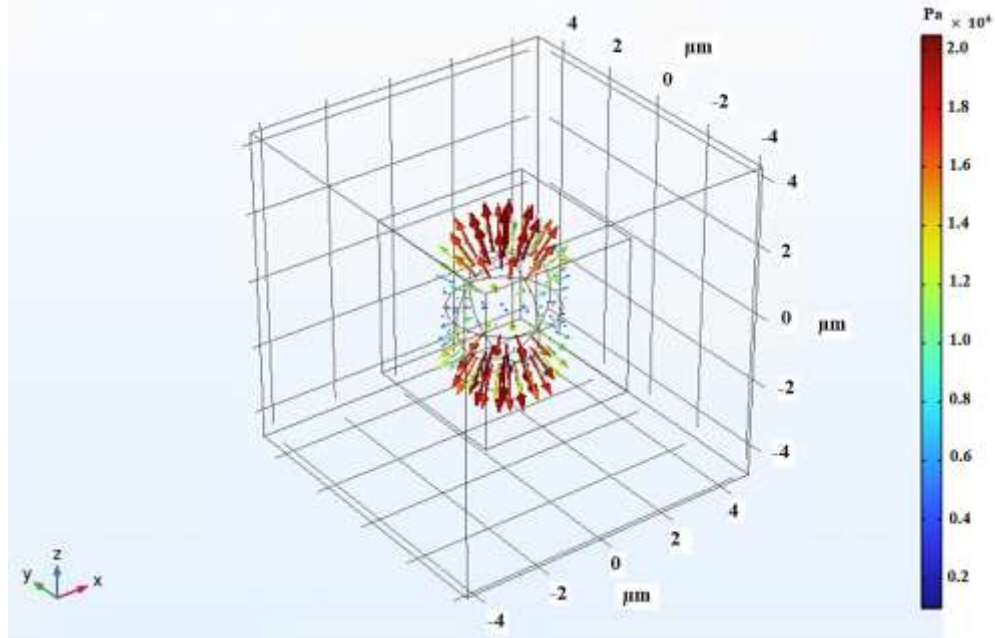


Figure 52: The magnetic boundary loads applied on the CIP inclusion boundaries under magnetic flux density of 0.1T. The color definition bar expresses the Maxwell upward stress tensor in Pa.

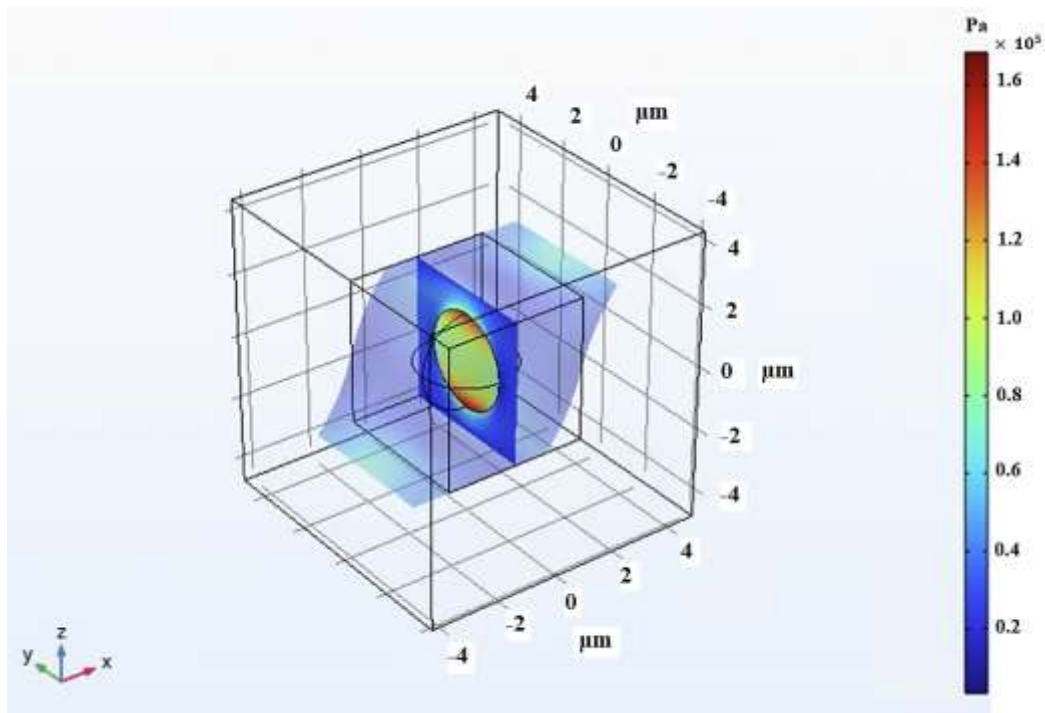


Figure 53: The shear deformation of MRE-RVE under 30% Shear strain, while the periodic boundary conditions are being applied on the RVE boundaries. The color definition bar depicts the Tresca stress in Pa.

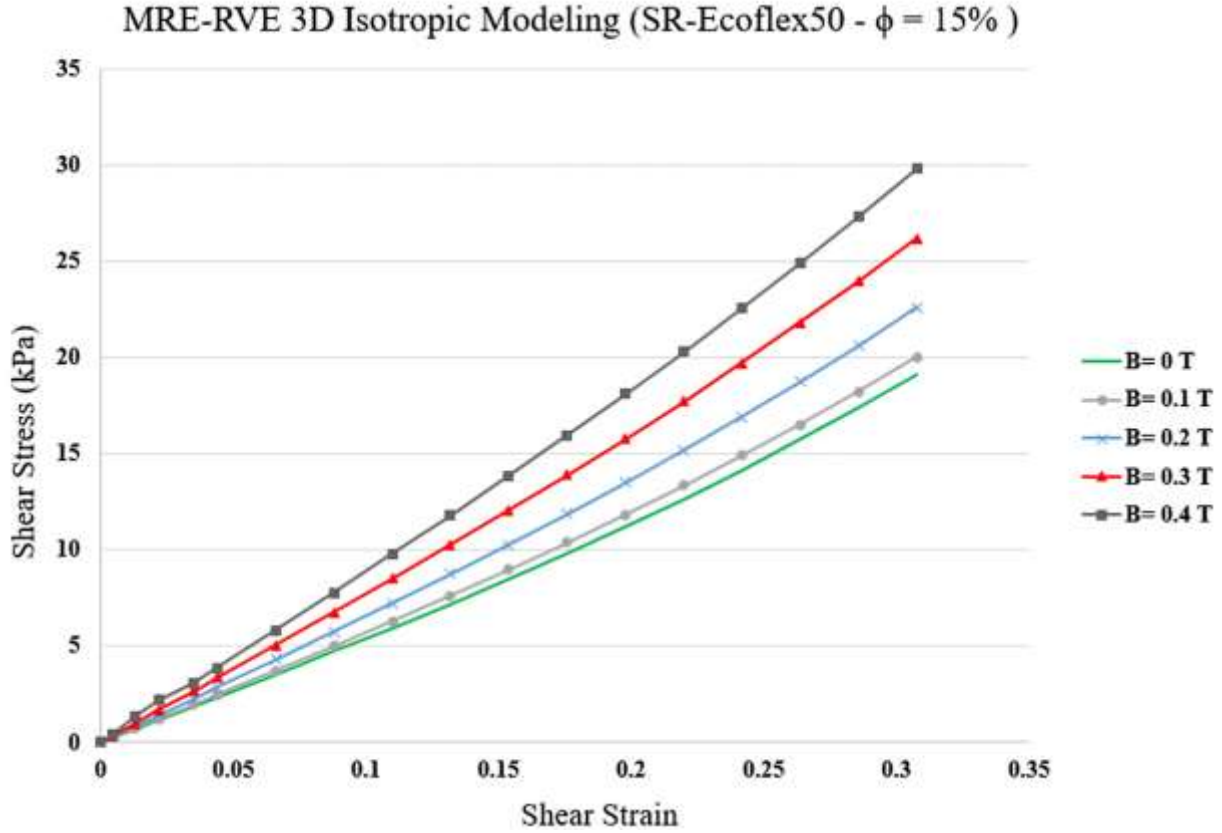


Figure 54: Shear stress- shear strain plot for 3D MRE-RVE (Ecoflex 50), containing 15% of CIP in volume fraction under different applied magnetic fields.

Examination of results in Fig. 54 reveals that as expected the shear modulus increases by increasing the magnetic field intensity. The variation of the predicted field-dependent shear modulus with respect to the applied magnetic flux density and its comparison with reported experimental results [55] is shown in Fig. 55. As it can be realized, unlike 2D MRE-RVE model, the 3D RVE can accurately predict the field-dependent shear modulus of the MRE up to 0.4T. For instance, the zero-field shear modulus of MRE-RVE obtained from Comsol FE 3D modeling is 55.15 kPa, which is only 1.3 % higher than the 54.43kPa zero-field shear modulus of MRE obtained experimentally.

In order to assure that the whole behavior of the MRE is captured accurately in the conducted FE modeling, the coefficient of determination (R^2) is determined, which is defined as $(1 - \frac{SS_{res}}{SS_{tot}})$. In which, SS_{res} is the sum of squared residuals (the differences between the predicted values and the actual values), and SS_{tot} is the total sum of squares, which measures the total variance of the predicted variable. If R^2 is determined to be close to 1, it means that the predicted values hold a perfect agreement with the actual values, while, R^2 value close to 0 indicates not a satisfying agreement between the values. Hence, R^2 was determined between the results from the modeling and the ones obtained from experiments [55], and a perfect agreement was assured by $R^2 = 0.999$.

We have attempted to evaluate the shear response behaviour of the 3D -RVE modeling for higher intensities of the applied magnetic field, beyond 0.4T, however the model fails due to the complex interaction between the mechanical and magnetic loads. Analyzing the results, we realized that the issue is likely due to the abrupt change in the material properties between an extremely soft rubber, and a rigid inclusion, along with the accumulated mechanical and magnetic nonlinearity associated with the stress and material behaviour. Several methods were employed to overcome the issue but without success, these include enhancing the mesh resolution around the inclusion by adding 10 mesh boundary layers, decreasing the matrix material nonlinearity by using other hyper-elastic material models like Neo-Hookean and Mooney-Rivlin, decreasing the nonlinearity in the B-H curve of CIP, remeshing the model during the simulation to assure maintaining a good mesh quality, and imposing different boundary conditions around the inclusion by assuming a thin elastic layer around the inclusion to smoothen the abrupt change between the two materials.

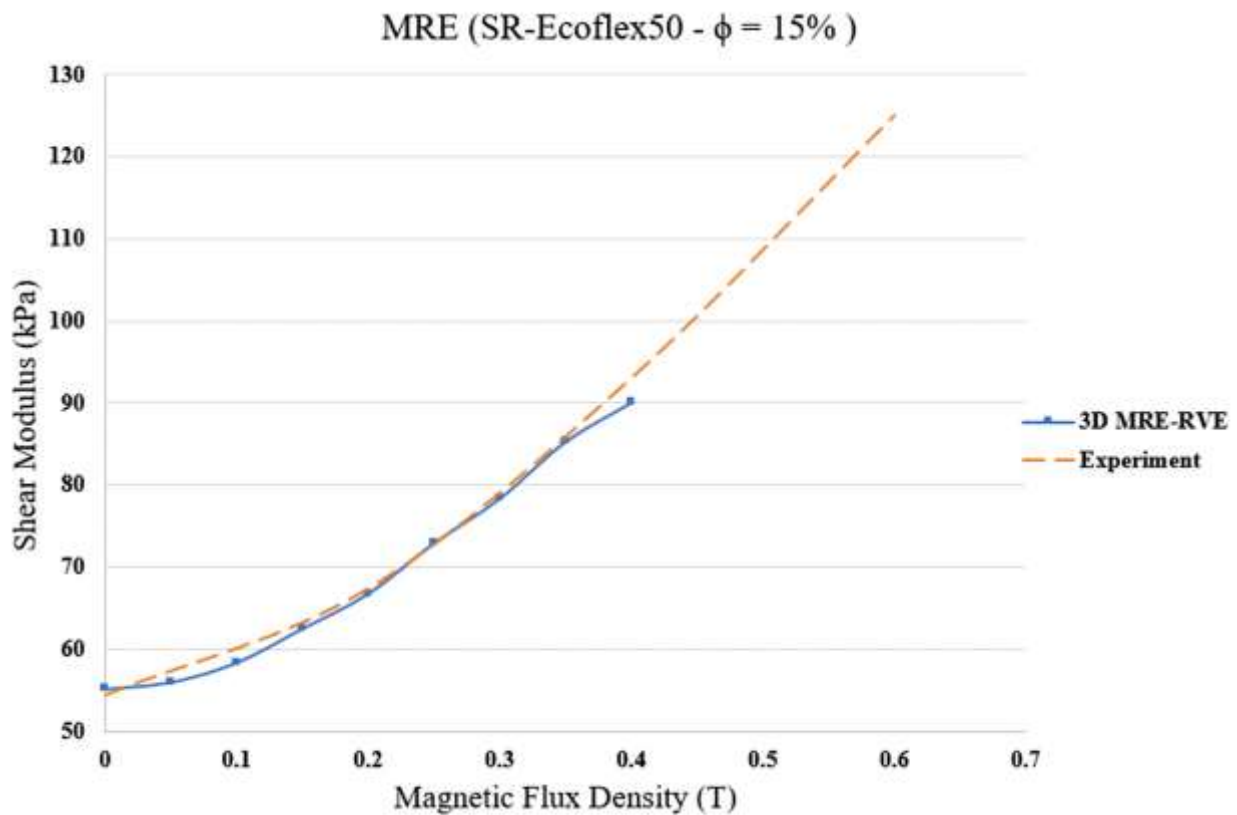


Figure 55: Shear modulus versus magnetic flux density for 3D isotropic MRE-RVE.

As discussed in section 1.7, previous research studies also encounter similar problem while modeling MRE-RVE even at very small intensities, while also ignoring the nonlinearities in the materials and modeling [55].

So, keeping the maximum magnetic flux density at 0.4T, we subsequently used the validated 3D MRE-RVE FE model to investigate the influence of CIP volume fraction, the MR effect, and matrix stiffness on the shear deformation response behaviour of MREs.

Results for shear stress-shear strain response concerning different CIP volume fraction, ranging from 5% to 40%, are illustrated in Figs. 56 (a – f).

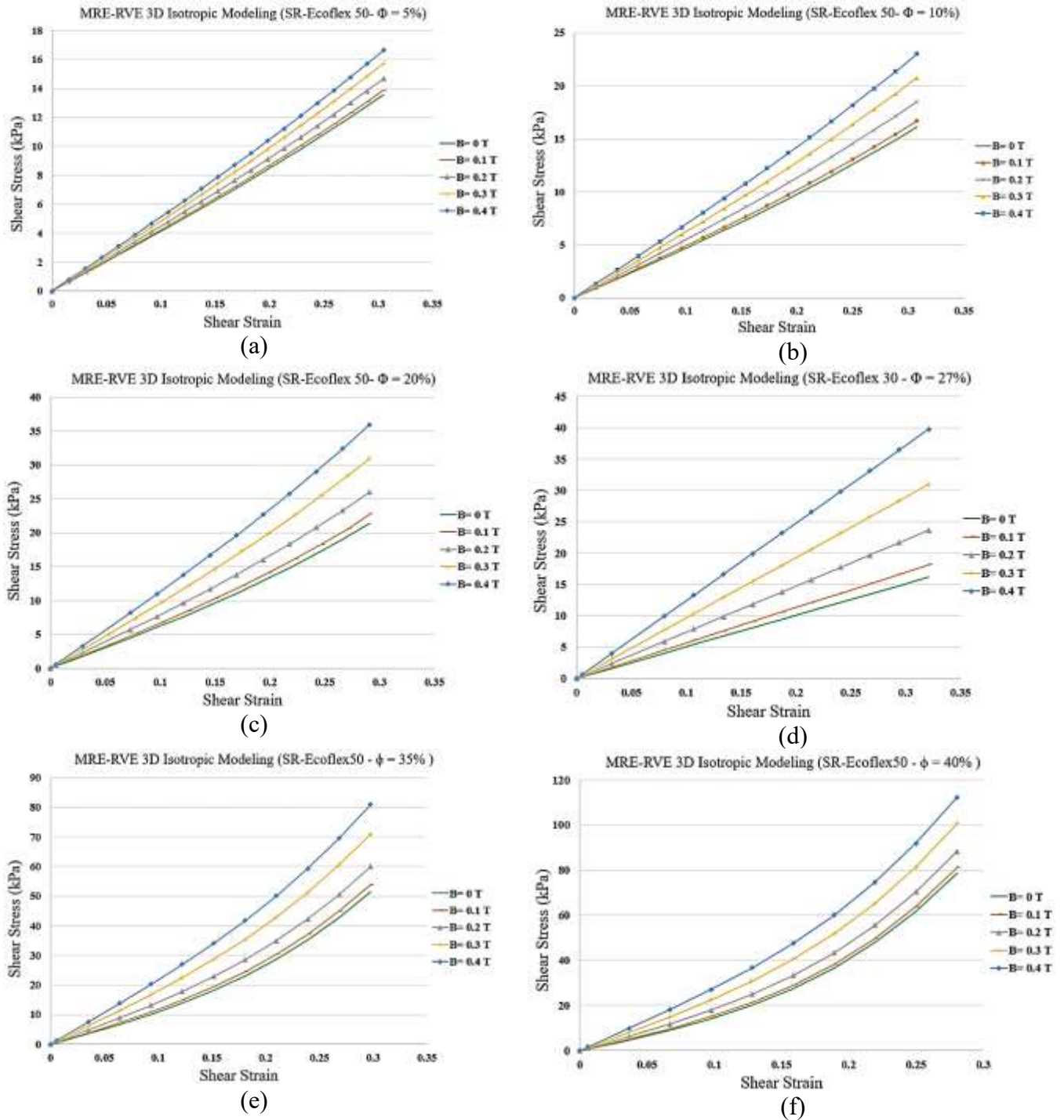


Figure 56: Shear stress- shear strain plot for 3D Isotropic MRE-RVE under different applied magnetic fields for silicone rubber (SR) Ecoflex 50 with (a) 5%, (b) 10%, (c) 20%, (d)27%, (e)35%, and (f) 40% of CIP in volume fraction.

Results show that the nonlinearity in the stress-strain curves increases by increasing the volume fraction of CIP and also by increasing the applied magnetic field. Results also show that increasing the volume fraction of CIP yields substantial increase in the induced shear stress at the given shear strain.

To have a better understanding of the influence of CIP volume fraction, the MR effect of the 3D MRE-RVEs with different volume fraction of CIP has been evaluated, considering that maximum shear modulus at 0.4T magnetic density. The results are shown in Fig. 57. Results clearly show that the relative MR effect initially increases as the CIP content increases, reaching to a maximum level of 92% at 27% volume fraction and then decreases with further increasing the volume fraction of CIP. This is in agreement with results reported by Davis [40].

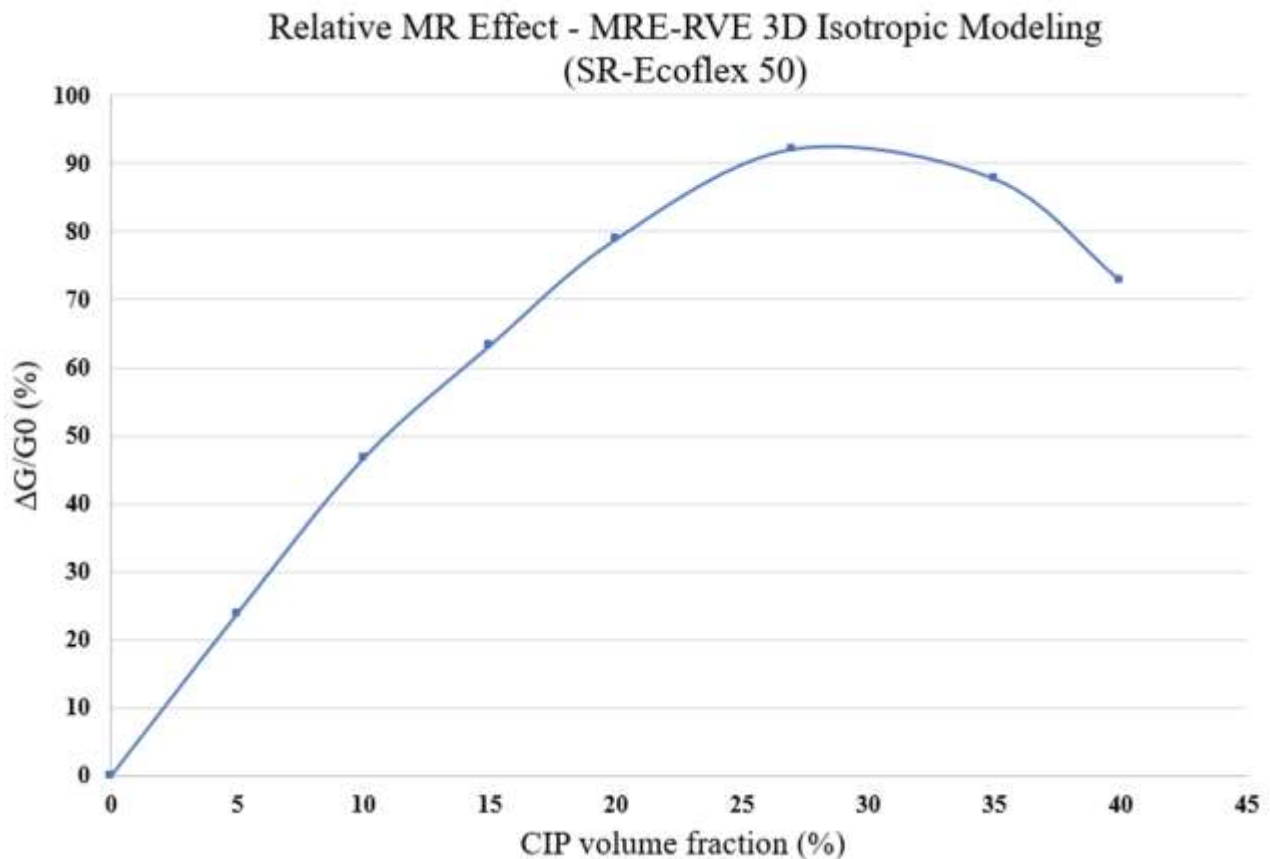


Figure 57: Relative MR effect for silicone rubber Ecoflex50 MRE-RVE versus CIP volume fraction.

4.2.3.2 Silicone Rubber Ecoflex 30 MRE-RVE

Next, the same procedure of FE modeling used for silicone rubber Ecoflex50 MRE-RVE, was conducted on MRE-RVE with silicone rubber Ecoflex30 as the matrix material. The influence of different magnetic flux densities, ranging from 0- 0.4T, was also studied on the shear stress-shear strain response of the silicone rubber Ecoflex 30 MRE-RVEs containing various CIP content.

Fig. 58 shows the shear stress-shear strain behavior of Ecoflex 30 MRE-RVEs with 15% volume fraction of CIP, under varied magnetic flux densities ranging from 0 to 0.4T. Results clearly suggest that MRE-RVE with Ecoflex 30 as the matrix shows lower stiffness compared with MRE-RVE with Ecoflex 50 in Fig. 54 and, thus, more pronounced relative MR effect.

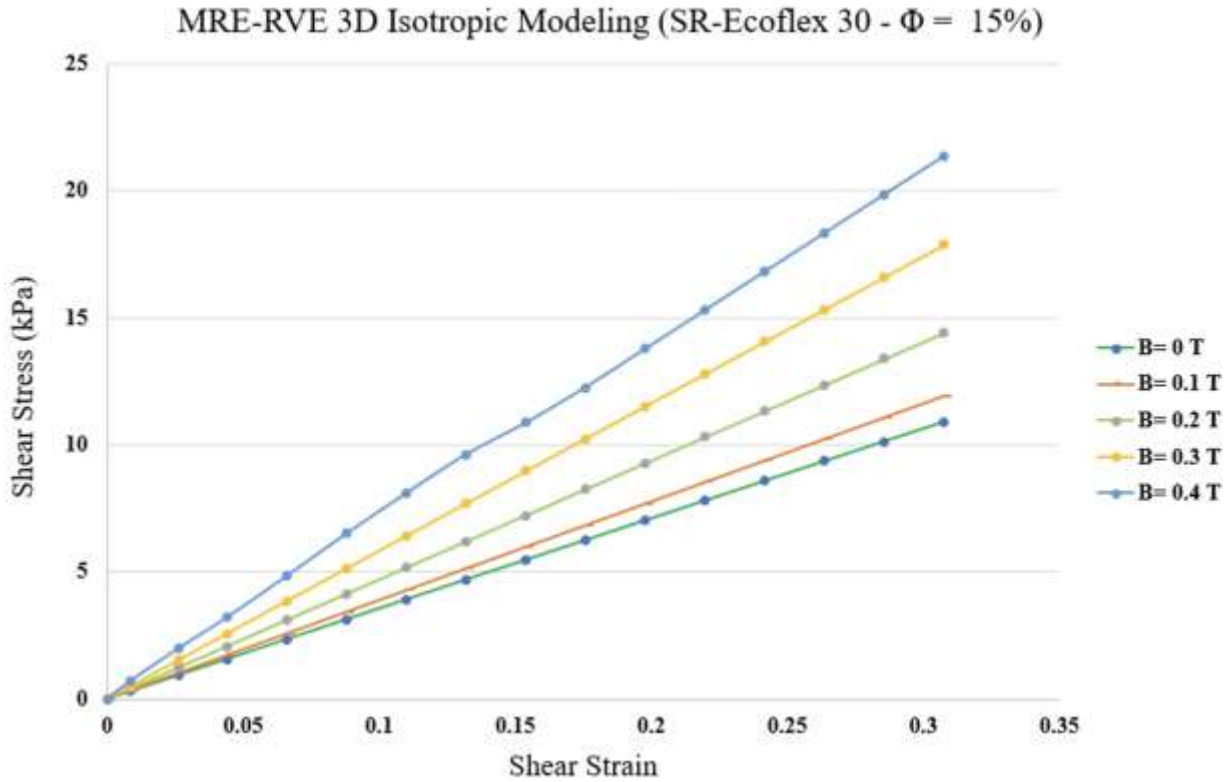
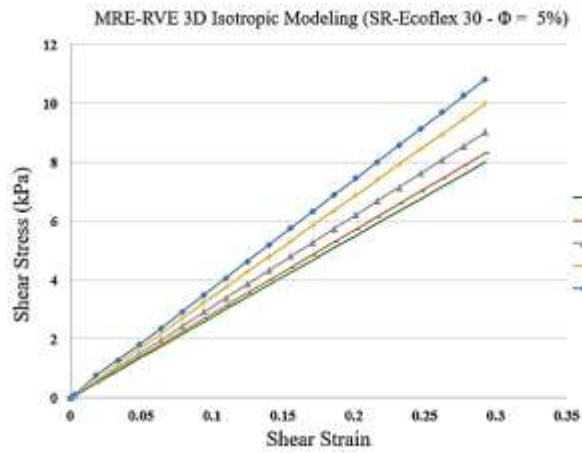
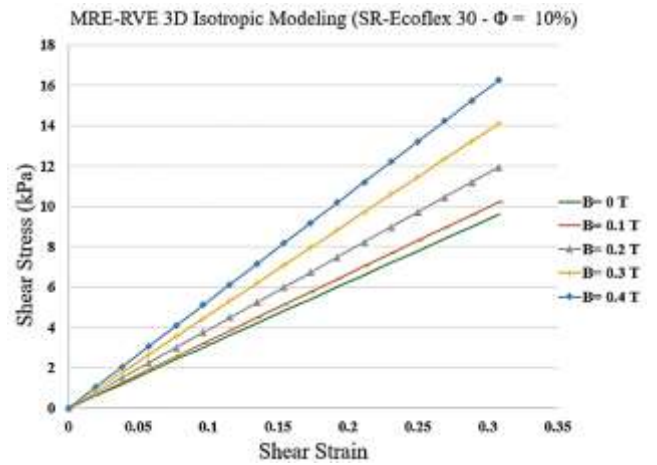


Figure 58: MRE-RVE (Ecoflex30) shear stress- strain behaviour under the application of different magnetic fields.

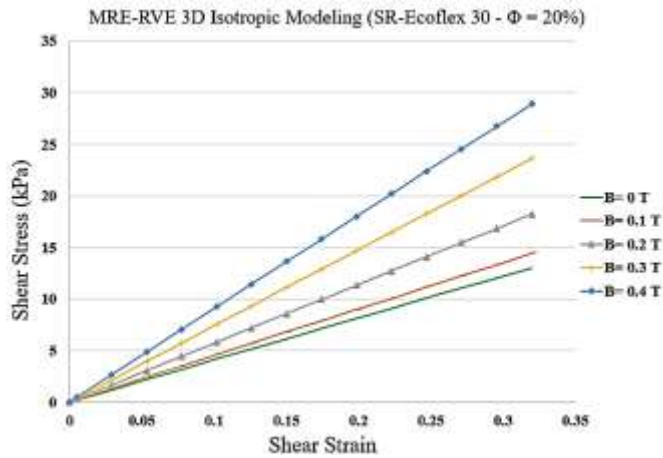
Similar to MRE-RVE with Ecoflex 50, the effect of volume fraction of CIP on the shear stress-shear strain response of 3D MRE-RVE with Ecoflex 30 has also been investigated and results are shown in Figs. 59 (a-f). Results suggest that increasing the CIP content in MRE-RVE with Ecoflex 30 has more pronounced effect on the relative MR effect compared with MRE-RVE with Ecoflex 50. The effect of volume fraction of CIP can be better understood in Fig. 60 which shows the variation of relative MR effect with respect to CIP volume fraction. Fig. 60 shows that the relative MR effect for MRE-RVE with Ecoflex 30, as the matrix will reach to its peak at CIP volume fraction of nearly 35%, which was anticipated due to using a softer matrix [31].



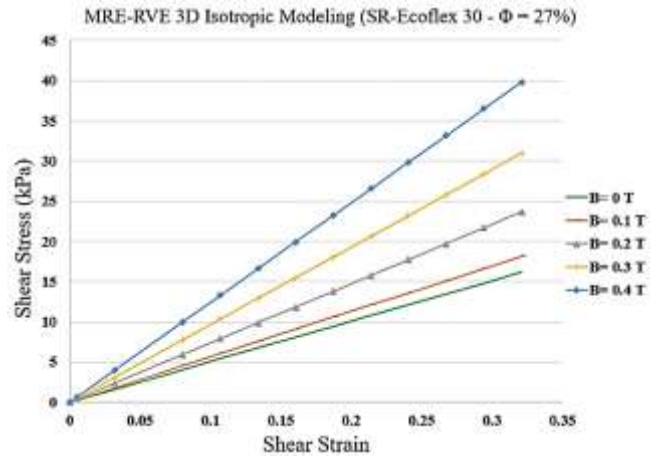
(a)



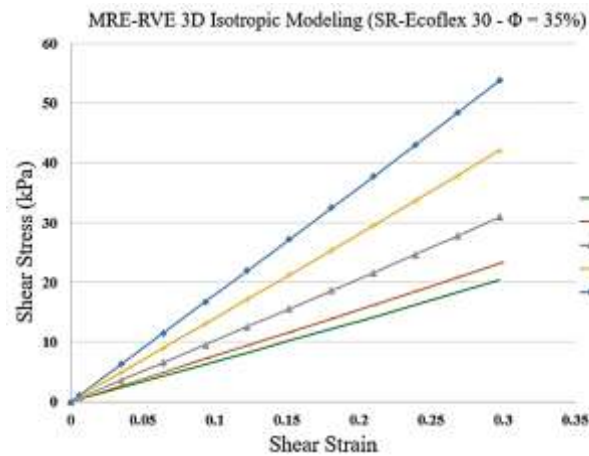
(b)



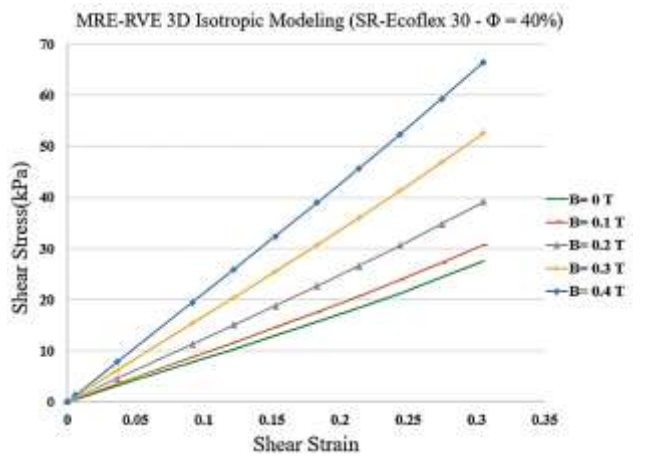
(c)



(d)



(e)



(f)

Figure 59: Shear stress- shear strain plot for 3D Isotropic MRE-RVE under different applied magnetic fields for silicone rubber Ecoflex 30 with (a) 5%, (b) 10%, (c) 20%, (d) 27%, (e) 35%, and (f) 40% of CIP in volume fraction.

Comparison of results for MRE-RVE Ecoflex 30 with those of MRE-RVE Ecoflex 50 reveals that the maximum relative MR effect in MREs with the softer matrix (silicone rubber Ecoflex 30) is noticeably higher than that of MREs with silicone rubber Ecoflex 50 which has also been confirmed by other studies [31, 55].

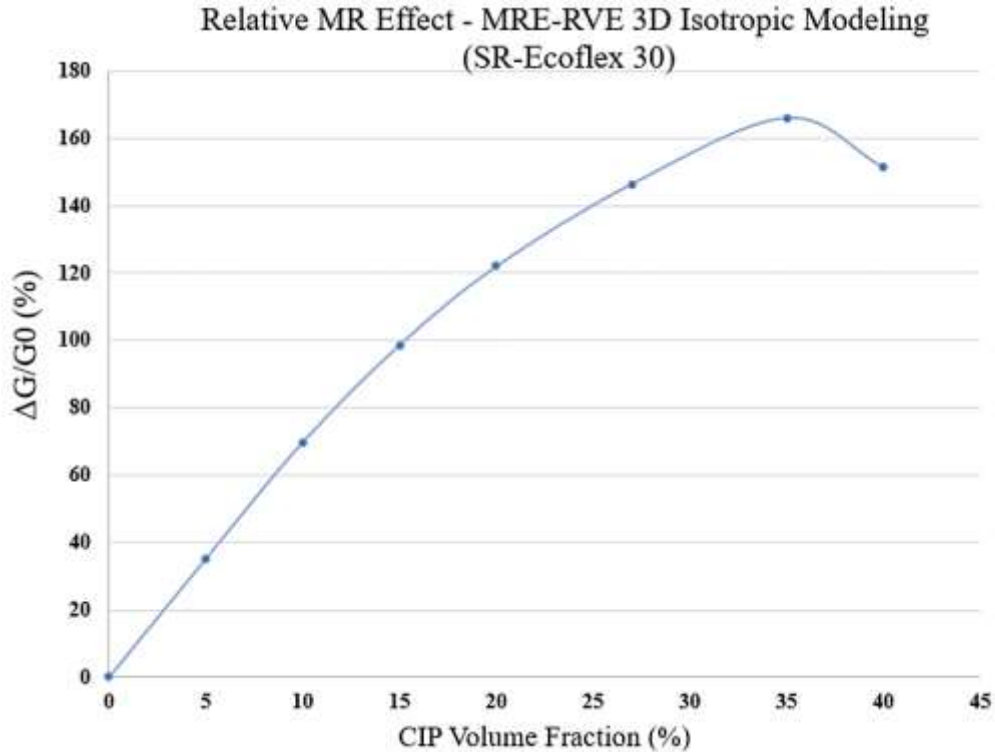


Figure 60: Relative MR effect versus CIP volume fraction obtained from isotropic 3D MRE-RVE for silicone rubber Ecoflex30.

Fig. 61 illustrates this considerable difference between the relative MR effect obtained from MRE-RVEs with different host rubber matrices. The maximum MR effect obtained from softer matrix was observed to be nearly 166% at 35% volume fraction of CIP compared with nearly 92% MR effect at 27% volume fraction CIP for silicone rubber Ecoflex50, both under the application of magnetic flux density of 0.4T.

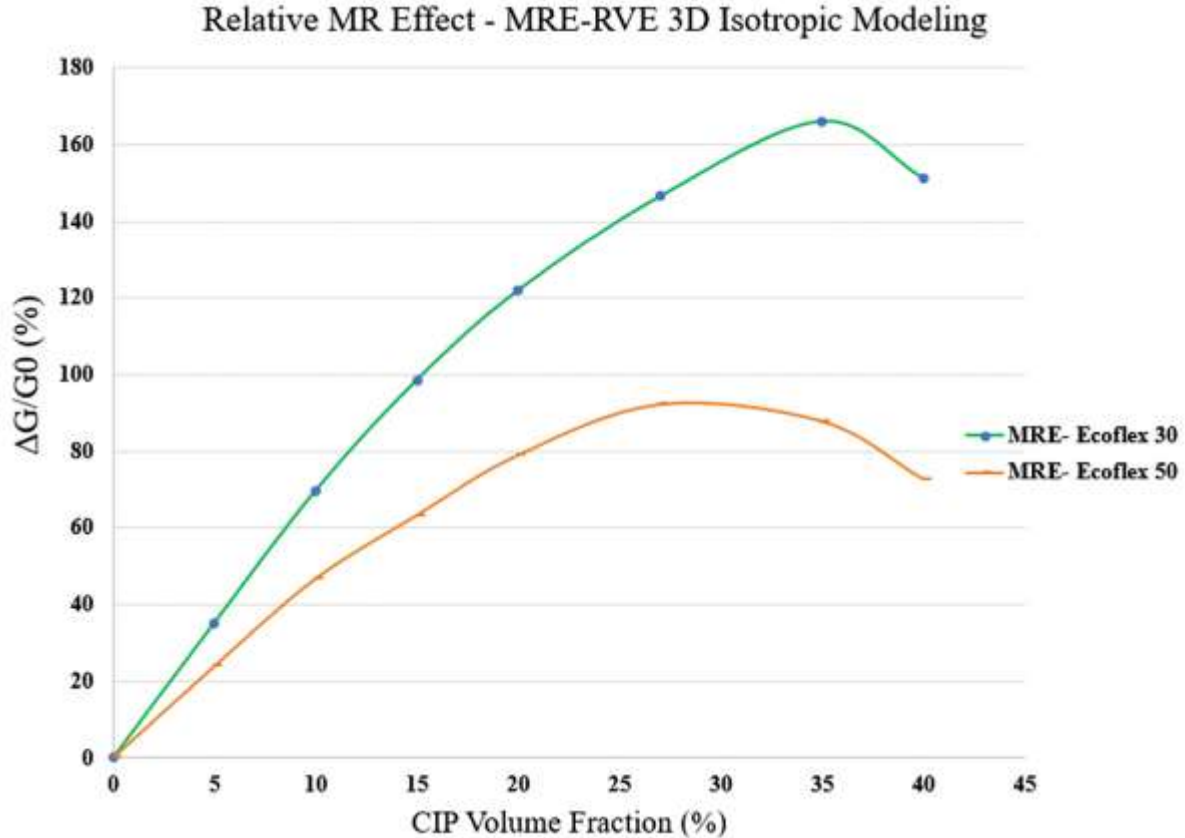


Figure 61: Comparing MR effect versus CIP volume fraction obtained from 3D Isotropic MRE-RVE for silicone rubber Ecoflex 30 and silicone rubber Ecoflex 50.

4.3 Summary and Conclusion

In this Chapter, the obtained material properties for the matrix and inclusions, as discussed in Chapter 3, were integrated into the FE modeling analysis for developing the MRE-RVEs in 2D and 3D configurations. The FE analysis was conducted using Comsol Multiphysics (6.0). The study focused on isotropic MREs, in which the magnetic particles are uniformly and randomly distributed within the host elastomeric matrix.

The modeling in both configurations, concerned the pure shear deformation of MRE-RVEs under the application of an external magnetic field, investigating the influence of varied magnetic flux densities, CIP content and the host rubber's hyper-elastic behavior on the shear modulus of the MREs. The MR effect behavior of the MRE-RVEs are also studied and compared.

The analysis started with a comprehensive study on the 2D MRE-RVEs, generated as a simple square with one circular inclusion inside, surrounded by air. The MRE-RVE underwent incremental pure shear deformation up to 30%, while PBC was defined on the boundaries. A homogeneous magnetic field was simultaneously applied on the MRE-RVE, perpendicular to the direction of shear deformation. The homogenized shear modulus of the MRE-RVE was then determined concerning varied magnetic flux densities ranging (0- 0.7T), CIP content and different host elastomers, being silicone rubber Ecoflex 30 and Ecoflex 50.

The results showed that the shear modulus in the MRE-RVE increases as the magnetic flux density goes up. Comparing the 2D results for Ecoflex 50 with the experimental results in the literature [55] revealed that although the 2D modeling can predict the MRE's behaviour within $\pm 20\%$ difference with the experimental results, and shows the saturation effect, it cannot accurately predict the variation of MR effect with respect to CIP volume fraction. The relative MR effect in the 2D MRE-RVE increases with the CIP volume fraction going up, however, the MR effect is supposed to reach a peak at the optimum volume fraction, followed by a decrease as the volume fraction increases further. These differences between the results obtained from the modeling and the experiments could be attributed to the incapability of 2D model to capture the whole physical phenomenon, as in 2D RVE model, an extruded depth should be assigned to the plane geometry. Thus, the inclusion is in fact considered as a cylindrical short fiber which is different from the geometry of the nearly spherical inclusion in reality.

Hence, the study delved into conducting the FE analysis on the 3D MRE-RVE. The analysis started with a detailed investigation on various typical RVE arrangements, comparing the obtained homogenized shear modulus with the experimental results in the literature [55]. Results suggested that simple cubic RVE arrangement, as a simple cube with one spherical inclusion generated inside holds a good agreement with the experimental results, offering a minor 1.3% difference. Therefore, the modeling was conducted on the simple cubic MRE-RVE with the same procedure outlined in 2D modeling.

The study was conducted on MRE-RVEs concerning varied magnetic flux densities (ranging 0-0.4T), CIP content and different host elastomers, being silicone rubber Ecoflex 30 and Ecoflex 50. The results suggested that the shear modulus increases as the magnetic flux density increases, in MRE-RVEs containing CIP volume fractions ranging 5%- 40%, with both silicone rubbers as the matrix material. Comparing the 3D results for Ecoflex 50 with the experimental results in the literature [55] revealed that the results of the 3D MRE-RVE modeling hold a perfect agreement with the experiments, offering a coefficient of determination (R^2) of 0.999. Exploring the MR effect in the 3D MRE-RVE, revealed that the relative MR effect in the MRE-RVE with the softer matrix material (Ecoflex 30), is higher than that of Ecoflex 50 MRE-RVE. The 3D modeling is also able to predict the MR effect variation with respect to CIP volume fraction accurately. The results suggested that the relative MR effect in Ecoflex 30 MRE-RVE keeps increasing up to 35% volume fraction of CIP, peaking at 166%, while the MR effect in MRE-RVE with Ecoflex 50 reaches a maximum of 92% at 27% CIP content.

Chapter 5: Contributions, Conclusion and Future Remarks

5.1 Major Contributions

This research thesis aimed to propose a simple yet comprehensive microscale model for predicting the magnetic-mechanical properties of MREs at the macroscale. By obviating the need for expensive experimental approaches, the objective was to offer a cost-effective method for predicting the mechanical properties of MREs. The main goal was to fill the current research gap concerning development of a numerical finite element model by RVE approach to predict the behaviour of MREs under the influence of applied magnetic field with all the nonlinearities in material models (both mechanical and magnetic) taken into account. The key contributions of this thesis can be outlined as follows:

- I. Development of a simple microscale 2D and 3D RVE finite element models to predict the macroscale magnetic field-induced properties of isotropic MREs.
- II. Incorporation of the nonlinear Ogden model and design of an experiment to characterize the highly nonlinear hyper-elastic behaviour of elastomeric matrix.
- III. Systematic investigation to realize the effect of external magnetic field, volume fraction of CIP and the type of matrix on the mechanical response and relative MR effect of MREs.

5.2 Major Conclusions

This dissertation research delves into the intricate nonlinear stress-strain characteristics exhibited by magnetorheological elastomers, using a finite element numerical model, adopting the RVE approach. The key findings derived from this comprehensive investigation are outlined below:

- I. The proposed 2D MRE-RVE was not able to predict the whole magneto-mechanical behaviour of MREs with an acceptable accuracy range, however, it could capture the increase of the magnetic field-induced shear modulus up to saturation within $\pm 20\%$ difference with the experimental results.
- II. The developed 3D MRE-RVE model was able to accurately predict the mechanical response behaviour of MREs under varied magnetic flux densities.
- III. The CIP concentration within the elastomeric matrix of MRE intricately governs the magneto-mechanical properties. An augmentation in the volume fraction of CIP

significantly increases the MR effect, manifesting as a jump in the modulus of the MRE under the influence of an applied magnetic field.

- IV. The relative MR effect increases with increasing volume fraction of CIP up to certain level namely the critical or optimum content of CIP and further addition of CIP decreases the MR effect. The conventional critical ferromagnetic particle content is suggested to be 27% in volume fraction, however, by using a softer host rubber and/or softening the rubber matrix using additives, further increase in the iron particle content can result in higher MR effect.
- V. The relative MR effect achieved in MREs with softer host rubber is much higher compared to MREs with stiffer rubber matrix under identical conditions. For example, the MR effect in shear modulus for silicone rubber Ecoflex 30 was calculated to be 166% at 35% CIP volume fraction while silicone rubber Ecoflex 50 offered an MR effect of 92% at 27% of CIP volume fraction, both under 0.4T magnetic field.

5.3 Future Remarks

This research thesis has been instrumental in clarifying the complexities associated with modeling the macroscopic field-dependent mechanical responses of Magnetorheological Elastomers (MREs) using microscale RVE approach and considering nonlinear behaviors exhibited by both the matrix elastomer and magnetic particles. However, the complexities inherent in this domain leaves avenues for further investigation in future studies. Addressing these remaining questions will contribute not only to the modeling of MREs behaviour but also to the broader understanding of their application and potential advancements in the field.

- I. Proposing an RVE model for predicting the behaviour of anisotropic MREs containing chain-like ferromagnetic particles, considering the nonlinear mechanical and magnetic behaviour of MRE components.
- II. Conducting dynamic shear deformation on the proposed RVE, incorporating damping to investigate the linear and nonlinear viscoelastic behaviour of MREs under varying excitation frequency and strain amplitude.
- III. Proposing a new approach to develop 3D MRE-RVE model capable of predicting the mechanical response of MREs under higher magnetic field intensities up to saturation.
- IV. Developing a data-driven model using machine learning techniques to efficiently predict the viscoelastic behaviour of MREs under different loading scenarios.

References

1. Carlson JD, Jolly M. (2000) MR Fluid, foam and elastomer devices. *Mechatronics* 10 114:236–240
2. Bastola AK, Paudel M, Li L, Li W (2020) Recent progress of magnetorheological elastomers: A review. *Smart Mater Struct.* <https://doi.org/10.1088/1361-665X/abbc77>
3. Saber A, Sedaghati R (2023) The Modeling of Magnetorheological Elastomers: A State-of-the-Art Review. *Adv Eng Mater.* <https://doi.org/10.1002/adem.202300182>
4. Li Y, Li J, Li W, Du H (2014) A state-of-the-art review on magnetorheological elastomer devices. *Smart Mater Struct.* <https://doi.org/10.1088/0964-1726/23/12/123001>
5. Liu Y (2023) A review on magnetorheological elastomers. *Adv Eng Technol Res* 4:503
6. Bastola AK, Hossain M (2020) A review on magneto-mechanical characterizations of magnetorheological elastomers. *Compos Part B Eng* 200:108348
7. Jaafar MF, Mustapha F, Mustapha M (2021) Review of current research progress related to magnetorheological elastomer material. *J Mater Res Technol* 15:5010–5045
8. Cantera MA, Behrooz M, Gibson RF, Gordaninejad F (2017) Modeling of magneto-mechanical response of magnetorheological elastomers (MRE) and MRE-based systems: A review. *Smart Mater Struct.* <https://doi.org/10.1088/1361-665X/aa549c>
9. Díez AG, Tubio CR, Etxebarria JG, Lanceros-Mendez S (2021) Magnetorheological Elastomer-Based Materials and Devices: State of the Art and Future Perspectives. *Adv Eng Mater* 23:1–20
10. Li WH, Zhang XZ, Du H (2013) Magnetorheological Elastomers and Their Applications. 357–374
11. Li W, Zhang X (2010) Research and Applications of MR Elastomers. *Recent Patents Mech Eng* 1:161–166
12. Ubaidillah, Sutrisno J, Purwanto A, Mazlan SA (2015) Recent progress on magnetorheological solids: Materials, fabrication, testing, and applications. *Adv Eng Mater* 17:563–597
13. Sharif U, Sun B, Hussain S, Ibrahim DS, Adewale OO, Ashraf S, Bashir F (2021) Dynamic behavior of sandwich structures with magnetorheological elastomer: A review. *Materials (Basel).* <https://doi.org/10.3390/ma14227025>
14. Faizal Johari MA, Mazlan SA, Ubaidillah, Harjana, Abdul Aziz SA, Nordin NA, Johari N, Nazmi N (2020) An Overview of Durability Evaluations of Elastomer-Based Magnetorheological Materials. *IEEE Access* 8:134536–134552
15. Ginder JM, Nichols ME, Elie LD, Tardiff JL (1999) Magnetorheological elastomers: properties and applications. *Smart Struct Mater* 1999 *Smart Mater Technol* 3675:131–138

16. Lokander M, Stenberg B (2003) Performance of isotropic magnetorheological rubber materials. *Polym Test* 22:245–251
17. Stepanov G V., Abramchuk SS, Grishin DA, Nikitin L V., Kramarenko EY, Khokhlov AR (2007) Effect of a homogeneous magnetic field on the viscoelastic behavior of magnetic elastomers. *Polymer (Guildf)* 48:488–495
18. Duan Y, Li G, Liu L, Liu S (2010) Electromagnetic properties of carbonyl iron and their microwave absorbing characterization as filler in silicone rubber. *Bull Mater Sci* 33:633–636
19. Filipcsei G, Csetneki I, Szilágyi A, Zrínyi M (2007) Magnetic field-responsive smart polymer composites. *Adv Polym Sci* 206:137–189
20. Liu T, Xu Y (2019) Magnetorheological Elastomers: Materials and Applications. *Smart Funct Soft Mater*. <https://doi.org/10.5772/intechopen.85083>
21. Shit SC, Shah P (2013) A review on silicone rubber. *Natl Acad Sci Lett* 36:355–365
22. Chen L, Gong XL, Jiang WQ, Yao JJ, Deng HX, Li WH (2007) Investigation on magnetorheological elastomers based on natural rubber. *J Mater Sci* 42:5483–5489
23. Ahmad Khairi MH, Mazlan SA, Ubaidillah, Choi SB, Abdul Aziz SA, Mohamad N, Hapipi NM, Nordin N (2019) Role of Additives in Enhancing the Rheological Properties of Magnetorheological Solids: A Review. *Adv Eng Mater* 21:1–13
24. Khairi MHA, Fatah AYA, Mazlan SA, Ubaidillah U, Nordin NA, Ismail NIN, Choi SB, Aziz SAA (2019) Enhancement of particle alignment using silicone oil plasticizer and its effects on the field-dependent properties of magnetorheological elastomers. *Int J Mol Sci*. <https://doi.org/10.3390/ijms20174085>
25. Khairi MHA, Noor EEM, Ubaidillah U, Aziz SAA, Mazlan SA, Tarmizi SMA, Nordin NA (2022) Enhancement of Magneto-Induced Modulus by the Combination of Filler and Plasticizer Additives-Based Magnetorheological Elastomer. *Materials (Basel)* 15:1–12
26. Gong XL, Zhang XZ, Zhang PQ (2005) Fabrication and characterization of isotropic magnetorheological elastomers. *Polym Test* 24:669–676
27. Leblanc JL (2002) Rubber-filler interactions and rheological properties in filled compounds. *Prog Polym Sci* 27:627–687
28. Barman H, Hegde S (2019) Comprehensive review of parameters influencing the performance of magnetorheological elastomers embedded in beams. *Mater Today Proc* 26:2130–2135
29. Bastola AK, Hoang VT, Li L (2017) A novel hybrid magnetorheological elastomer developed by 3D printing. *Mater Des* 114:391–397
30. Bastola AK, Paudel M, Li L (2018) Development of hybrid magnetorheological elastomers by 3D printing. *Polymer (Guildf)* 149:213–228
31. Dargahi A, Sedaghati R, Rakheja S (2019) On the properties of magnetorheological elastomers in shear mode: Design, fabrication and characterization. *Compos Part B Eng*

159:269–283

32. Boczkowska A, Awietjan SF, Pietrzko S, Kurzydłowski KJ (2012) Mechanical properties of magnetorheological elastomers under shear deformation. *Compos Part B Eng* 43:636–640
33. Zhang J, Pang H, Wang Y, Gong X (2020) The magneto-mechanical properties of off-axis anisotropic magnetorheological elastomers. *Compos Sci Technol* 191:108079
34. Dong X, Ma N, Qi M, Li J, Chen R, Ou J (2012) The pressure-dependent MR effect of magnetorheological elastomers. *Smart Mater Struct*. <https://doi.org/10.1088/0964-1726/21/7/075014>
35. Wu J, Gong X, Fan Y, Xia H (2012) Improving the magnetorheological properties of polyurethane magnetorheological elastomer through plasticization. *J Appl Polym Sci* 123:2476–2484
36. Danas K, Kankanala S V., Triantafyllidis N (2012) Experiments and modeling of iron-particle-filled magnetorheological elastomers. *J Mech Phys Solids* 60:120–138
37. Jin Q, Xu YG, Di Y, Fan H (2015) Influence of the particle size on the rheology of magnetorheological elastomer. *Mater Sci Forum* 809–810:757–763
38. Winger J, Schümann M, Kupka A, Odenbach S (2019) Influence of the particle size on the magnetorheological effect of magnetorheological elastomers. *J Magn Magn Mater* 481:176–182
39. Kallio M (2005) The elastic and damping properties of magnetorheological elastomers.
40. Davis LC (1999) Model of magnetorheological elastomers. *J Appl Phys* 85:3348–3351
41. Chen L, Gong XL, Li WH (2007) Microstructures and viscoelastic properties of anisotropic magnetorheological elastomers. *Smart Mater Struct* 16:2645–2650
42. Li W, Zhang X, Du H (2012) Development and simulation evaluation of a magnetorheological elastomer isolator for seat vibration control. *J Intell Mater Syst Struct* 23:1041–1048
43. Kordonsky WI (1993) Magnetorheological effect as a base of new devices and technologies. *J Magn Magn Mater* 122:395–398
44. Ginder JM, Schlotter WF, Nichols ME (2001) <title>Magnetorheological elastomers in tunable vibration absorbers</title>. *Smart Struct Mater 2001 Damping Isol* 4331:103–110
45. Deng HX, Gong XL (2007) Adaptive tuned vibration absorber based on magnetorheological elastomer. *J Intell Mater Syst Struct* 18:1205–1210
46. Rasooli A, Sedaghati R, Hemmatian M (2020) A novel magnetorheological elastomer-based adaptive tuned vibration absorber: Design, analysis and experimental characterization. *Smart Mater Struct*. <https://doi.org/10.1088/1361-665X/abb575>
47. Tao Y, Rui X, Yang F, Chen G, Bian L, Zhu W, Wei M (2018) Design and experimental research of a magnetorheological elastomer isolator working in squeeze/elongation–shear

- mode. *J Intell Mater Syst Struct* 29:1418–1429
48. Jolly J (1995) Particles Respond By Attempting. 613–622
 49. Dorfmann A, Ogden RW (2004) Nonlinear magnetoelastic deformations of elastomers. *Acta Mech* 167:13–28
 50. Berasategi J, Salazar D, Gomez A, Gutierrez J, Sebastián MS, Bou-Ali M, Barandiaran JM (2020) Anisotropic behaviour analysis of silicone/carbonyl iron particles magnetorheological elastomers. *Rheol Acta* 59:469–476
 51. Vatandoost H, Sedaghati R, Rakheja S, Hemmatian M (2021) Effect of pre-strain on compression mode properties of magnetorheological elastomers. *Polym Test* 93:106888
 52. Shen Y, Golnaraghi MF, Heppler GR (2004) Experimental research and modeling of magnetorheological elastomers. *J Intell Mater Syst Struct* 15:27–35
 53. Nam TH, Petriková I, Marvalová B (2020) Experimental characterization and viscoelastic modeling of isotropic and anisotropic magnetorheological elastomers. *Polym Test*. <https://doi.org/10.1016/j.polymertesting.2019.106272>
 54. Syam TMI, Muthalif AGA, Salem AMH, Hejazi AAA (2020) 3D numerical modelling and analysis of a magnetorheological elastomer (MRE). *J Vibroengineering* 22:1251–1265
 55. Asadi Khanouki M, Sedaghati R, Hemmatian M (2019) Experimental characterization and microscale modeling of isotropic and anisotropic magnetorheological elastomers. *Compos Part B Eng* 176:107311
 56. Norouzi M, Gilani M, Alehashem SMS, Vatandoost H (2017) Dynamic Characterization and Modeling of Isotropic Magnetorheological Elastomers under Tensile-Compressive Loadings. *IEEE Trans Magn*. <https://doi.org/10.1109/TMAG.2017.2698403>
 57. Ardehali NM, Hemmatian M, Sedaghati R (2021) Characterization and modeling of hard magnetic particle-based magnetorheological elastomers. *J Intell Mater Syst Struct* 32:909–920
 58. Sun S, Peng X, Guo Z (2014) Study on macroscopic and microscopic mechanical behavior of magnetorheological elastomers by representative volume element approach. *Adv Condens Matter Phys*. <https://doi.org/10.1155/2014/232510>
 59. Xu H, Ye L Characterization and Simulation of Magnetorheological Elastomer Filled with Carbonyl Iron and NdFeB Particles under Uniaxial Tension, Compression, and Pure Shear Modes.
 60. Kiarie WM, Jiles DC (2015) Modeling Of Effect Of Particle Size On Macroscopic Behavior Of Magnetorheological Elastomers. 809:2–4
 61. Li R, Ma S, Jin F, Yin S, Nian C, Xin N, Yu Q (2023) Coupled multi-physics field simulation research of magneto-rheological elastomeric magneto-shear mechanical properties based on COMSOL. 34
 62. Hill R (1963) Elastic properties of reinforced solids: Some theoretical principles. *J Mech Phys Solids* 11:357–372

63. Hashin Z (1983) Analysis of Composite Materials. *J Appl Mech* 50:481–505
64. Evesque P (2005) Fluctuations, Correlation and Representative Elementary Volume (REV) in Granular Materials. 2023
65. El Moumen A, Kanit T, Imad A (2021) Numerical evaluation of the representative volume element for random composites. *Eur J Mech A/Solids* 86:104181
66. Madi K, Forest S, Jeulin D, et al (2007) Estimating RVE sizes for 2D / 3D viscoplastic composite materials To cite this version : Estimating RVE sizes for 2D / 3D viscoplastic composite materials.
67. El Moumen A, Imad A, Kanit T, Hilali E, El Minor H (2014) A multiscale approach and microstructure design of the elastic composite behavior reinforced with natural particles. *Compos Part B Eng* 66:247–254
68. Dirrenberger J, Forest S, Jeulin D (2014) Towards gigantic RVE sizes for 3D stochastic fibrous networks. *Int J Solids Struct* 51:359–376
69. Auriault JL (1991) Heterogeneous medium. Is an equivalent macroscopic description possible? *Int J Eng Sci* 29:785–795
70. Moumen A El, Kanit T, Imad A, Minor HEL (2013) Effect of overlapping inclusions on effective elastic properties of composites. *Mech Res Commun* 53:24–30
71. Kanit T, Forest S, Galliet I, Mounoury V, Jeulin D (2003) Determination of the size of the representative volume element for random composites: Statistical and numerical approach. *Int J Solids Struct* 40:3647–3679
72. Jeulin D (2012) Morphology and effective properties of multi-scale random sets: A review. *Comptes Rendus - Mec* 340:219–229
73. Willot F, Jeulin D (2009) Elastic behavior of composites containing Boolean random sets of inhomogeneities. *Int J Eng Sci* 47:313–324
74. Jeong S, Lim H, Zhu F, Yun G (2017) A Study on Effective Properties of Heterogeneous Representative Volume Element under Various Boundary Conditions. *Advances Struct. Eng. Mech.*
75. Amieur M, Hazanov S, Huet C, Polytechnique E, Lausanne F De (1995) an 149. *M*:149–150
76. Hazanov S (1998) Hill condition and overall properties of composites. *Arch Appl Mech* 68:385–394
77. Hazanov S, Huet C (1994) Order relationships for boundary conditions effect in heterogeneous bodies smaller than the representative volume. *J Mech Phys Solids* 42:1995–2011
78. Suquet P (1987) Elements of homogenization for in solid mechanics. *Lect Notes Phys* 272:193–278
79. Anthoine A (1995) Derivation of the in-plane elastic characteristics of masonry through



- homogenization theory. *Int J Solids Struct* 32:137–163
80. Terada K, Hori M, Kyoya T, Kikuchi N (2000) Simulation of the multi-scale convergence in computational homogenization approaches. *Int J Solids Struct* 37:2285–2311
 81. Van Der Sluis O, Schreurs PJG, Brekelmans WAM, Meijer HEH (2000) Overall behaviour of heterogeneous elastoviscoplastic materials: Effect of microstructural modelling. *Mech Mater* 32:449–462
 82. Okereke MI, Akpoyomare AI (2013) A virtual framework for prediction of full-field elastic response of unidirectional composites. *Comput Mater Sci* 70:82–99
 83. Swan CC (1994) Techniques for stress- and strain-controlled homogenization of inelastic periodic composites. *Comput Methods Appl Mech Eng* 117:249–267
 84. Smit RJM, Brekelmans WAM, Meijer HEH (1999) Prediction of the large-strain mechanical response of heterogeneous polymer systems: Local and global deformation behaviour of a representative volume element of voided polycarbonate. *J Mech Phys Solids* 47:201–221
 85. Nguyen QH, Choi SB, Lee YS, Han MS (2009) An analytical method for optimal design of MR valve structures. *Smart Mater Struct*. <https://doi.org/10.1088/0964-1726/18/9/095032>
 86. Davis A, Onoochin V (2020) the Maxwell Stress Tensor and Electromagnetic Momentum. *Prog Electromagn Res Lett* 94:151–156
 87. Pao Y-H (1978) Electromagnetic forces in deformable continua. In: *Mech. today*. Vol. 4. (A78-35706 14-70) New York. pp 209–305
 88. Mishra P Maxwell ' s Stress Tensor and Electromagnetic Momentum. V:1–7
 89. Kim B, Lee SB, Lee J, Cho S, Park H, Yeom S, Park SH (2012) A comparison among Neo-Hookean model, Mooney-Rivlin model, and Ogden model for Chloroprene rubber. *Int J Precis Eng Manuf* 13:759–764
 90. Bergström J (2015) Elasticity/Hyperelasticity. *Mech Solid Polym*. <https://doi.org/10.1016/b978-0-323-31150-2.00005-4>
 91. Rackl M (2015) Curve Fitting for Ogden , Yeoh and Polynomial Models. *Ostbayerishce Tech Hochschule Regensburg* 18
 92. Ogden R, Saccomandi G, Sgura I, Ogden R, Saccomandi G, Sgura I, Ogden RW, Saccomandi G, Sgura I (2018) Fitting hyperelastic models to experimental data To cite this version : HAL Id : hal-01727230 Fitting hyperelastic models to experimental data. 34:484–502
 93. Rao DK, Kuptsov V (2015) Effective Use of Magnetization Data in the Design of Electric Machines with Overfluxed Regions. *IEEE Trans Magn*. <https://doi.org/10.1109/TMAG.2015.2397398>
 94. <https://www.gosupps.com/bbdino-super-elastic-silicone-mold-making-kit-mold-making->

[silicone-rubber-n-w-21-16-oz-liquid-silicone-rubber-mold-making-ideal-for-casting-3d-silicone-molds-food-molds-1-1-by-volume-jade-green.html](#)

Technical bulletin of Ecoflex series silicone rubber

Ecoflex™ Series

Super-Soft, Addition Cure Silicone Rubbers

www.smooth-on.com

Cured Material
Certified Skin Safe!

PRODUCT OVERVIEW

Ecoflex™ rubbers are platinum-catalyzed silicones that are versatile and easy to use. Ecoflex™ rubbers are mixed 1A:1B by weight or volume and cured at room temperature with negligible shrinkage. Low viscosity ensures easy mixing and de-airing, or you can choose to mix and dispense using our convenient dispensing cartridges. Cured rubber is very soft, very strong and very "stretchy", stretching many times its original size without tearing and will rebound to its original form without distortion. Ecoflex™ rubbers are water white translucent and can be color pigmented with Silc Pig™ pigments for creating a variety of color effects. You can also add Smooth-On's Silicone Thinner™ to further lower the viscosity. THI-VEX™ silicone thickener can be added by weight to Ecoflex™ silicones for brushable applications.

Soft, Softer, Softest . . . Ecoflex™ rubbers are based on Smooth-On's Dragon Skin™ technology and are currently available in many different hardnesses: Shore A-5, Shore 00-10, 00-20, 00-30 and 00-50. They are suitable for a variety of applications including making prosthetic appliances, cushioning for orthotics and special effects applications (especially in animatronics where repetitive motion is required). Ecoflex™ 5 has a pot life of 1 minute and a demold time of 5 minutes – Available only in dispensing cartridges. Ecoflex™ 00-33 AF is an **anti-fungal** silicone suitable for making a variety of skin-safe cushioning device configurations that resist fungi for orthopedic and orthotic applications. Ecoflex™ 00-20 FAST has a 20 minute pot life and 1 hour cure time. Cured Ecoflex™ is skin safe and certified by an independent laboratory.

Note: Ecoflex™ 00-10 cures with a "tacky" surface.

TECHNICAL OVERVIEW

	Mixed Viscosity (ASTM D-2393)	Specific Gravity (g/cc) (ASTM D-1473)	Specific Volume (cu. in./lb.) (ASTM D-1475)	Pot Life (ASTM D-2471)	Cure Time	Shore Hardness (ASTM D-2240)	Tensile Strength (ASTM D-412)	100% Modulus (ASTM D-412)	Elongation at Break % (ASTM D-412)	Die B Tear Strength (ASTM D-624)	Shrinkage (in./in.) (ASTM D-2566)
Ecoflex™ 5	13,000 cps	1.07	25.8	1 min.	5 min.	5A	350 psi	15 psi	1000%	75 pli	< .001 in./in.
Ecoflex™ 00-50	8,000 cps	1.07	25.9	18 min.	3 hours	00-50	315 psi	12 psi	980%	50 pli	< .001 in./in.
Ecoflex™ 00-30	3,000 cps	1.07	26.0	45 min.	4 hours	00-30	200 psi	10 psi	900%	38 pli	< .001 in./in.
Ecoflex™ 00-33 AF	3,000 cps	1.07	26.0	45 min.	4 hours	00-33	200 psi	10 psi	900%	38 pli	< .001 in./in.
Ecoflex™ 00-20	3,000 cps	1.07	26.0	30 min.	4 hours	00-20	160 psi	8 psi	845%	30 pli	< .001 in./in.
Ecoflex™ 00-20 FAST	3,000 cps	1.07	26.0	20 min.	1 hour	00-20	160 psi	8 psi	845%	30 pli	< .001 in./in.
Ecoflex™ 00-10	14,000 cps	1.04	26.6	30 min.	4 hours	00-10	120 psi	8 psi	800%	22 pli	< .001 in./in.

*All values measured after 7 days at 73°F/23°C

Mix Ratio: 1A:1B by volume or weight
Color: Translucent

Useful Temperature Range: -65°F to 450°F (-53°C to 232°C)
Dielectric Strength (ASTM D-147-97a): >350 volts/mil

PROCESSING RECOMMENDATIONS

PREPARATION... Safety – Use in a properly ventilated area ("room size" ventilation). Wear safety glasses, long sleeves and rubber gloves to minimize contamination risk. Wear vinyl gloves only. Latex gloves will inhibit the cure of the rubber.

Store and use material at room temperature (73°F/23°C). Warmer temperatures will drastically reduce working time and cure time. Storing material at warmer temperatures will also reduce the usable shelf life of unused material. These products have a limited shelf life and should be used as soon as possible. Mixing containers should have straight sides and a flat bottom. Mixing sticks should be flat and stiff with defined edges for scraping the sides and bottom of your mixing container.

Cure Inhibition – Addition-cure silicone rubber may be inhibited by certain contaminants in or on the pattern to be molded resulting in tackiness at the pattern interface or a total lack of cure throughout the mold. Latex, tin-cure silicone, sulfur clays, certain wood surfaces, newly cast polyester, epoxy, tin cure silicone rubber or urethane rubber may cause inhibition. If compatibility between the rubber and the surface is a concern, a small-scale test is recommended. Apply a small amount of rubber onto a non-critical area of the pattern. Inhibition has occurred if the rubber is gummy or uncured after the recommended cure time has passed.

Because no two applications are quite the same, a small test application to determine suitability for your project is recommended if performance of this material is in question.

Safety First!

The Material Safety Data Sheet (MSDS) for this or any Smooth-On product should be read prior to use and is available upon request from Smooth-On. All Smooth-On products are safe to use if directions are read and followed carefully.

Keep Out of Reach of Children

Be careful. Use only with adequate ventilation. Contact with skin and eyes may cause irritation. Flush eyes with water for 15 minutes and seek immediate medical attention. Remove from skin with waterless hand cleaner followed by soap and water.

Important: The information contained in this bulletin is considered accurate. However, no warranty is expressed or implied regarding the accuracy of the data, the results to be obtained from the use thereof, or that any such use will not infringe upon a patent. User shall determine the suitability of the product for the intended application and assume all risk and liability whatsoever in connection therewith.

To prevent inhibition, one or more coatings of a clear acrylic lacquer applied to the model surface is usually effective. Allow any sealer to thoroughly dry before applying rubber. Note: Even with a sealer, platinum silicones will not work with modeling clays containing heavy amounts of sulfur. Do a small scale test for compatibility before using on your project.

Applying A Release Agent - Although not usually necessary, a release agent will make demolding easier when pouring into or over most surfaces. Ease Release™ 200 is a proven release agent for use with silicone rubber. Mann Ease Release™ products are available from Smooth-On or your Smooth-On distributor.

IMPORTANT: To ensure thorough coverage, lightly brush the release agent with a soft brush over all surfaces of the model. Follow with a light mist coating and let the release agent dry for 30 minutes.

If there is any question about the effectiveness of a sealer/release agent combination, a small-scale test should be made on an identical surface for trial.

MEASURING & MIXING...

Stir Part A and Part B thoroughly before dispensing. After dispensing required amounts of Parts A and B into mixing container (1A:1B by volume or weight), **mix thoroughly for 3 minutes making sure that you scrape the sides and bottom of the mixing container several times.** After mixing parts A and B, vacuum degassing is recommended to eliminate any entrapped air in liquid rubber. Your vacuum pump must pull a minimum of 29 inches of mercury (or 1 Bar / 100 KPa). Leave enough room in container for material expansion. Vacuum material until it rises, breaks and falls. Vacuum for 1 minute after material falls.

POURING, CURING & MOLD PERFORMANCE...

For best results, pour your mixture in a single spot at the lowest point of the containment field. Let the rubber seek its level up and over the model. **A uniform flow will help minimize entrapped air.** The liquid rubber should level off at least 1/2" (1.3 cm) over the highest point of the model surface.

Curing / Post Curing - Allow rubber to cure as prescribed at room temperature (73°F/23°C) before demolding. Do not cure rubber where temperature is less than 65°F/18°C. **Optional:** Post curing the mold will aid in quickly attaining maximum physical and performance properties. After curing at room temperature, expose the rubber to 176°F/80°C for 2 hours and 212°F/100°C for one hour. Allow mold to cool to room temperature before using.

If Using As A Mold - When first cast, silicone rubber molds exhibit natural release characteristics. Depending on what is being cast into the mold, mold lubricity may be depleted over time and parts will begin to stick. No release agent is necessary when casting wax or gypsum. Applying a release agent such as Ease Release™ 200 (available from Smooth-On) prior to casting polyurethane, polyester and epoxy resins is recommended to prevent mold degradation.

Thickening Ecoflex™ Silicones - THI-VEX™ is made especially for thickening Smooth-On's silicones for vertical surface application (making brush-on molds). Different viscosities can be attained by varying the amount of THI-VEX™. See the **THI-VEX™ technical bulletin** (available from Smooth-On or your Smooth-On distributor) for full details.

Thinning Ecoflex™ Silicones - Smooth-On's Silicone Thinner™ will lower the viscosity of Ecoflex™ silicones for easier pouring and vacuum degassing. A **disadvantage** is that ultimate tear and tensile are reduced in proportion to the amount of Silicone Thinner™ added. **It is not recommended to exceed 10% by weight of total system (A+B).** See the Silicone Thinner™ technical bulletin (available from Smooth-On or your Smooth-On distributor) for full details.

Mold Performance & Storage - The physical life of the mold depends on how you use it (materials cast, frequency, etc.). Casting abrasive materials such as concrete can quickly erode mold detail, while casting non-abrasive materials (wax) will not affect mold detail. Before storing, the mold should be cleaned with a soap solution and wiped fully dry. Two part (or more) molds should be assembled. Molds should be stored on a level surface in a cool, dry environment.



Call Us Anytime With Questions About Your Application.

Toll-free: (800) 381-1733 Fax: (610) 252-6200

The new www.smooth-on.com is loaded with information about mold making, casting and more.